

See discussions, stats, and author profiles for this publication at: <https://www.researchgate.net/publication/6763218>

Electronic Excitations in Metals and at Metal Surfaces

ARTICLE *in* CHEMICAL REVIEWS · NOVEMBER 2006

Impact Factor: 46.57 · DOI: 10.1021/cr050166o · Source: PubMed

CITATIONS

160

READS

34

7 AUTHORS, INCLUDING:



Andrey Borissov

Université Paris-Sud 11

200 PUBLICATIONS 4,511 CITATIONS

[SEE PROFILE](#)



Daniel Sánchez-Portal

Spanish National Research Council

166 PUBLICATIONS 11,843 CITATIONS

[SEE PROFILE](#)



V. M. Silkin

Universidad del País Vasco / Euskal Herriko U...

174 PUBLICATIONS 4,059 CITATIONS

[SEE PROFILE](#)



Vladlen Zhukov

Russian Academy of Sciences

112 PUBLICATIONS 1,401 CITATIONS

[SEE PROFILE](#)

Electronic Excitations in Metals and at Metal Surfaces

E. V. Chulkov,^{*,†,‡} A. G. Borisov,[§] J. P. Gauyacq,[§] D. Sánchez-Portal,[†] V. M. Silkin,[‡] V. P. Zhukov,[‡] and P. M. Echenique^{†,‡}

Departamento de Física de Materiales and Centro Mixto CSIC-UPV/EHU, Facultad de Ciencias Químicas, Universidad del País Vasco UPV/EHU, Apdo. 1072, 20080 San Sebastián/Donostia, Basque Country, Spain, Donostia International Physics Center (DIPC), Paseo de Manuel Lardizabal 4, 20018 San Sebastián/Donostia, Basque Country, Spain, and Laboratoire des Collisions Atomiques et Moléculaires (CNRS UMR 8625), Bâtiment 351, Université Paris-Sud, 91405 Orsay Cedex, France

Received January 21, 2006

Contents

1. Introduction	4160
2. Theory	4164
2.1. Inelastic Electron–Electron Scattering	4164
2.1.1. The GW Method	4164
2.1.2. The GW+T Method	4165
2.2. One-Electron Energy Conserving Processes	4166
2.2.1. The Wave Packet Propagation Method	4166
2.2.2. The Green Function Method	4170
2.3. Electron–Phonon Scattering	4171
2.4. Collective Excitations	4172
3. Electron Excitations in Bulk Para- and Ferro-magnetic Metals	4173
3.1. Simple Metals	4173
3.2. Noble Metals	4174
3.3. Paramagnetic Transition Metals	4175
3.4. Ferromagnetic Metals	4176
3.5. Comparison of Theoretical and Experimental Lifetimes	4178
4. Excitations on Clean Metal Surfaces	4178
4.1. Excitations in Surface States	4178
4.2. Excitations in Image-Potential States	4179
4.3. Collective Excitations on Clean Metal Surfaces	4182
5. Overlayers on Metal Surfaces	4183
5.1. Metal Overlayers on Metal Surfaces	4183
5.2. Insulating Overlayers on Metal Surfaces	4184
6. Adsorbates on Metal Surfaces	4188
6.1. Scattering of Delocalized States by Adsorbates	4188
6.2. Scattering by Defects Probed by Scanning Tunneling Microscopy	4191
6.3. Localization of 2D Continua by Defects at Surfaces	4192
6.4. Transient States Localized on Adsorbates at Surfaces	4193
6.5. Localized Excitons Formed by Inner-Shell Excitation in Surface Overlayers	4197
6.5.1. Charge Transfer Studies	4198
6.5.2. Effect of Ar Neighbors on the Ar*(2p _{3/2} –14s) State	4199

7. Summary and Outlook	4200
8. Acknowledgments	4201
9. References	4201

1. Introduction

Electron excitations in metal systems play an important role in many chemical and physical phenomena. They are of paramount importance for energy transfer in photochemical reactions,¹ in particular, in photodissociation and photodesorption processes.² They are essential for excitation mediated desorption and oxidation of molecules at surfaces³ as well as for electron localization at interfaces.⁴ It was recently shown that electronic excitations form a natural bridge between large-amplitude vibrations of molecules on metal surfaces and efficient electron emission.⁵ It was then argued that the conversion of these vibrations to electronic excitations is a clear indication of a strong nonadiabatic character of chemical reactions on metal surfaces. Electronic excitations have a profound impact on molecular motion induced by femtosecond laser pulses⁶ and play a large role in catalytic reactions as well as in spin transport within bulk metals, across interfaces, and at surfaces.^{7–9}

At metal surfaces, in addition to bulk electron states, new electron states arise. These new states can be classified as intrinsic surface states and image-potential states. Intrinsic surface states predicted by Tamm^{10,11} and later by Shockley¹² appear due to the cleavage of bulk metal. They are strongly coupled to the surface: the maximum of the probability density of these states is close to the surface atomic layer, and the density decays exponentially both into the bulk and into the vacuum. Since the first measurement of a surface state on Cu(111),¹³ surface states have been studied on many metal surfaces.^{14,15} Image-potential states are generated by a potential well formed by the Coulomb-like attractive image potential barrier and the repulsive crystal barrier.^{16–22} This potential well gives rise to a Rydberg-like series of image-potential states localized mainly in the vacuum side in front of the surface. The maximum of the probability density for the first image-potential state is several angstroms away from the surface and increases quadratically with the quantum number n . Therefore, image-potential states are coupled to a surface much weaker than the surface states.

One of the key quantities of the excited electron is its lifetime, which sets the duration of the excitation. Moreover, in combination with the velocity, this lifetime determines the mean free path, a measure of influence of the excitation.

* To whom correspondence should be addressed. E-mail: waptctce@sc.ehu.es. Telephone: +34 943 018220. Fax: +34 943 015600.

[†] Universidad del País Vasco.

[‡] Donostia International Physics Center.

[§] Université Paris-Sud.



Born in Skopin, Ryazan, Russia, and educated at Tomsk State University, Evgueni Chulkov received his Ph.D. in Physics from this university in 1980. His Ph.D. thesis was focused on electronic and thermodynamic properties of metals and alloys. He then worked at the Institute of Strength Physics and Materials Science of the SU Academy of Sciences as a senior researcher and since 1988 as a head of the laboratory of the Physics of Surface Phenomena, focusing on the study of electronic and vibrational properties of metal and semiconductor surfaces. In 1995 he moved to the University of the Basque Country, where he works as a Professor at the Materials Physics Department. His research interests are single-particle and collective excitations in metallic materials (including ferromagnetics) and in their surfaces as well as electron–electron, electron–phonon, and electron–magnon interactions.



Dr. Andrey G. Borisov received his B.A. in Physics from Moscow State University in 1989. He then received his Ph.D. in 1992 from Paris-Sud University. His research is focused on the dynamics of electron excitations at surfaces and electron transfer in particle–surface interactions. Coauthor of over 100 publications, he is currently a researcher in CNRS (Centre National de la Recherche Scientifique).

Lifetime is controlled by the interaction of the excited electron with other quasiparticles, e.g. with single-particle excitations—electrons and holes—or/and with collective excitations—phonons, magnons, and plasmons. These interactions change the energy and momentum of the excited electron (inelastic scattering of the electron on other quasiparticles) whereas a scattering of the electron on defects causes only a change of momentum (elastic scattering of the electron).

Electron (hole) excitation energies as well as the excited particle decay are closely related to the electron band structure of a metal, and via the interaction with phonon, magnon, and plasmon excitations, these quantities are also related to the phonon, magnon, and plasmon spectra of a metal. All these characteristics, electron, phonon, magnon, and plasmon spectra, as well as the decay rate (inverse lifetime), depend on the dimensionality of a system. For



Jean-Pierre Gauyacq was born in 1950 in Epernay (France). After studies at the Ecole Normale Supérieure in Paris, he prepared his thèse de doctorat at the Université Paris-Sud in Orsay (France), working with M. Barat on atomic collision studies. He was a post-doc with A. Herzenberg in the Engineering and Applied Science Department at Yale University (New Haven, CT, USA). He is currently Directeur de Recherche au CNRS (Centre National de la Recherche Scientifique) and works in Orsay in the Laboratoire des Collisions Atomiques et Moléculaires, which he directed in 1990–97. His research interests range from theoretical studies on atomic collisions, to electron–molecule collisions, to ion scattering at surfaces and the fast-time behavior of excited electrons at surfaces.



Dr. Daniel Sánchez-Portal was born in Madrid (Spain). He received his B.Sc. in 1993 from the Universidad Autonoma de Madrid and his Ph.D. from the same university in 1998. During his period in graduate school, working under the direction of Prof. Jose M. Soler and Prof. Emilio Artacho, he initiated his interest in the methodology of electronic structure calculations and its application to the study of complex materials and nanostructures. He participated in the development of the SIESTA method and code (see www.uam.es/siesta). This method is specially optimized to study large systems and allows performing self-consistent density-functional simulations with a linear scaling of the computational cost with the size of the system under study. The SIESTA code is currently used by many research groups in the academic community. After a postdoctoral stay (1999–2001) at the University of Illinois at Urbana-Champaign working with Prof. Richard M. Martin, he joined the Solid State Theory Group at the Universidad del Pais Vasco (UPV/EHU), where he started his collaboration with Prof. Pedro M. Echenique. He is currently a research scientist in the “Unidad de Física de Materiales”, Centro Mixto CSIC-UPV/EHU, located in San Sebastian, Spain. His research is devoted to the theoretical study and prediction of the structural and electronic properties of surfaces and nanostructures.

instance, on metal surfaces the decay of electrons excited in surface electron states will be modified by the interaction with surface phonons, magnons, and plasmons.^{23–31} Therefore, decay mechanisms on surfaces may be very different from those in the bulk.^{32–35} Bulk metals exhibit three-dimensional (3D) translational symmetry that leads to a discrete electron spectrum at any selected momentum in the



Vyacheslav M. Silkin was born in Ekibastuz, Soviet Union (now Kazakhstan), in 1959. He studied physics at Tomsk State University and moved to the Institute of Strength Physics and Materials Science of the Russian Academy of Sciences, Tomsk, where he obtained his Ph.D. degree in 1990 under the guidance of Prof. Evgueni Chulkov. In 1996 he joined the group of Prof. P. M. Echenique at the Materials Department of the University of Basque Country, San Sebastian, Spain. Since 2000 he has worked at the Donostia International Physics Center, San Sebastian, Spain. His research interests focus on the theoretical investigations of the surface electronic structures, collective electronic excitations in the bulk and at solid surfaces, and the dynamics of electronic excitations at metal surfaces.



Vladlen Zhukov was born in Sverdlovsk (now Ekaterinburg), Russia. He studied physical engineering in the same city, and afterward, he worked at the Institute of Solid State Chemistry of the Academy of Sciences. He received his master of sciences in physical chemistry in 1976 and the degree of doctor of sciences in solid-state physics in 1988. He became senior research associate in 1991 and chief research associate in 1993 at the same Institute. In 1994–1995 he spent one year in the group of theoretical chemistry at the University of Barcelona (Spain), and in 1998 he moved to the Institute of Material Research in Nantes (France). Since 1999 he has been working at the Donostia International Physics Center in San Sebastian (Spain). His current research interests include theoretical investigation of the electron dynamics in metals.

Brillouin zone. To illustrate this, we show the band structure of bulk Cu in Figure 1. With such an electronic structure, the decay of excited electrons in the absence of defects can occur only via inelastic scattering of the excited particle on other quasiparticles (other excited electrons, phonons, magnons, and plasmons). The formation of a metal surface leads to a loss of translational symmetry in the direction perpendicular to the surface. As a result, a metal surface exhibits two-dimensional (2D) translational symmetry and bulk states form a continuum of electron states with energy gaps in the projection of bulk band structure onto the 2D Brillouin zone. In Figure 2, we schematically show the projected bulk band structure as well as the energy positions of surface and



Pedro M. Echenique was born in 1950 in Isaba (Navarre). He studied Physics at the University of Navarra. He received his Ph.D. degree in 1976 from the University of Cambridge (U.K.) for a thesis on the interaction of energetic particles with surfaces, and in 1977 from the University of Barcelona (Spain) for his work on spatial excitation patterns induced by swift ions in condensed matter. After doing postdoctoral work at Oak Ridge National Laboratory (USA), Bohr Institute (Denmark), and Lund University (Sweden), he spent two years as a Visiting Professor at the University of Cambridge. In 1986 he joined the University of the Basque Country, where he is now Full Professor of Condensed Matter Physics. He also leads the newly established Donostia International Physics Center in San Sebastian (Spain). His current research interests include the interaction of swift particles and radiation with solids and nanostructured materials, and the electronic response of condensed matter.

image-potential states for Cu(111) (Ag(111)) and for Cu(100) (Ag(100) and Au(100)). The figure shows that, on metal surfaces, there exist not only gap surface and gap image-potential states, but there also exist resonance surface and image-potential states which lie outside energy gaps and, therefore, are degenerate in energy with bulk electron states. The change of the electron state character from the gap one to the resonance one results in a change of the dominating decay mechanism from many-body electron–electron (inelastic) scattering to a one-electron transition: the energy-conserving resonant electron transfer into the bulk metal states. The latter mechanism is more efficient than inelastic electron–electron scattering for electrons excited into resonance states. This one-electron decay mechanism does not exist in bulk metals. However, it is ubiquitous on clean metal surfaces, on surfaces with adatoms, and on surfaces covered with adlayers.

The decay rate of an excited electron or hole can be presented as a sum of four contributions:

$$\Gamma_{\text{tot}} = \Gamma_{\text{e-e}} + \Gamma_{\text{e-e}}^{\text{le}} + \Gamma_{\text{e-ph}} + \Gamma_{\text{e-def}} \quad (1)$$

The first term, $\Gamma_{\text{e-e}}$, describes the most important contribution from the inelastic electron–electron (e–e) scattering mechanism leading to decay of excited electrons (holes) to lower (higher) lying electron states with simultaneous creation of an electron–hole pair or/and plasmon excitation in paramagnetic metals and a Stoner pair or/and magnon excitation in ferromagnets. The second term, $\Gamma_{\text{e-e}}^{\text{le}}$, describes the contribution from the energy-conserving resonant electron-transfer mechanism. The third contribution, $\Gamma_{\text{e-ph}}$, represents the electron–phonon (e–ph) channel for energy relaxation of excited electrons (holes) via e–ph scattering. This mechanism is the only one which carries the temperature dependence of the electron (hole) decay in paramagnetic

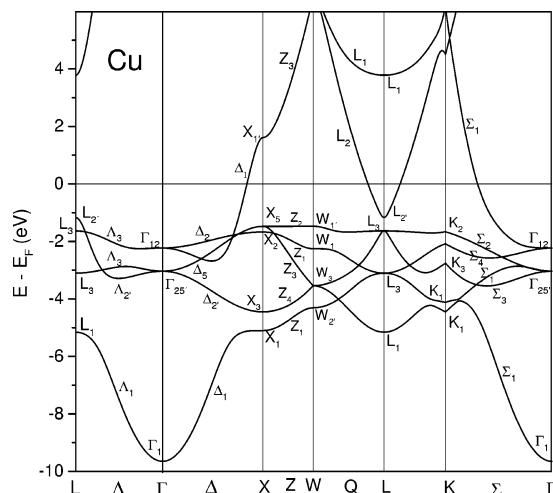


Figure 1. Calculated band structure of Cu along symmetry directions.

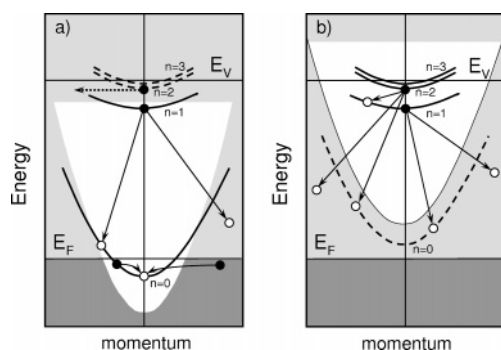


Figure 2. Schematic electronic structures of (a) Cu(111) and Ag(111) and (b) Cu(100), Ag(100), and Au(100). Energy is shown as a function of the momentum parallel to the surface. Solid lines represent surface and image-potential states that lie inside the energy gap while dashed lines depict resonance surface and image-potential states. Solid (open) circles show electrons (holes) in occupied bands as well as excited electrons (no electrons) in unoccupied states. Arrows indicate possible intra- (within the same band) and interband transitions which can occur at the decay process.

metals. The fourth term, $\Gamma_{e-\text{def}}$, describes elastic scattering which changes electron momentum and does not change its energy.

A study of the decay mechanisms of electron excitations on surfaces requires appropriate experimental and theoretical methods. Several experimental techniques are used to explore the decay of electron (hole) excitations in bulk metals and on metal surfaces. Photoelectron spectroscopy (PES) is applied to study the decay of holes (occupied electron states) through the spectral line shape and line width.^{36–38} The complementary technique, inverse photoemission (IP), permits measurements of the line width of unoccupied electron states.^{39–41} However, its limited energy resolution does not favor the extraction of precise quantitative information on line widths except for some favorable cases.⁴² The two-photon photoemission (2PPE) technique^{21,43} gives more precise information on spectral line shapes and line widths of unoccupied states. In some exceptional cases, it can also give information on occupied surface states.⁴⁴ Two-photon photoemission in the time-resolved mode (TR-2PPE) allows one to study the decay in the time domain.^{45–49} By combining this information with spectroscopic measurements, a very detailed picture of the electron dynamics emerges.^{50,51} Scanning tunneling microscopy (STM) combined with scan-

ning tunneling spectroscopy (STS)^{52–54} allows one to obtain detailed information on the decay properties of surface and image-potential states.^{32,55–58} The topographical images monitor simultaneously the quality and structures of the surface area under investigation.

A variety of theoretical methods is employed to study electron and hole dynamics in metals. The most powerful of them used for calculations of inelastic e–e scattering is a self-energy formalism of many-body theory.^{59–67} This formalism was introduced by Quinn and Ferrell (QF) for the description of the lifetime of excited electrons in a homogeneous electron gas.⁶⁸ The authors of ref 68 showed that for energies close to the Fermi level, E_F , the decay rate of excited electrons scales with energy as $\Gamma_{e-e} \sim (E - E_F)^2$. In the high-density limit, $r_s \rightarrow 0$, the inverse lifetime is

$$\hbar/\tau_{e-e}^{-1} = \Gamma_{e-e} = 2.5019r_s^{5/2}(E - E_F)^2 \text{ eV}^{-2} \text{ meV} \quad (2)$$

In eq 2 the Heisenberg uncertainty principle, $\Delta E \Delta t = \hbar$, is used to relate τ_{e-e}^{-1} and Γ_{e-e} ; τ_{e-e}^{-1} is in femtoseconds (fs), Γ_{e-e} in meV, and $\hbar = 1$ in atomic units. The electron density parameter r_s is determined by $4/3\pi r_s^3 n_0 = \Omega_0$, where n_0 is the number of valence electrons and Ω_0 is the volume per atom, respectively. In eq 2 r_s is assumed to be in atomic units while $E - E_F$ is in eV. For a long time, eq 2 was used for interpretation of measured line widths in terms of lifetimes for excited electrons and holes in surface states of real metals.^{69,70} The results of these interpretations were not satisfactory even for energies close to E_F . Later, at the end of the nineties and in 2000, it was shown that for the correct description of the hole (electron) lifetimes on surfaces it is necessary to include a realistic band structure of a metal into the calculations.^{32,71,72} So far, most calculations of the inelastic e–e scattering contribution Γ_{e-e} for paramagnetic materials have been performed within the Hedin GW approximation^{63,73} for the self-energy Σ and taking the material band structure into account.^{65,74–77} The GW approach represents the self-energy with the first term in the series expansion of Σ in terms of the screened Coulomb interaction W retained (with G being the Green function). The screened interaction W allows one to naturally include plasmon excitations into the electron (hole) decay picture. This mechanism becomes important when a plasmon lies in the energy interval accessible for electron decay.^{28,30,78} However, for ferromagnetic metals, GW is not sufficient to describe electron decay via excitation of spin waves (magnons) and Stoner pairs. These new mechanisms appear in the T-matrix generalization of GW, the GW+T-matrix approximation.^{79–82} For the description of an electron (hole) decay in resonance states on metal surfaces when one-electron processes are dominant, the wave propagation method and Green function methods are used.^{83–85} Electron–phonon interaction and the phonon-induced contribution to electron decay are calculated by employing the Eliashberg function.^{86–88}

Apart from the self-energy calculations of the electron- and phonon-induced contribution as well as the one-electron contribution to the excited electron decay rate, other studies of electron dynamics have been undertaken. In particular, Gumhalter has estimated the lifetime of the excited electron in the first image state as well as the lifetime of the excited hole in the surface state on the Cu(111) surface by using the cumulant expansion for a single particle propagator.^{89–91} Sakaue *et al.*^{92–94} discussed energy relaxation and dephasing times obtained from 2PPE measurements and the relation

of these times with intrinsic lifetimes of electrons and holes on Cu(111) by employing the nonequilibrium Green function method. In general, the results obtained from the use of the cumulant expansion and from nonequilibrium Green function methods are in agreement with the GW calculation results for electron and hole dynamics. Nagy *et al.*^{95–99} have recently studied the role of spin and charge in the screening of electron–electron interaction in the free electron gas model, going beyond the random phase approximation (RPA). For that they used the Landau kinetic model of relaxation rate at energies close to the Fermi level. Charge and spin response functions were constructed in terms of local field factors, thus leading to the spin dependent lifetimes. It was shown that the scattering rate of the spin-fluctuation channel gives around 25% of the total decay rate of an excited electron. A different approach based on the Boltzmann equation was proposed by Knorren *et al.*^{100,101} This approach allows one to study the energy dependence of electron lifetimes (the momentum dependence has not been included in the theory) and secondary electron effects. An overview of the results obtained with this method is given in ref 102.

The review is organized as follows. We give a short description of the calculation methods used in section II. In particular, the GW and GW+T formulations for the electron self-energy are briefly described. Both these methods designed for calculations of inelastic (many-body) e–e scattering are well presented in the literature, and for more details we refer the reader to the corresponding publications. These methods are followed by the description of the wave packet propagation method. The latter method, designed for evaluations of one-electron energy conserving processes, has been outlined only briefly in a few publications. Therefore, we present it here in detail. Then we describe another method developed to study one-electron processes, namely, the Green function method. We also give a brief description of an *ab initio* method for calculation of the e–ph interaction in metals. Finally, we outline the method for calculations of the surface response function. The latter allows one to evaluate surface and acoustic surface plasmon characteristics: the energy position and width. These are naturally related to the study of excited electrons since the response function is one of the key ingredients of the imaginary part of the electron self-energy and thus it can influence the lifetime of excited electrons in image potential states.²⁸ In section III we review the calculation and experimental study of lifetimes in bulk simple, noble, and transition paramagnetic metals. Electron dynamics in ferromagnets are also discussed. The results on lifetimes of excited electrons in image-potential states and excited electrons and holes in surface states are reviewed in section IV. A part of these results has been discussed in ref 74. Here we review these data in parallel with new experimental and theoretical findings. The discussion of the line width of surface plasmons as well as acoustic surface plasmons is also presented in this section. Section V is devoted to electron excitations in metal and insulating overlayers on metal substrates. Theoretical and experimental lifetimes are reviewed for electron and hole excitations in quantum-well states in metal overlayers, while electron excited lifetimes in image states are discussed for rare gas layers on noble metals. In section VI, we discuss the dynamics of electrons excited into delocalized 2D states and scattered by adsorbates. Lifetimes of electrons in transient states localized on adsorbates at surfaces are also reviewed. This is followed by analysis of localized excitons

in Ar adlayers on a metal surface and charge transfer in such systems. Finally, the conclusions are drawn in section VII. Unless otherwise stated, atomic units are used throughout, i.e., $e^2 = m_e = \hbar = 1$, where e and m_e are the electron charge and mass, respectively, and $\hbar = h/2\pi$, with h being Planck's constant. The atomic unit of length is the Bohr radius, $a_0 = 0.529$ Å. The 3D and 2D vectors are defined by $\mathbf{r} = \{x, y, z\}$ and $\mathbf{r}_{||} = \{x, y\}$, respectively.

2. Theory

2.1. Inelastic Electron–Electron Scattering

Below we give a brief description of the many-body methods, GW and GW+T, widely used to calculate the inelastic e–e scattering contribution to the electron (hole) decay rate. This decay rate is related to the energy relaxation of excited electrons via creation of e–h pairs and plasmon excitation in paramagnetic metals, as well as via creation of Stoner pairs and spin wave generation in ferromagnets. Within the many-body theory, the inelastic e–e scattering contribution to the decay rate, Γ , i.e., the inverse lifetime, of an electron with momentum \mathbf{k} , band index i , spin σ , and energy $\epsilon_{\mathbf{k},i,\sigma} > E_F$ is obtained in the “on energy-shell” approximation as the projection of the imaginary part of the self-energy operator onto the electron state $\psi_{\mathbf{k},i,\sigma}(\mathbf{r})$ (see, for instance, refs 63 and 65)

$$\Gamma_{e-e}(\epsilon_{\mathbf{k},i,\sigma}) = -2 \int d\mathbf{r} \int d\mathbf{r}' \psi_{\mathbf{k},i,\sigma}^*(\mathbf{r}) \text{Im} \Sigma_o(\mathbf{r}, \mathbf{r}', \epsilon_{\mathbf{k},i,\sigma}) \psi_{\mathbf{k},i,\sigma}(\mathbf{r}') \quad (3)$$

where $\psi_{\mathbf{k},i,\sigma}(\mathbf{r})$ and $\epsilon_{\mathbf{k},i,\sigma}$ are the eigenfunctions and eigenvalues of the one-electron Hamiltonian. In the GW approximation for the self-energy, only the first term in the series expansion in terms of the screened Coulomb interaction is retained.^{63,64} The GW+T method represents a generalization of the GW approximation by including the higher-order self-energy terms that allow for the calculation of the quasiparticle decay in ferromagnetic systems on the same footing as in paramagnetics.

Self-energy can be represented as^{79,81,82,103}

$$\Sigma_o(\mathbf{r}, \mathbf{r}', \epsilon_{\mathbf{k},i,\sigma}) = \Sigma_o^{\text{GW}}(\mathbf{r}, \mathbf{r}', \epsilon_{\mathbf{k},i,\sigma}) + \Sigma_o^{\text{T}}(\mathbf{r}, \mathbf{r}', \epsilon_{\mathbf{k},i,\sigma}) \quad (4)$$

where Σ_o^{GW} is the self-energy derived within the GW approximation⁶³ and Σ_o^{T} is the self-energy contribution obtained from the T-matrix approximation which accounts for electron–hole, electron–electron, and hole–hole interactions multiple scattering. One should note that in this formulation of self-energy a few double counting terms which are already contained in the GW approximation should be subtracted from the T-matrix.^{79,81,82,103,104}

2.1.1. The GW Method

In this subsection we consider paramagnetic systems only and thus omit the spin index. In the GW approximation, the imaginary part of the self-energy is evaluated in terms of the screened interaction $W(\mathbf{r}, \mathbf{r}', \omega_{if})$ and the allowed final states $\psi_{\mathbf{k}',f}(\mathbf{r})$ for the decay process:

$$\text{Im} \Sigma(\mathbf{r}, \mathbf{r}', \epsilon_{\mathbf{k},i}) = \sum_{\epsilon_{\mathbf{k}',f} \geq \epsilon_{\mathbf{k},i} \geq E_F} \psi_{\mathbf{k}',f}^*(\mathbf{r}') \text{Im} W(\mathbf{r}, \mathbf{r}', \omega_{if}) \psi_{\mathbf{k}',f}(\mathbf{r}) \quad (5)$$

Here, $\omega_{if} = \epsilon_{\mathbf{k}',i} - \epsilon_{\mathbf{k}',f}$ and the summation is performed over the final-state energies, which are between the initial state and the Fermi energy, E_F . For the holes, these energies are below the Fermi energy. Finally, the inverse lifetime within GW is calculated as

$$\tau_{e-e}^{-1}(\epsilon_{\mathbf{k},i}) = -2 \sum_{\epsilon_{\mathbf{k}',f}} \int d\mathbf{r} \int d\mathbf{r}' \psi_{\mathbf{k}',i}^*(\mathbf{r}) \psi_{\mathbf{k}',f}^*(\mathbf{r}') \times \text{Im } W(\mathbf{r}, \mathbf{r}', \omega_{if}) \psi_{\mathbf{k}',i}(\mathbf{r}') \psi_{\mathbf{k},f}(\mathbf{r}) \quad (6)$$

The screened interaction W is given in linear response theory by

$$W(\mathbf{r}, \mathbf{r}', \omega) = v(\mathbf{r} - \mathbf{r}') + \int d\mathbf{r}_1 \int d\mathbf{r}_2 [v(\mathbf{r} - \mathbf{r}_1) + K^{xc}(\mathbf{r}, \mathbf{r}_1, \omega)] \chi(\mathbf{r}_1, \mathbf{r}_2, \omega) v(\mathbf{r}_2 - \mathbf{r}') \quad (7)$$

where $v(\mathbf{r} - \mathbf{r}')$ is the bare Coulomb interaction and $\chi(\mathbf{r}, \mathbf{r}', \omega)$ is the linear density–density response function. In short notation, this equation can be rewritten as

$$W = v + (v + K^{xc})\chi v \quad (8)$$

The density–density response function χ is obtained from the following integral equation

$$\chi = \chi^0 + \chi^0(v + K^{xc})\chi \quad (9)$$

where χ^0 is the density–density response function of the noninteracting electron system:

$$\chi^0(\mathbf{r}, \mathbf{r}', \omega) = 2 \sum_{ij} \frac{\theta(E_F - \epsilon_i) - \theta(E_F - \epsilon_j)}{\epsilon_i - \epsilon_j + (\omega + i\eta)} \psi_i(\mathbf{r}) \psi_j^*(\mathbf{r}) \psi_j(\mathbf{r}') \psi_i^*(\mathbf{r}') \quad (10)$$

In this equation, η is an infinitesimally small positive constant. The kernel K^{xc} entering eqs 7–9 accounts for the reduction of the electron–electron interaction due to the existence of short-range exchange and correlation effects associated with the probe electron (eq 8) and with screening electrons (eq 9). Most calculations of the lifetimes of electrons and holes in surface and image-potential states that have been performed to date use the RPA. In this approximation, the exchange and correlation kernel K^{xc} is omitted from eqs 7–9.

Inclusion of exchange and correlation effects in the screened interaction (eq 8) and in the screening (eq 9) act in opposite directions as the evaluation of the lifetimes is concerned. This is easy to understand by considering the physics involved. Inclusion of exchange and correlation effects in the screening results in a reduced screening effect and, therefore, reduces the lifetime of a hot electron while inclusion of exchange and correlation in the screened interaction of the quiparticle with the medium reduces the interaction and, therefore, increases the lifetime. When the exchange and correlation kernel is included in W (eq 8), we shall refer to it as WT .¹⁰⁵

2.1.2. The GW+T Method

In the GW+T extension of the GW method, the central quantity is the T-matrix operator, which is defined as a

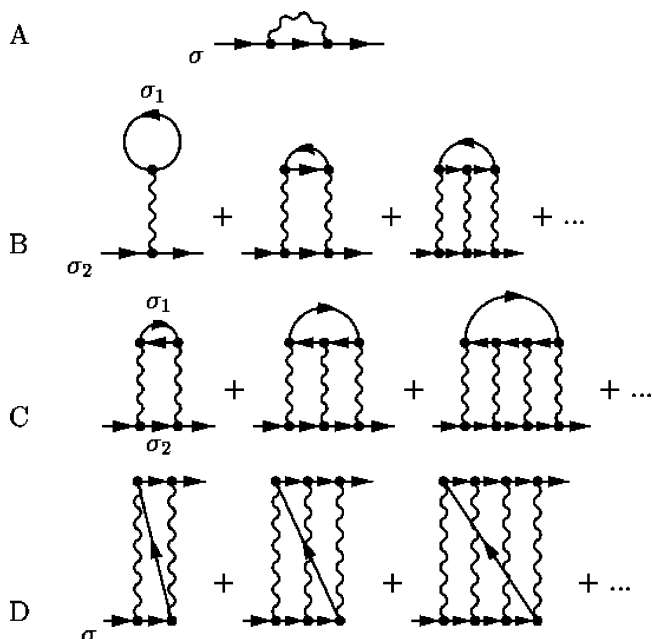


Figure 3. Feynman diagrams for the GW and T-matrix self-energy of an excited electron: (A) GW-term; (B) T-matrix direct terms with multiple electron–electron scattering; (C) T-matrix direct terms with electron–hole scattering; (D) T-matrix exchange terms. The vertical wiggly lines represent static screened potential, and the lines with arrows are Green functions. The time direction is to the right. By changing the time direction, one obtains analogous diagrams for the self-energy of an excited hole.

solution of the Bethe–Salpeter (BS) equation⁶²

$$T_{\sigma_1, \sigma_2}(1, 2|3, 4) = W(1, 2) \delta(1 - 3) \delta(2 - 4) + W(1, 2) \int d1' d2' K_{\sigma_1, \sigma_2}(1, 2|1', 2') T_{\sigma_1, \sigma_2}(1', 2'|3, 4) \quad (11)$$

Here we use the short-hand notation $1 \equiv (\mathbf{r}_1, t_1)$. W is a screened potential, and the kernel K_{σ_1, σ_2} is a two-particle propagator. In the case of multiple electron–hole scattering, the kernel (electron–hole propagator) is a product of electron and hole time-ordered Green’s functions

$$K_{\sigma_1, \sigma_2}^{e-h}(1, 2|1', 2') = iG_{\sigma_1}(1, 1') G_{\sigma_2}(2', 2) \quad (12)$$

For electron–electron scattering, it is a product of two electron Green functions

$$K_{\sigma_1, \sigma_2}^{e-e}(1, 2|1', 2') = iG_{\sigma_1}(1', 1) G_{\sigma_2}(2', 2) \quad (13)$$

and for hole–hole scattering, it is a product of two hole Green functions

$$K_{\sigma_1, \sigma_2}^{h-h}(1, 2|1', 2') = iG_{\sigma_1}(1, 1') G_{\sigma_2}(2, 2') \quad (14)$$

Diagrams used for the GW and T-matrix self-energy are shown in Figure 3. With these diagrams and the kernel of eq 12, the self-energy term describing multiple electron–hole scattering can be expressed as

$$\Sigma_{\sigma_2}^{e-h}(4, 2) = -i \sum_{\sigma_1} \int d1 d3 G_{\sigma_1}(3, 1) T_{\sigma_2, \sigma_1}(1, 2|3, 4) \quad (15)$$

Similar equations can be obtained for multiple e–e and h–h scattering.⁸² In general, the screened potential W is energy dependent. However, to make computations feasible, the

local and static approximation, $W(1,2) = W(\mathbf{r}_1, \mathbf{r}_2) \delta(\mathbf{r}_1 - \mathbf{r}_2) \delta(t_1 - t_2)$, is frequently used.^{79,81,82,106} More discussion on the effect of the local approximation on the self-energy can be found in refs 103 and 104. Most calculations for excited electron lifetimes have been done within this approximation. For details, we refer the reader to refs 79, 81, 82, and 106.

2.2. One-Electron Energy Conserving Processes

2.2.1. The Wave Packet Propagation Method

The wave packet propagation (WPP) approach that we are addressing here is a powerful and versatile technique to study the one-particle evolution driven by an effective Hamiltonian H . The advantage of this method is that it can be equally applied to stationary problems (such as the search for resonances or scattering matrix calculations) and to explicitly dynamic problems (e.g. projectile–surface collisional charge transfer). The changes to be made at the computational level are minimal. In surface science, the wave packet propagation technique has been widely used to describe the heavy particle dynamics involved in chemical reactions at surfaces, such as molecule–surface interactions, photoinduced processes, etc.^{107–118} Explicit treatments of the electron dynamics at surfaces also appeared,^{119,120} where most of the recent developments addressing electronically excited states are directly linked with TR-2PPE experiments in the femtosecond time domain (see refs 121–123 and further references in this review).

The core of the WPP method consists of the direct solution of the time-dependent Schrödinger equation for the wave function $\Psi(\mathbf{r}, t)$ of the “active” electron:

$$i \frac{\partial \Psi(\mathbf{r}, t)}{\partial t} = H(t) \Psi(\mathbf{r}, t) \quad (16)$$

subject to the initial conditions, $\Psi_0 \equiv \Psi(\mathbf{r}, t=0)$. The solution of eq 16 is given by

$$\Psi(\mathbf{r}, t) = U(t) \Psi_0 \quad (17)$$

with propagator $U(t)$:

$$U(t) = \mathcal{T} \exp(-i \int_0^t H(t') dt') \quad (18)$$

where \mathcal{T} is the time-ordering operator. In the case of a time-independent Hamiltonian as considered below, eq 18 transforms to

$$U(t) = \exp(-iHt) \quad (19)$$

Once the $\Psi(\mathbf{r}, t)$ solution is obtained, it is analyzed to get the physical quantities of interest. With the propagator given by eq 19, the time-to-energy Laplace transform is usually applied, allowing a direct link with the retarded Green function. Indeed, using eqs 17 and 19,

$$\hat{L}(\omega) \Psi(\mathbf{r}, t) \equiv \int_0^\infty e^{i(\omega + i\eta)t} \Psi(\mathbf{r}, t) dt = i \left(\frac{1}{\omega + i\eta - H} \right) \Psi_0 \quad (20)$$

where $\eta \rightarrow +0$ and the term in the curved brackets is the retarded Green function $G^+(\omega)$. Obviously,

$$n(\omega) = \text{Re}\{\langle \Psi_0 | \hat{L}(\omega) \Psi(\mathbf{r}, t) \rangle\} \quad (21)$$

is the density of states projected onto the initial state. In practice, $n(\omega)$ is calculated from the Laplace transform of the survival amplitude:

$$A(t) = \langle \Psi_0 | \Psi(\mathbf{r}, t) \rangle \quad (22)$$

The Lorentzian fit of the structures in $n(\omega)$ can be used to calculate the energies, E , and the widths, Γ , of the quasi-stationary states.⁸³ However, if long-lived states are present in the system, long propagation times might be needed in order to reach convergence of the projected density of states (DOS). This problem can be avoided via a direct fit of the $A(t)$ signal to a sum of exponentially decaying terms:

$$A(t) = \sum_{j=1}^J a_j e^{-i(E_j - i(\Gamma_j/2))t} \quad (23)$$

Some parameters are stable with respect to J ; they are associated with the energies E_j and widths Γ_j of the resonances. The procedure defined by eq 23 works well if the number of resonances contributing to $A(t)$ is small. For the cases where the number of resonances is large, the “filter diagonalization” technique^{124,125} should be preferred. Equation 23 can be used equally well to search for the stationary (bound) states of the system. The corresponding Γ_j is zero in this case. It is noteworthy that the only requirement on the initial state wave function is that Ψ_0 is chosen in such a way that it has the largest possible overlap with states under study. This statement is particularly transparent in the case of a Hamiltonian with a discrete energy spectrum: $H\psi_j = E_j\psi_j$, where eq 17 leads to

$$\Psi(\mathbf{r}, t) = \sum_j e^{-iE_j t} \langle \psi_j | \Psi_0 \rangle \psi_j \quad (24)$$

and the survival amplitude is given by

$$A(t) = \sum_j e^{-iE_j t} |\langle \psi_j | \Psi_0 \rangle|^2 \quad (25)$$

Obviously, only the states with $|\langle \psi_j | \Psi_0 \rangle|^2 \neq 0$ can be revealed by the spectral analysis of $A(t)$.

For the case of bound states or narrow and well-defined resonances, eq 20 with ω set equal to the bound state (resonance) energy provides the corresponding wave function.

With eqs 20 and 21 one can also calculate the tunneling conductance, \mathcal{J} , of the STM experiments.¹²⁶ Indeed, according to the Tersoff–Hamann theory,¹²⁷ \mathcal{J} is proportional to the local density of states at the tip position, \mathbf{r}_{tip} . Then it is sufficient to set $\Psi_0 = \delta(\mathbf{r} - \mathbf{r}_{\text{tip}})$ and use eq 21 to calculate \mathcal{J} . In practice, the δ -function is replaced by a narrow Gaussian function centered at \mathbf{r}_{tip} .

Further applications of the WPP method are discussed below. We now turn to the numerical aspects. In choosing a specific algorithm from the variety of numerical approaches to the solution of eq 16, several main issues have to be addressed: (1) the wave function representation and calculation of the Hamiltonian action on the wave function, $H\Psi$;^{128–132} (2) the wave function propagation in time;^{133,135–137} (3) problems related with the finite size of the mesh and corresponding reflections of the wave packet at the boundaries.^{131,138–140} These aspects are not necessarily independent, as the wave function representation often imposes some constraints on the time propagator. In what follows,

we give specific examples linked with works by the authors.^{84,126,141–155} It should be understood that the choices of the algorithms made here are by far not unique, and the reader can find that his/her own experience is different from ours.

In most of the WPP studies of the dynamics of excited states at surfaces, we are interested in the effect of localized perturbers such as defects and adsorbates. The structure of the model potentials that are used is then such that a convenient coordinate system is the cylindrical one $\mathbf{r} = (\rho, \varphi, z)$ with the z -axis perpendicular to the surface and going through the defect center. The Hamiltonian is given by

$$H = \underbrace{-\frac{1}{2} \frac{\partial^2}{\partial z^2}}_{T_z} + \underbrace{-\frac{1}{2\rho} \frac{\partial}{\partial \rho} \rho \frac{\partial}{\partial \rho}}_{T_{\rho\varphi}} - \frac{1}{2\rho^2} \frac{\partial^2}{\partial \varphi^2} + V(\rho, \varphi, z) \quad (26)$$

Typically, the (model) potential of the system $V(\rho, \varphi, z)$ consists of several terms, as explained below:

$$V(\rho, \varphi, z) = V_s(z) + V_{\text{Ads}}(\rho, \varphi, z) + V_{\text{opt}} \quad (27)$$

For the metallic substrates considered in this review, two models are used for the electron–surface interaction potential, $V_s(z)$. Both models consider only the z -dependence of the interaction; that is, free-electron motion parallel to the surface is assumed. The first model, taken from ref 156, represents a free electron–metal substrate where a constant potential inside the metal smoothly joins the image potential $-1/4z$ on the vacuum side. The second model is used to study the effects of the projected band structure of certain surfaces, such as, e.g., the (111) and (100) surfaces of noble metals. $V_s(z)$ is then given by the model potential from ref 157. This potential has been constructed on the basis of *ab initio* studies in such a way that it reproduces the properties of the surface electronic band structure at the $\bar{\Gamma}$ point: the energy position of the projected band gap, surface state, and image potential states.

$V_{\text{Ads}}(\rho, \varphi, z)$ stands for the change of the electron–surface interaction due to the presence of an adsorbate, a defect, an adsorbate layer, etc. It is represented with model potentials, or potentials obtained from the density functional calculations.

We are interested in the electron dynamics in the *a priori* infinite space while performing the calculations on finite size grids. To suppress the reflection of the wave packet, an optical absorbing potential V_{opt} is introduced at the grid boundaries.^{131,138–140} Consistent with the causality principle, an optical absorbing potential imposes the outgoing wave boundary conditions and plays the role of the $i\eta$ term in $G^+(\omega)$ given by eq 20. Most often, we use an optical potential of the form

$$V_{\text{opt}} = -iC_1(z - C_2)^2, z \leq C_2$$

$$V_{\text{opt}} = 0, z > C_2 \quad (28)$$

where C_1 and C_2 are some positive constants adjusted to reach the desired absorption of the incident waves within the energy range of interest. Equation 28 corresponds to an optical potential introduced at the small z edge of the mesh. Similar potentials may be introduced at the other z and ρ edges of the mesh.

Being a one-electron treatment, the WPP technique does not explicitly account for the inelastic energy relaxation of the excited states due to many-body effects such as electron–electron scattering. The role of the inelastic electron–electron interactions can be estimated by the procedure used in low energy electron diffraction calculations.¹³⁴ It consists of adding a small negative imaginary part to V_s everywhere inside the metal.

With a wave function representation on a finite size mesh in cylindrical coordinates, the time dependent solution $\Psi(t)$ of eq 16 with the Hamiltonian in eq 26 is obtained numerically via short time-propagation:

$$\Psi(t+\Delta t) = U(\Delta t) \Psi(t) \quad (29)$$

where $U(\Delta t)$ is given by eq 19. The action of the $e^{-i\Delta t H}$ operator on the wave function in eq 29 is calculated via the split-operator technique.^{135,137}

$$e^{-i\Delta t H} = e^{-i(\Delta t/2)V} e^{-i\Delta t T_z} e^{-i\Delta t T_{\rho\varphi}} e^{-i(\Delta t/2)V} + O(\Delta t^3) \quad (30)$$

For an equidistant mesh of $N_\rho \times N_\varphi \times N_z$ points in ρ , φ , and z coordinates, respectively, the actual algorithm of the time-propagation, based on eq 30, involves several steps.

(I) The $e^{-i(\Delta t/2)V}$ operator is, in general, local in the direct (coordinate) space. Therefore, the calculation of the $e^{-i(\Delta t/2)V}\Psi(t)$ reduces to the corresponding multiplications at the grid points. However, in some cases, such as, e.g., the study of the alkali adsorbate-induced resonances, the potential V contains nonlocal terms arising from the pseudo-potential representation of the electron interaction with the alkali atom core. The nonlocal part of the potential has the form of a projector operator: $V_{\text{NL}} = |\alpha\rangle\langle\alpha|$. Then, further splitting of the operators in eq 30 is performed in order to single out the $e^{-i(\Delta t/2)V_{\text{NL}}}$ operator. Its action on the wave function is calculated in direct space, according to

$$e^{-i(\Delta t/2)V_{\text{NL}}} = 1 + \frac{(e^{-i\Delta t\langle\alpha|\alpha\rangle/2} - 1)}{\langle\alpha|\alpha\rangle} |\alpha\rangle\langle\alpha| \quad (31)$$

as can be straightforwardly obtained from the Taylor series representation of the exponential.

(II) The $e^{-i\Delta t T_{\rho\varphi}}$ operator is diagonal in the $[1/(2\pi)]^{1/2} e^{im\varphi}$ angular basis, where m stands for the magnetic quantum number. The pseudospectral approach^{131,133} is then used, where the wave function $\Phi \equiv e^{-i(\Delta t/2)V}\Psi$ is transformed into the $e^{im\varphi}$ representation with a direct fast Fourier transform, so that $e^{-i\Delta t T_{\rho\varphi}}\Phi$ is given by

$$e^{-i\Delta t T_{\rho\varphi}}\Phi(\rho, \varphi, z, t) = \sum_{m=-N_\varphi/2}^{N_\varphi/2-1} e^{im\varphi} e^{i\Delta t[(1/2\rho)(\partial/\partial\rho)\rho(\partial/\partial\rho) - (m^2/2\rho^2)]} \Phi_m(\rho, z, t) \quad (32)$$

where the action of the exponential operator on the right hand side (rhs) of eq 32 is calculated with the stable Cayley transform:^{158,159}

$$\tilde{\Phi}_m(\rho, z) \equiv e^{-i\Delta t T} \Phi_m(\rho, z) = \frac{1 - i\Delta t T/2}{1 + i\Delta t T/2} \Phi_m(\rho, z) + O(\Delta t^3) \quad (33)$$

Under transformation of eq 33 to the form

$$\left(1 + i\frac{\Delta t}{2}T\right)\tilde{\Phi}_m(\rho, z) = \left(1 - i\frac{\Delta t}{2}T\right)\Phi_m(\rho, z) \quad (34)$$

and with use of the three point finite differences for the ρ derivatives entering the kinetic energy operator, one obtains the three-diagonal set of equations for the unknown values of $\tilde{\Phi}_m(\rho, z)$ at the points of the ρ -mesh (see details in refs 83 and 160). Finally, an inverse fast Fourier transform is used to perform the summation in eq 32 in order to obtain the wave function in the direct space.

(III) The $e^{-i\Delta t T_z}$ operator is diagonal in the $[1/(2\pi)^{1/2}]e^{ikz}$ plane wave basis, where it takes the form $e^{-i\Delta t k^2/2}$. Then, similarly to step II, the pseudospectral approach^{131,133} with fast Fourier transforms is used to calculate the action of the $e^{-i\Delta t T_z}$ exponential on the wave function.

The above procedure is unitary; that is, if no optical potential is included, the norm of the wave function is preserved in due course of the time propagation. The loss of norm due to the action of the optical potential mimics the spread of the wave packet outside the calculation box boundaries.

The algorithm is greatly simplified if the total potential of the system V has cylindrical symmetry. With the wave function represented as

$$\Psi(\rho, \varphi, z, t) = \sum_m \frac{1}{\sqrt{2\pi}} e^{im\varphi} \Psi_m(\rho, z, t) \quad (35)$$

the 3D problem can be reduced to a number of 2D problems. Indeed, the $\Psi_m(\rho, z, t)$ components evolve independently and one has to propagate 2D wave packets with initial conditions defined in each m -subspace of interest.

The numerical convergence of the WPP calculations can be essentially improved with a variable change $\rho = f(\xi)$, where, for the equidistant “calculation” mesh in the ξ -coordinate, the “physical” mesh in the ρ -coordinate is dense close to the origin. The variable change is accompanied by the following change of the wave function:

$$\Psi(\xi, \varphi, z, t) = \frac{\psi(\xi, \varphi, z, t)}{\sqrt{f(\xi)f'(\xi)}} \quad (36)$$

where $f'(\xi) = \partial f / \partial \xi$. The wave function $\psi(\xi, \varphi, z, t)$ obeys the time dependent Schrödinger equation (eq 16), where, as compared to eq 26, the $T_{\rho\varphi}$ part takes the form

$$T_{\rho\varphi} \rightarrow T_{\xi\varphi} = -\frac{1}{2} \frac{1}{\sqrt{ff'}} \frac{d}{d\xi} f' \frac{d}{d\xi} \frac{1}{\sqrt{ff'}} - \frac{1}{2f^2} \frac{\partial^2}{\partial \varphi^2} \quad (37)$$

Time propagation is then performed with the algorithm described above.

At this point, a comment is in order with respect to the choice of the split-operator technique and the Cayley transform for time propagation. Indeed, the second-order-difference (SOD) method,¹³⁷ also called leapfrog, has an accuracy of the same order in Δt . Moreover, in modern quantum chemistry, the short-time Lanczos^{136,137,161} and global Chebyshev^{137,162} time-propagation techniques are considered the state-of-the-art approaches, since they offer much higher accuracy. The Chebyshev approach, allowing the entire propagation in a single time step and providing exponential convergence, is, in fact, often used as a benchmark to test other methods.¹³⁷

The advanced Lanczos and Chebyshev methods rely on the fact that the Hamiltonian is a Hermitian operator. This is not the case here because of the use of an optical absorbing potential (eq 28). For the Lanczos scheme, this problem can

be solved by separating the exponential from the optical potential via the split approximation:

$$e^{-i\Delta t H} \rightarrow e^{-i\Delta t V_{\text{opt}}/2} e^{-i\Delta t \tilde{H}} e^{-i\Delta t V_{\text{opt}}/2} \quad (38)$$

where $\tilde{H} = H - V_{\text{opt}}$. The highly accurate Lanczos method is then used to calculate the action of $e^{-i\Delta t \tilde{H}}$ on the wave function. Indeed, the sole role of an optical potential is to avoid the reflection of the wave packet at the boundaries of the grid. Its precise calculation is of no importance as long as reflection does not occur. Another possibility is to use the Lanczos–Arnoldi propagation scheme,^{163,164} which is an extension of the Lanczos method to non-Hermitian Hamiltonians. As for the Chebyshev method, one can use the energy-domain scheme described by Mandelshtam and Taylor¹⁶⁵ to extract, e.g., the scattering matrix of the system. If the time-domain dynamics is of interest, one has to change from the Chebyshev-polynomial based method to the Faber-polynomial representation of the propagator $U(t)$ in eq 19.^{166–169}

However, the main problem arises because of the spectral range of the Hamiltonian projected on the grid (grid-Hamiltonian). One of the specificities of the present work is that it considers the evolution of an electronic wave packet. In contrast to heavy particle (e.g. molecular) wave functions, electronic wave functions often present sharp features, such as the Coulomb cusp. The description of these requires quite dense meshes, so that the grid-Hamiltonians possess very large eigenvalues, primarily because of the kinetic energy part. The SOD method is conditionally stable; that is, the time step should satisfy $\Delta t < 1/|E|_{\text{max}}$, where $|E|_{\text{max}}$ stands for the maximum of the absolute value of the grid-Hamiltonian eigenvalues. This means that in the present case the propagation time step has to be extremely small for the SOD to be stable. Thus, for a given propagation time, too many time steps are needed. The situation is more delicate with Lanczos and Chebyshev techniques. *A priori*, these are unconditionally stable, so that a large $|E|_{\text{max}}$ does not seem to be a difficulty. Nonetheless, it is. Indeed, the number of terms in the Chebyshev-polynomial representation of the propagator $U(t)$ grows as $|E|_{\text{max}}$ for a fixed total propagation time. The method becomes inefficient. In the Lanczos method, the construction of the orthonormal basis in the Krylov subspace requires the repetitive actions of the Hamiltonian on the wave function. The contribution of the eigenvectors of the grid-Hamiltonian corresponding to large eigenvalues is quickly growing in the $H^p\Psi$ vector. Even for small p values, this leads to a loss of numerical accuracy. In practice, similarly to the case of SOD, one is then constrained to use very small time propagation steps.

The scheme based on the split-operator technique and Cayley transform used in our studies and expressed in eqs 30–34 appears to be free from the above difficulties.

Aside from the use of the wave packet propagation techniques as a tool to study the properties of (quasi) stationary states in a given system, the calculation of the probabilities of chemical reactions is the most frequently used application of the WPP approach in quantum chemistry (see, e.g., ref 128). More generally, this is connected with application of WPP as a method of extraction of the scattering matrix of the collisional system. We illustrate the possible algorithm on the example of impurity scattering of an electron moving within a continuum of the given image state band n . The potentials are assumed to possess cylindrical symmetry.

We start from the derivation of the formulas for the 2D single channel scattering problem. Using generating series for the Bessel functions J_m , the 2D plane wave can be expanded as

$$\frac{1}{2\pi} e^{i\mathbf{k}_\parallel \mathbf{r}_\parallel} = \sum_{m=-\infty}^{\infty} \frac{i^m}{2\pi} J_m(k\rho) e^{im\varphi} = \sum_{m=-\infty}^{\infty} \frac{i^m}{4\pi} (H_m^{(2)}(k\rho) + H_m^{(1)}(k\rho)) e^{im\varphi} \quad (39)$$

where $\mathbf{k}_\parallel = (k, 0)$ and $\mathbf{r}_\parallel = (\rho \cos \varphi, \rho \sin \varphi)$. $H_m^{(1),(2)}$ are the Hankel functions of the first and second kind corresponding to outgoing and ingoing cylindrical waves, respectively. As a result of the scattering, the solution within each m subspace takes the asymptotic form

$$\phi_m = b_m (H_m^{(2)}(k\rho) + S_m H_m^{(1)}(k\rho)) \quad (40)$$

where S_m is the scattering matrix. Then, setting $b_m = i^m/4\pi$, the total wave function can be expressed as the superposition of incident and scattered waves in the asymptotic region:

$$\Psi(\rho) = \sum_{m=-\infty}^{\infty} \phi_m e^{im\varphi} = \frac{1}{2\pi} e^{i\mathbf{k}_\parallel \mathbf{r}_\parallel} + \mathcal{A}(\varphi) \frac{e^{ik\rho}}{\sqrt{k\rho}} = \frac{1}{2\pi} e^{i\mathbf{k}_\parallel \mathbf{r}_\parallel} + \sum_{m=-\infty}^{\infty} \frac{i^m}{4\pi} (S_m - 1) H_m^{(1)}(k\rho) e^{im\varphi} \quad (41)$$

Using the asymptotic expansion of the Hankel functions, the scattering amplitude $\mathcal{A}(\varphi)$ is given by

$$\mathcal{A}(\varphi) = \sum_{m=-\infty}^{\infty} \frac{1}{4\pi} \sqrt{\frac{2}{\pi}} e^{-i(\pi/4)} (S_m - 1) e^{im\varphi} \quad (42)$$

From eqs 41 and eq 42, we obtain the scattering cross section:

$$\sigma_{el} = \frac{1}{k} \sum_{m=-\infty}^{\infty} |S_m - 1|^2 \quad (43)$$

It is worth mentioning that the 2D scattering cross sections have the dimensionality of length.

The WPP approach to impurity scattering directly stems from eqs 40–43 generalized to multichannel scattering. The incident channel describes an electron moving within the n -th image state continuum, and the other channels correspond to this electron being scattered by the impurity into different 2D surface localized or 3D bulk states. For the extraction of the scattering matrix, we employ the virtual detector method derived in detail in refs 153 and 170. For simplicity, we discuss here the $\Psi_m(\rho, z, t)$ wave function, though the actual calculations are performed with a variable change in the ρ -coordinate (see eqs 35 and 36). Because of the cylindrical symmetry of the potentials, the calculations are performed independently in each m -subspace. The initial wave packet $\Psi_m(\rho, z, t=0)$ is located in the asymptotic region, where the impurity-induced potential is negligible. It is constructed as a Gaussian wave packet in the n -th image state continuum approaching the scattering center with an average parallel momentum k_0 :

$$\Psi_m(\rho, z, t=0) = \frac{1}{\sqrt{\rho}} \exp \left[-ik_0 \rho + \left(\frac{\rho - \rho_0}{\Delta} \right)^2 \right] \chi_n(z) \quad (44)$$

where Δ and ρ_0 are the width and position of the initial wave packet, respectively. The use of a Gaussian initial wave packet allows for the coverage of a range of kinetic energies, whereby the energy dependence of the scattering process is obtained in a single calculation. $\chi_n(z)$ is the wave function of the n -th image state along the surface normal. For the grid of equidistant points in the z -coordinate, $z_j = z_0 + L(j-1)/N_z$ ($j = 1, \dots, N_z$), the wave function $\chi_n(z)$ can be obtained from the direct diagonalization of the Fourier–grid Hamiltonian:^{135,171}

$$H_{jj} = \frac{1}{2} \frac{\pi^2 N_z^2 + 2}{L^2} + V_s(z_j)$$

$$H_{jl} = \frac{1}{2} (-1)^{l-j} \frac{2\pi^2}{L^2} \frac{1}{\sin^2[(j-l)\pi/N_z]}, \quad j \neq l \quad (45)$$

Throughout the course of the time propagation, the $A_j^m(t) = \langle \chi_j(z) | \Psi_m(\rho, z, t) \rangle$ signal is recorded on a virtual detector located at ρ_d far enough from the scattering center. The time-to-energy Laplace transform of $A_j^m(t)$ (cf. eq 20) yields the asymptotic solution:

$$\Phi_j^m(\omega) = b_j^m(\omega) H_m^{(2)}(k_j \rho_d) \delta_{jn} + S_{n \rightarrow j}^m(\omega) H_m^{(1)}(k_j \rho_d) \quad (46)$$

where δ_{jn} is a Kronecker symbol and ω is the total energy of the electron. The electron momentum parallel to the surface, k_j , is given by energy conservation: $k_j^2/2 = \omega - E_j$, with E_j being the energy of the j -th image state at $\bar{\Gamma}$. One immediately recognizes the same structure as eq 40. Thus, for a wave with a given angular momentum, m , the partial probabilities can be calculated as follows below.

Intraband scattering:

$$P_n^{\text{intra}}(\omega, m) = \left| \frac{S_{n \rightarrow n}^m(\omega)}{b_n^m(\omega)} - 1 \right|^2 \quad (47)$$

Interband scattering out of the initial state, n :

$$P_n^{\text{inter}}(\omega, m) = 1 - \left| \frac{S_{n \rightarrow n}^m(\omega)}{b_n^m(\omega)} \right|^2 \quad (48)$$

Final state resolved interband scattering
(transition from band n to band j):

$$P_{n \rightarrow j}^{\text{inter}}(\omega, m) = \left| \frac{S_{n \rightarrow j}^m(\omega)}{b_n^m(\omega)} \right|^2 \quad (49)$$

From eqs 47–49 we obtain the corresponding total cross sections for intraband scattering, interband scattering, and final state resolved interband scattering:

$$\sigma_\gamma^\beta(\omega) = \frac{1}{k_n} \sum_m P_\gamma^\beta(\omega, m)$$

$$(\beta, \gamma) = (\text{intra}, n), (\text{inter}, n), (\text{inter}, n \rightarrow j) \quad (50)$$

In practice, the sum in eq 50 contains a limited number of terms, since the partial probabilities vanish for large enough

values of $|m|$. This can be understood from the fact that the centrifugal barrier $m^2/2\rho^2$ prevents an electron from approaching the scattering center close enough to be scattered.

The WPP scheme in cylindrical coordinates detailed above is well suited to treat local effects, such as, e.g., image state scattering on adatoms. However, in some cases, one is interested in the effect of the ordered adsorbate structures at surfaces. For example, the image potential states are known to be substantially modified by the presence of ordered rare gas layers adsorbed on a surface (see section 5.2 and the article by Höfer *et al.*¹⁷² in this journal issue). In what follows, we discuss the application of the WPP technique to search for the energies at the $\bar{\Gamma}$ point as well as for the energy dispersion of the image potential states (resonances) in these systems.

For ordered adlayers, the total potential V (eq 27) is periodic in the plane parallel to the surface, owing to the periodicity of V_{Ads} . We will consider the simplest case of the square 2D unit cell in the plane parallel to the surface. Generalization to an arbitrary unit cell is straightforward. For such periodic systems, it is convenient to work with an equidistant mesh in 3D Cartesian coordinates $\mathbf{r} = (x, y, z)$. The x and y mesh cover the 2D unit cell area. The z coordinate is defined along the normal to the surface, and the z -mesh covers sufficiently large regions into the vacuum and inside the metal. Exploiting the properties of Bloch states, the wave function can be expressed in the form

$$\Psi(\mathbf{r}, t) = e^{i(K_x x + K_y y)} \psi(\mathbf{r}, t) \quad (51)$$

where $\mathbf{K} = (K_x, K_y, 0)$ is the 2D Bloch wave vector parallel to the surface and $\psi(\mathbf{r}, t)$ is periodic in the x and y coordinates.

The time dependent Schrödinger equation for $\psi(\mathbf{r}, t)$ reads

$$i \frac{\partial \psi(\mathbf{r}, t)}{\partial t} = \underbrace{\left[-\frac{1}{2} \frac{\partial^2}{\partial z^2} - \frac{1}{2} (\nabla_{2D} + i\mathbf{K})^2 \right]}_T \psi(\mathbf{r}, t) + \underbrace{[V_s(z) + V_{\text{Ads}}(\mathbf{r}) + V_{\text{opt}}(z)]}_V \psi(\mathbf{r}, t) \quad (52)$$

where $\nabla_{2D} = (\partial/\partial x, \partial/\partial y, 0)$. The absorbing potential is introduced only at the ends of the z -mesh. When one is interested in the stationary states bound in the z -direction (e.g. image states lying in the projected band gap), care should be taken to set the z -mesh large enough so that V_{opt} does not induce any artificial broadening of the states, i.e., so that V_{opt} does not overlap the stationary state wave functions. Equation 52 is numerically solved via short time propagation with the split-operator technique (cf. eq 30):

$$\psi(\mathbf{r}, t + \Delta t) = e^{-i(\Delta t/2)V} e^{-i\Delta t T} e^{-i(\Delta t/2)V} \psi(\mathbf{r}, t) \quad (53)$$

The pseudospectral method employing a Fourier grid^{131,133} implicitly includes the periodicity constraints and, thus, becomes a quite natural choice in this case. In the basis of plane waves, $\exp(i\mathbf{k}\mathbf{r})$, the T operator defined in eq 52 is diagonal and $\exp(-i\Delta t T) = \exp(-i\Delta t(\mathbf{K} + \mathbf{k})^2/2)$. Then, the procedure defined by eq 53 can be efficiently implemented with successive use of direct and inverse 3D fast Fourier transforms.

The time propagation is initiated with an initial wave function $\psi_0 \equiv \psi(\mathbf{r}, 0)$ satisfying periodic boundary conditions within the 2D unit cell parallel to the surface. The properties of the stationary states ($E(\mathbf{K})$) or of the resonances ($E(\mathbf{K})$),

$\Gamma(\mathbf{K})$) are then extracted from the analysis of the survival amplitude: eqs 22 and 23. It is noteworthy that the approach outlined here can be equally used to calculate the 3D band structures for a known effective one-electron potential.

2.2.2. The Green Function Method

The WPP method reviewed in the previous paragraph allows for the calculation of the evolution time of an electron initially described by a wavepacket Ψ_0 . As already pointed out, in the case of a time independent Hamiltonian, this time evolution can be easily expressed in terms of the Green function of the system. Particularly, the Fourier transform of the survival amplitude or the autocorrelation function of the initial wavepacket $A(t)$ is nothing but the projection of the Green function onto Ψ_0 ,

$$\begin{aligned} \tilde{A}(\omega) &\equiv \lim_{\eta \rightarrow 0^+} \int_0^\infty dt A(t) e^{i(\omega + i\eta)t} \\ &= i \langle \Psi_0 | G^+(\omega) | \Psi_0 \rangle = i G_{00}(\omega) \end{aligned} \quad (54)$$

Notice that $\text{Re}\{\tilde{A}(\omega)\} = -\text{Im}\{G_{00}(\omega)\}$ is proportional to the projected density of states on Ψ_0 . Equation 54 provides an alternative and efficient route for the calculation of the elastic dynamics of electrons. In our case, Ψ_0 is a wavepacket localized in the surface region; then $G_{00}(\omega)$ provides information about the energy position and the width of the surface resonances and/or electronic states associated with adsorbates and defects in the surface.

Most of the standard methods to perform calculations of the electronic structure of surfaces or adsorbates at surfaces rely on the use of relatively thin slabs or finite clusters.¹⁷³ This approximation is justified by the assumption that most surface properties converge rapidly with the number of atomic layers in the slab. Typical examples are, for many systems, the atomic structure and relaxations of the surface layer, the adsorption configuration and energy of small adsorbates, the electronic density in the surface region, etc. Other properties, particularly those dependent on the precise energy position of the electronic levels, converge quite slowly and even show oscillations as a function of the number of layers in the slab. This is due to the confinement of the electronic states in the direction perpendicular to the surfaces of the slabs, causing the discretization of the spectrum. For this reason, we cannot use the electronic eigenfunctions and eigenvalues obtained from the slab to directly calculate the Green function in eq 54. The typical differences between the energy positions of the sub-bands in the slab (approximately $\delta E \sim (\pi/L)^2$ in atomic units, where L is the thickness of the slab in bohrs) are larger than or comparable to the peak widths that we want to resolve in our calculations (for example, a charge-transfer time ≥ 1 fs between an adsorbed atom and the substrate translates to a width of the corresponding resonance ≤ 600 meV). In other words, the energy resolution provided by a slab calculation is insufficient for our purposes.

To avoid these difficulties, we have to calculate the Green's function of the truly semi-infinite system. This can be done using several approaches.^{173,184} We focus here on the method used by the authors in a number of recent publications addressing the elastic width of states associated with adatoms or adlayers on metallic surfaces.^{85,174,183} Since the description of the electronic properties of the system should be as accurate as possible, we use first-principles calculations based on density functional theory to set up the

one-electron Hamiltonian. We combine the information (Hamiltonian matrix elements) from slab and bulk calculations. The use of a basis set localized in real space is instrumental for this purpose. We thus use a linear combination of numerical atomic orbitals as a basis set for our *ab initio* calculations.^{175–177} The Hamiltonian automatically assumes a tight-binding-like form. The matrix elements of the Hamiltonian and the overlap between atoms that are far apart are strictly zero, and the infinite system can be divided into separate “regions” containing a few atomic layers. Each region only interacts with its nearest neighbor regions. The Hamiltonian (and overlap) of the surface region is obtained from the slab, while those of the inner regions (bulk regions) are taken from a bulk calculation using similar parameters.¹⁸³ A common energy reference is set by aligning the Fermi levels of both calculations (this is possible since we typically deal with metals, while for insulators or semiconductors the average potentials should be aligned instead).

We can now use the recursive relation

$$\sum_{ij} G^{ij}(\omega, \mathbf{k}_{\parallel}) [H_{jk}(\mathbf{k}_{\parallel}) - \omega S_{jk}(\mathbf{k}_{\parallel})] = \delta_k^i \quad (55)$$

to obtain the Green function in the surface region for each crystalline momentum parallel to the surface plane, \mathbf{k}_{\parallel} . We always use supercells in the lateral directions, and therefore, \mathbf{k}_{\parallel} is a well defined quantum number in our calculations. The matrix elements of the Green function are defined here such that

$$G(\mathbf{r}, \mathbf{r}', \omega, \mathbf{k}_{\parallel}) = \sum_{ij} G_{ij}(\omega, \mathbf{k}_{\parallel}) \psi_{\mathbf{k}_{\parallel}i}(\mathbf{r}) \psi_{\mathbf{k}_{\parallel}j}^*(\mathbf{r}) \quad (56)$$

where

$$\psi_{\mathbf{k}_{\parallel}i}(\mathbf{r}) = \sum_{\mathbf{R}_{\alpha}} e^{-i\mathbf{k}_{\parallel} \cdot \mathbf{R}_{\alpha}} \phi_i(\mathbf{r} - \mathbf{R}_{\alpha}) \quad (57)$$

are Bloch-like combinations of atomic orbitals $\phi_i(\mathbf{r} - \mathbf{R}_{\alpha})$. $H_{jk}(\mathbf{k}_{\parallel})$ and $S_{jk}(\mathbf{k}_{\parallel})$ are respectively the matrix elements of the Hamiltonian and the overlap matrix in such a basis set. If S denotes the collection of orbitals in the surface region and $n \geq 1$ those in the n -th bulk region (where increasing n indicates increasing the depth into the substrate) we can rewrite eq 55 as a set of the three equations:

$$G^{SS}(\omega) M_{SS}(\omega) + G^{S1}(\omega) M_{1S}(\omega) = \delta_S^S \quad (58)$$

$$G^{SS}(\omega) M_{S1}(\omega) + G^{S1}(\omega) M_{11}(\omega) + G^{S2}(\omega) M_{21}(\omega) = 0 \quad (59)$$

$$G^{S(n-1)}(\omega) M_{(n-1)n}(\omega) + G^{Sn}(\omega) M_{nn}(\omega) + G^{S(n+1)}(\omega) M_{(n+1)n}(\omega) = 0 \quad (60)$$

where $M_{xy}(\omega) = H_{xy} - \omega S_{xy}$. Equation 60 can be solved using the transfer matrix scheme^{178–182} where we write $G^{S(n+1)}(\omega) = G^{Sn}(\omega) T(\omega)$ with T the so-called transfer matrix. The resulting equation is independent of the index n and can be solved by iteration:^{179,180}

$$T(\omega) = (\omega S_{BB'} - H_{BB'}) [(H_{BB} - \omega S_{BB}) + T(\omega) (H_{BB'}^{\dagger} - \omega S_{BB'}^{\dagger})]^{-1} \quad (61)$$

$H_{BB'}$ and $S_{BB'}$ are respectively the Hamiltonian and overlap matrix elements between neighboring bulk regions B and B' . To converge this iteration, it is necessary to evaluate the Green function outside the real axis. We need thus to add a small imaginary part to the energy $\omega + i\eta$. Once $T(\omega)$ is known, all the eqs 58–60 can be solved and $G^{SS}(\omega)$ can be obtained. If the wave packet Ψ_0 is expressed in terms of the numerical atomic orbitals in the surface region $c_0^i \phi_i(\mathbf{r})$, then the projection of the Green function onto this state is given by

$$G_{00}(\omega) = c_0^i S_{ik} G^{kl}(\omega) S_{lj} c_0^j \quad (62)$$

Fitting $\text{Im}\{G_{00}(\omega)\}$ with a collection of Lorentzians $[(\omega - E_j)^2 + (\Gamma_j/2 + \eta)^2]^{-1}$, we can obtain the energies E_j and widths Γ_j of the surface resonances. The width and position of these peaks is independent of the election of Ψ_0 , as long as Ψ_0 has a considerable overlap with the true wave functions of the resonances.

The time evolution of the survival amplitude $A(t)$ can be obtained from $G_{00}(\omega)$

$$\langle \Psi_0 | \Psi(t) \rangle = A(t) = \frac{ie^{+\eta t}}{\pi} \int_{-\infty}^{\infty} d\omega G_{00}(\omega) e^{-i\omega t} \quad (63)$$

Examining $A(t)$ and $|A(t)|^2$ may be quite useful in situations where the structures in $\text{Im}\{G_{00}(\omega)\}$ depart severely from a Lorentzian profile.

2.3. Electron–Phonon Scattering

The phonon-induced lifetime broadening $\Gamma_{e-ph}(\epsilon_{\mathbf{k}_i})$ of an electron state with momentum (\mathbf{k}_i) and energy $\epsilon_{\mathbf{k}_i}$ is related to the Eliashberg $\alpha^2 F_{\mathbf{k}_i}(\omega)$ spectral function through the integral over all the scattering events that conserve energy and momentum^{88,185}

$$\Gamma_{e-ph}(\epsilon_{\mathbf{k}_i}) = 2\pi \int_0^{\omega_m} \alpha^2 F_{\mathbf{k}_i}(\omega) [1 - f(\epsilon_{\mathbf{k}_i} - \omega) + f(\epsilon_{\mathbf{k}_i} + \omega) + 2n(\omega)] d\omega \quad (64)$$

Here, f and n are the Fermi and Bose distribution functions and ω_m is the maximum phonon frequency. The spectral function is given by

$$\alpha^2 F_{\mathbf{k}_i}(\omega) = \sum_{\mathbf{q}, \nu, f} \delta(\omega - \omega_{\mathbf{q}, \nu}) |g(\mathbf{k}_i, \mathbf{k}_f, \mathbf{q}, \nu)|^2 \delta(\epsilon_{\mathbf{k}_i} - \epsilon_{\mathbf{k}_f} \pm \omega_{\mathbf{q}, \nu}) \quad (65)$$

where $g(\mathbf{k}_i, \mathbf{k}_f, \mathbf{q}, \nu)$ is the e–ph matrix element which reflects the probability of an electron scattering from the initial state $\psi_{\mathbf{k}_i}$ and energy $\epsilon_{\mathbf{k}_i}$ to the final state $\psi_{\mathbf{k}_f}$ with energy $\epsilon_{\mathbf{k}_f}$ by the phonon $\omega_{\mathbf{q}, \nu}$. Here \mathbf{q} and ν are respectively the phonon momentum and phonon spectrum branch. The sum in eq 65 is carried out over all final electron states $\psi_{\mathbf{k}_f}$ and all possible phonon modes. The + and – signs in the argument of the δ function correspond to phonon emission and absorption. In the quasielastic approximation (phonon energies are small in comparison with electron energies, and $\omega_{\mathbf{q}, \nu}$ is neglected in $\delta(\epsilon_{\mathbf{k}_i} - \epsilon_{\mathbf{k}_f} \pm \omega_{\mathbf{q}, \nu})$), the Eliashberg function is the same for phonon absorption and emission. This approximation is frequently used in calculations of the e–ph coupling in metals. The e–ph matrix element is

$$g(\mathbf{k}_i, \mathbf{k}_f, \mathbf{q}, \nu) = \left(\frac{1}{2M\omega_{\mathbf{q}, \nu}} \right)^{1/2} \langle \psi_{\mathbf{k}_i} | \hat{\epsilon}_{\mathbf{q}, \nu} \cdot \nabla_{\mathbf{R}} V_{\text{SC}} | \psi_{\mathbf{k}_f} \rangle \quad (66)$$

where M is the atom mass, $\hat{\epsilon}_{q,\nu}$ are the phonon polarization vectors, and $\nabla_{\mathbf{R}}V_{\text{SC}}$ is the gradient of the screened one-electron potential with respect to atom displacements from their equilibrium positions \mathbf{R} .

The strength of the e-ph coupling described by $\lambda_{\mathbf{k}_i}$ is defined as the first reciprocal moment of the Eliashberg function^{86,88}

$$\lambda_{\mathbf{k}_i} = 2 \int_0^{\omega_m} \frac{\alpha^2 F_{\mathbf{k}_i}(\omega)}{\omega} d\omega \quad (67)$$

The value of $\lambda_{\mathbf{k}_i}$ can directly be obtained from the PES (2PPE) measurements of the temperature dependence of the hole (electron) line width of the surface, the image-potential, and the quantum-well states by using the high-temperature asymptotic behavior of the phonon-induced broadening^{24,36,44,70,186–191}

$$\Gamma_{\text{e-ph}} = 2\pi\lambda k_B T \quad (68)$$

This relation is asymptotically exact and does not depend on the model used for the description of the e-ph interaction, since temperature enters the $\Gamma_{\text{e-ph}}$ through the Fermi and Bose distribution functions only.

As follows from eqs 64–68, the calculation of the phonon-induced contribution to the electron (hole) lifetimes or the e-ph coupling parameter requires knowledge of (1) the phonon spectrum characteristics of a material of interest (frequencies, $\omega_{q,\nu}$, and polarizations, $\hat{\epsilon}_{q,\nu}$), (2) the electronic structure quantities (one-electron energies, $\epsilon_{\mathbf{k}}$, and wave functions, $\psi_{\mathbf{k}}$), and (3) the gradient of the one-electron potential evaluated at the ions' equilibrium position, $\nabla_{\mathbf{R}}V_{\text{SC}}$. Phonon frequencies and polarizations can be calculated by using the embedded atom method (examples of these computations can be found in refs 192 and 193), density-functional perturbation theory,^{194–196} or any other lattice dynamics calculation method (for a brief review of these methods, see ref 196). One-electron energies and wave functions can be obtained from density functional theory (DFT) or some model Hamiltonian electronic structure calculations. An example of a model potential widely used for the past decade in the theoretical study of the dynamics of excited electrons (holes) in surface and image-potential states on metal surfaces is the one-dimensional potential of refs 157 and 197. The gradient of the one-electron potential can be computed within density functional theory^{194,195} or by using a screened model pseudopotential.^{24,185} In sections 3 and 4 we give examples of the e-ph calculations for both bulk and surface excited electrons and holes.

For fast estimations of the phonon-induced contribution to the excited electron decay rate, the so-called Debye model is frequently used.^{24,37,70,188,189,198–204} In this model, the e-ph coupling matrix element, $g(\mathbf{k}_i, \mathbf{k}_f, \mathbf{q}, \nu)$, is assumed to be constant and, therefore, the Eliashberg function is determined by the phonon density of states. In this case, the Eliashberg function and phonon-induced contribution are given for a bulk (3D) Debye model as

(a) $\epsilon = \omega < \omega_D$

$$\alpha^2 F(\omega) = \lambda \omega^2 / \omega_D^2 \quad (69)$$

$$\Gamma_{\text{e-ph}} = \frac{2\pi\hbar\lambda\omega_D}{3} \left(\frac{\omega}{\omega_D}\right)^3 \quad (70)$$

(b) $\epsilon = \omega > \omega_D$

$$\alpha^2 F(\omega) = 0 \quad (71)$$

$$\Gamma_{\text{e-ph}} = 2\pi\hbar\lambda\omega_D/3 \quad (72)$$

For a 2D Debye model, one obtains for electron energies

(a) $\epsilon = \omega < \omega_D$

$$\alpha^2 F(\omega) = \frac{\lambda\omega}{2\omega_D} \quad (73)$$

$$\Gamma_{\text{e-ph}} = \frac{\pi\hbar\lambda\omega_D}{2} \left(\frac{\omega}{\omega_D}\right)^2 \quad (74)$$

(b) $\epsilon = \omega > \omega_D$

$$\alpha^2 F(\omega) = 0 \quad (75)$$

$$\Gamma_{\text{e-ph}} = \pi\hbar\lambda\omega_D/2 \quad (76)$$

In eqs 69–76, ω_D is the characteristic Debye frequency of a metal.

2.4. Collective Excitations

Information on the surface collective excitations can be obtained from the imaginary part of the surface response function $g(\mathbf{q}_{\parallel}, \omega)$, defined as^{205,206}

$$g(\mathbf{q}_{\parallel}, \omega) = \int d\mathbf{r} n_{\text{ind}}(\mathbf{r}, \omega) e^{q_{\parallel} z} \quad (77)$$

where $\mathbf{r} \equiv \{\mathbf{r}_{\parallel}, z\}$, \mathbf{q}_{\parallel} is a 2D momentum parallel to the surface, $q_{\parallel} = |\mathbf{q}_{\parallel}|$, and $n_{\text{ind}}(\mathbf{r}, \omega)$ is the charge density induced at the crystal surface by an external potential of the form

$$V_{\text{ext}}(\mathbf{r}, \omega) = -\frac{2\pi}{q_{\parallel}} e^{q_{\parallel} z} e^{i\mathbf{q}_{\parallel} \mathbf{r}_{\parallel}} e^{-i\omega t} \quad (78)$$

The so determined g can depend, in principle, on both the value and direction of the two-dimensional momentum \mathbf{q}_{\parallel} .

In time-dependent density functional theory,²⁰⁷ n_{ind} and V_{ext} are related by the equation

$$n_{\text{ind}}(\mathbf{r}, \omega) = \int d\mathbf{r}' \chi(\mathbf{r}, \mathbf{r}', \omega) V_{\text{ext}}(\mathbf{r}', \omega) \quad (79)$$

The response function $\chi(\mathbf{r}, \mathbf{r}', \omega)$ satisfies the integral equation 9 which relates it with the response function of a noninteracting electron system χ^0 .

At the surface, translational symmetry in the direction perpendicular to the surface is broken. To deal with this problem, the so-called slab geometry is frequently employed. In such an approach, the slabs containing several (normally up to several tens of) atomic layers are separated by vacuum intervals and periodically repeated in the direction normal to the surface. The slab geometry imposes some low momenta limit below which the surface plasmon begins to split into two slab excitations $\omega_{\pm}(\mathbf{q}_{\parallel}) = \omega_{\text{sp}}(1 \mp e^{-q_{\parallel}L})^{1/2}$ (refs 205, 208, and 209) (where L is the slab thickness). This drawback can be relieved by increasing the slab thickness.

Then, performing a Fourier transformation, $\chi^0(\mathbf{r}, \mathbf{r}', \omega)$ can be expressed via matrix elements given by

$$\chi_{\mathbf{G}, \mathbf{G}'}^0(\mathbf{q}_{\parallel}, \omega) = \frac{2}{S} \sum_{\mathbf{k}_{\parallel}} \sum_{n, n'} \frac{\theta(E_F - \epsilon_{\mathbf{k}_{\parallel}, n}) - \theta(E_F - \epsilon_{\mathbf{k}_{\parallel} + \mathbf{q}_{\parallel}, n'})}{\epsilon_{\mathbf{k}_{\parallel}, n} - \epsilon_{\mathbf{k}_{\parallel} + \mathbf{q}_{\parallel}, n'} + (\omega + i\eta)} \times \\ \langle \psi_{\mathbf{k}_{\parallel}, n} | e^{-i(\mathbf{q}_{\parallel} \mathbf{r}_{\parallel} + \mathbf{G} \cdot \mathbf{r})} | \psi_{\mathbf{k}_{\parallel} + \mathbf{q}_{\parallel}, n'} \rangle \langle \psi_{\mathbf{k}_{\parallel}, n'} | e^{i(\mathbf{q}_{\parallel} \mathbf{r}_{\parallel} + \mathbf{G}' \cdot \mathbf{r})} | \psi_{\mathbf{k}_{\parallel}, n} \rangle \quad (80)$$

where the second sum runs over the band structure for each wave vector \mathbf{k}_{\parallel} in the first surface Brillouin zone (SBZ), $\epsilon_{\mathbf{k}_{\parallel}, n}$ represents the one-particle eigenvalues, and $\psi_{\mathbf{k}_{\parallel}, n}$ represents the corresponding eigenfunctions of the ground state, evaluated with the use of an *ab initio* self-consistent pseudopotential method within the local density approximation. S is a normalization area. Further calculation details can be found in ref 210. By performing a Fourier transformation, one can finally obtain the next expression for the surface response function

$$g(\mathbf{q}_{\parallel}, \omega) = -\frac{2\pi}{q_{\parallel}} \int dz \int dz' \chi_{\mathbf{G}_{\parallel}=0, \mathbf{G}'_{\parallel}=0}(z, z', \mathbf{q}_{\parallel}, \omega) e^{q_{\parallel}(z+z')} \quad (81)$$

Although in this formula only the χ matrix elements with parallel components of reciprocal wave vectors equal to 0 enter, the full three-dimensional dependence of χ on \mathbf{r} and \mathbf{r}' is implicitly presented through the evaluation of the integral equation (eq 9). However, these calculations are rather computer time demanding. Therefore, in the case of small crystal local-field effects, it is better to perform calculations of the $\chi_{\mathbf{G}, \mathbf{G}'}^0(\mathbf{q}_{\parallel}, \omega)$ matrix for the $\mathbf{G}_{\parallel} = \mathbf{G}'_{\parallel} = 0$ components only. This drastically reduces the computational time. The effectiveness of this approach has recently been demonstrated for the case of Mg(0001) and Al(111) surfaces in refs 210 and 211, respectively.

In the case of the use of surface potentials which vary in the direction normal to the surface only, the calculations are greatly simplified due to the spatial invariance of the problem in the plane parallel to the surface, and $g(\mathbf{q}_{\parallel}, \omega)$ of eq 77 reduces to the $g(q_{\parallel}, \omega)$ form, which depends on the value of q_{\parallel} only²⁰⁵

$$g(q_{\parallel}, \omega) = \int dz n_{\text{ind}}(z, q_{\parallel}, \omega) e^{q_{\parallel} z} \quad (82)$$

where

$$n_{\text{ind}}(z, q_{\parallel}, \omega) = \int dz' \chi(z, z', q_{\parallel}, \omega) V_{\text{ext}}(z', q_{\parallel}, \omega) \quad (83)$$

The RPA interacting density-response function $\chi(z, z', q_{\parallel}, \omega)$ is calculated along the lines described in refs 212 and 213.

3. Electron Excitations in Bulk Para- and Ferromagnetic Metals

We start the discussion of decay mechanisms of low-energy single-particle excitations in metals in terms of creation of electron–hole pairs. This mechanism, schematically illustrated in Figure 4, is the basic one in metals. Moreover, for the majority of paramagnetic metals, this is the unique electronic decay mechanism in the energy interval from ≈ -3 eV to ≈ 3 eV with respect to E_F . The decay of low-energy excited electrons and holes is not affected by plasmon excitations since the energy of these excitations is

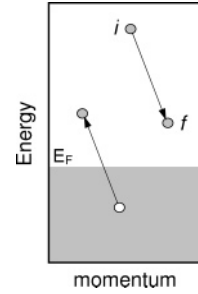


Figure 4. Decay of an excited electron with the creation of an electron–hole pair. Filled circles indicate electrons, and an open circle denotes a hole.

far beyond the low-energy interval. Typical examples of such metals are Al and Be, where bulk plasmon energies are of the order of 15 and 19 eV, respectively. Even in Ag, where the plasmon energy is of the order of ≈ 4 eV,²¹⁴ the low-energy single-particle excitations are not influenced by this very narrow plasmon peak. In ferromagnetic metals, we analyze how spin-flip processes affect the decay of spin-dependent low-energy excitations.⁸¹ We also analyze the phonon-induced contribution to the inverse lifetime of excited electrons and holes in metals which have recently been studied.^{223,246}

3.1. Simple Metals

In simple metals, electron–ion interaction is weak; hence, the electronic structure and electron state widths of these metals can be well approximated within the free electron gas model. The first calculations of the electron width (the decay rate of an excited electron or the inverse lifetime) were performed by Lindhard,²¹⁵ Quinn and Ferrell,⁶⁸ and Ritchie.²¹⁶ Recently, the role of multiple electron–hole scattering for the lifetime of the excited electrons and holes in the free electron gas model was studied in the framework of the GW+T approximation.¹⁰⁴ For very simple metals, *ab initio* GW calculations of *excited electron* lifetimes have been performed for Al,^{82,217–221} Be,^{219,222,223} Mg,²¹⁹ Na,²²⁴ and K.²²⁴ It was found that in all these metals, except for Be, the evaluated inverse lifetimes do not depend strongly on momentum and show approximately quadratic energy scaling, $\Gamma_{e-e} \sim (E - E_F)^2$, predicted within Fermi-liquid theory. In Be, in contrast, Γ_{e-e} strongly deviates from the quadratic energy dependence at certain points and directions of the Brillouine zone (BZ). This deviation was explained by the nonfree electron-like behavior of the electron bands (Figure 5, bands T_4 , Σ_1 , and S'_1) along certain symmetry directions and at symmetry points.^{219,223} *Excited hole* lifetimes have been calculated using the GW approximation for Al²²⁰ and Be.²²³ It was shown that in Al the hole inverse lifetime can be well approximated by quadratic scaling: $\Gamma_{e-e} \sim (E - E_F)^2$. For Be the low-energy excited hole inverse lifetimes deviate from the quadratic scaling along some symmetry directions.²²³ Later calculations done for Al have also included multiple-scattering terms (T-matrix contribution) in the self-energy.⁸² However, despite the change of the inverse lifetime values with respect to the GW results, this inclusion did not change the quadratic scaling of the Γ_{e-e} .

It is commonly accepted that the e–ph contribution Γ_{e-ph} to the decay rate Γ is very important for electron (hole) energies close to E_F , more exactly for energies $E \leq |\hbar\omega_D - E_F|$. However, first-principles calculations of Γ_{e-ph} performed

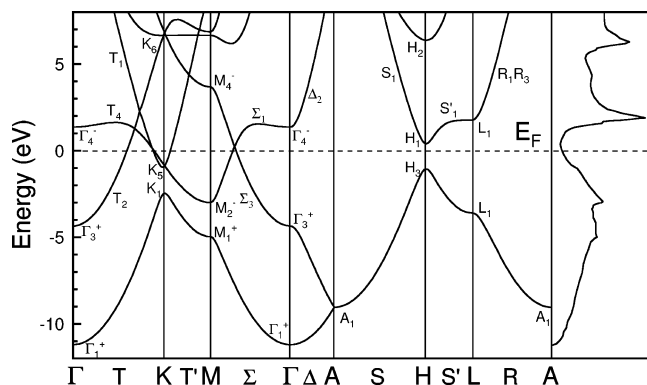


Figure 5. LDA energy bands along the symmetry directions and density of electron states (right panel) for hcp Be.

Table 1. Total Line Width, $\Gamma_{\text{tot}} = \Gamma_{\text{e-ph}} + \Gamma_{\text{e-e}}$, Electron-Phonon, $\Gamma_{\text{e-ph}}$, and Electron-Electron, $\Gamma_{\text{e-e}}$, Contributions for Certain States at the Γ , M, and L Points for Bulk Be^a

state	ϵ^{LDA}	$\Gamma_{\text{e-ph}}$	$\Gamma_{\text{e-e}}$	Γ_{tot}
Γ_3^+	-4.28	13	124	137
Γ_4^-	1.19	18	1	19
M_1^+	-4.87	40	189	261
M_2^-	-3.07	22	84	117
M_4^-	3.54	16	80	78
L_1	-3.54	38	78	105
L_1	1.55	76	3	77

^a These values are in millielectronvolts. The second column denotes the LDA eigenvalues (in eV).

in Be²²³ for certain symmetry points and symmetry directions in the BZ have shown that, even for energies $E \geq |\hbar\omega_D - E_F|$, $\Gamma_{\text{e-ph}}$ can be comparable with $\Gamma_{\text{e-e}}$ or, in some cases, can be much bigger than $\Gamma_{\text{e-e}}$. In Table 1 we compare the phonon-induced lifetime broadening, $\Gamma_{\text{e-ph}}$, at $T = 0$ with the e-e contribution for some selected electron states at the Γ , M, and L symmetry points. In general, the line width due to the e-ph scattering is smaller than that induced by the e-e interactions. For the electron states Γ_3^+ and M_1^+ , the e-e contribution is nearly 1 order of magnitude larger. However, for some electron states, such as Γ_4^- and L_1 (above the Fermi level), $\Gamma_{\text{e-ph}}$ is much larger than $\Gamma_{\text{e-e}}$, since for these states the e-e contribution is very small. This is explained by the absence of final electron states with relatively small momenta for the electron (hole) decay while for large momenta the decay probability is small. As for the e-ph interaction, analysis of the spectral function (eq 65) showed that the Eliashberg function in Be is dominated by high-frequency peaks of the phonon spectrum which are determined by optical phonons while the low-energy peak in the phonon density of states is completely suppressed by the e-ph matrix elements.²²³ These optical phonons favor the large contribution to the e-ph coupling that in turn results in a small lifetime of quasiparticles in these states despite the negligible values of the e-e scattering. For higher temperatures, the changes in the e-ph contribution depend on the value of the e-ph coupling parameter $\lambda_{\mathbf{k},i}$. As a rule, they are not very large, which is consistent with the rather weak e-ph coupling that is observed in hcp Be. Thus, at room temperature, the e-ph contributions to the line width for the M_1^+ , M_2^- , and M_4^- electron states are found to be 48, 28, and 20 meV, respectively. As one can see, they remain smaller than the line widths due to the e-e scattering for the same states, which do not depend on temperature.

3.2. Noble Metals

The electronic structure of noble metals is more complicated than that of simple metals. Electronic spectra of simple metals consist of sp symmetry bands²²⁵ while in noble metals electronic structure consists of two groups of bands (as an example, see Figure 1 for the band structure of Cu and ref 225): (1) unoccupied and occupied bands of sp symmetry up to an energy of -2 eV (-4 eV) with respect to E_F for Cu and Au (Ag); (2) narrow occupied bands of d symmetry with lower energies (except for the lowest states of s symmetry). The distinction in symmetry and different behavior in real space (the maximum of the d state wave function is much closer to the nucleus position than that of the sp state) leads to a qualitatively different energy and momentum dependence of $\Gamma_{\text{e-e}}$ ($\tau_{\text{e-e}}^{-1}$) for these two groups of electron states.²²⁶ We start from the sp unoccupied states. At first glance, the excited electrons in these states can be considered as free-like electrons with a decay rate which scales with energy as $\Gamma_{\text{e-e}} \sim (E - E_F)^2$. Indeed, all first-principles calculations for excited electron lifetimes in Cu, Ag, and Au give this scaling.^{217–219,226,230} However, as was shown in ref 218, the d-electrons lead to the increase of $\tau_{\text{e-e}}$ as compared to the case of the free electron gas model. Primarily, this effect is due to the contribution of the d electrons to the screening of the electron-electron interaction $W(\mathbf{r}, \mathbf{r}', w_{ij})$. A similar effect takes place for holes excited in the sp states. Very different decay occurs for holes in d states of noble metals.^{226–229} In Figure 6 we show the calculated lifetimes for holes in both the sp and d bands of these metals. From this figure one can conclude that (1) d hole lifetimes strongly deviate from the inverse quadratic scaling typical for the free electron gas model; (2) for the same energy, d hole lifetimes are much longer than the sp hole lifetimes; and (3) d hole lifetimes show very clearly the effect of the band structure.²²⁶ All three of these features are most pronounced for the upper d bands, where the hole decay is mostly determined by electron transitions from sp occupied bands. These transitions contribute only slightly to $\Gamma_{\text{e-e}}$ due to different symmetries of the sp and d states and their different localization in real space. In Figure 7 we compare the calculated^{228,229} and measured^{231–233} lifetimes for holes in the upper d bands at a few symmetry points in the BZ for Cu. One can see that the experimental data on the lifetime of the $X_{7+(5)}$ state are in good agreement with the lifetime values obtained from the full potential linear muffin-tin orbital (FP LMTO) GW calculation.²²⁹ For energies lower than that of the X_5 state, the FP LMTO GW lifetimes evaluated at the symmetry points are close to the results obtained from the pseudopotential method based on plane-wave basis set (PPW) GW computations.²²⁸ However, the experimental lifetimes demonstrate a sharp decrease near the top d band energy, and all the calculated lifetimes so far appear to be longer than the experimental ones.

The importance of multiple electron-hole scattering processes (T-matrix) for excited electron lifetimes can be illustrated by using recent calculation results for the inelastic mean free path (IMFP) in Au.²³⁴ The inelastic mean free path of an excited electron in the state $\psi_{\mathbf{k},i,\sigma}$ with momentum \mathbf{k} , band index i , spin σ , and energy $\epsilon_{\mathbf{k},i,\sigma}$ is defined as the distance the electron travels during its inelastic lifetime $\tau_{\mathbf{k},i,\sigma}$, i.e., $\lambda_{\mathbf{k},i,\sigma} = \tau_{\mathbf{k},i,\sigma} \mathbf{v}_{\mathbf{k},i,\sigma}$. The group velocity is defined as $\mathbf{v}_{\mathbf{k},i,\sigma} = \partial \epsilon_{\mathbf{k},i,\sigma} / \partial \mathbf{k}$. Normally the IMFPs deduced from experiments are resolved in energy and spin, and not in momentum;

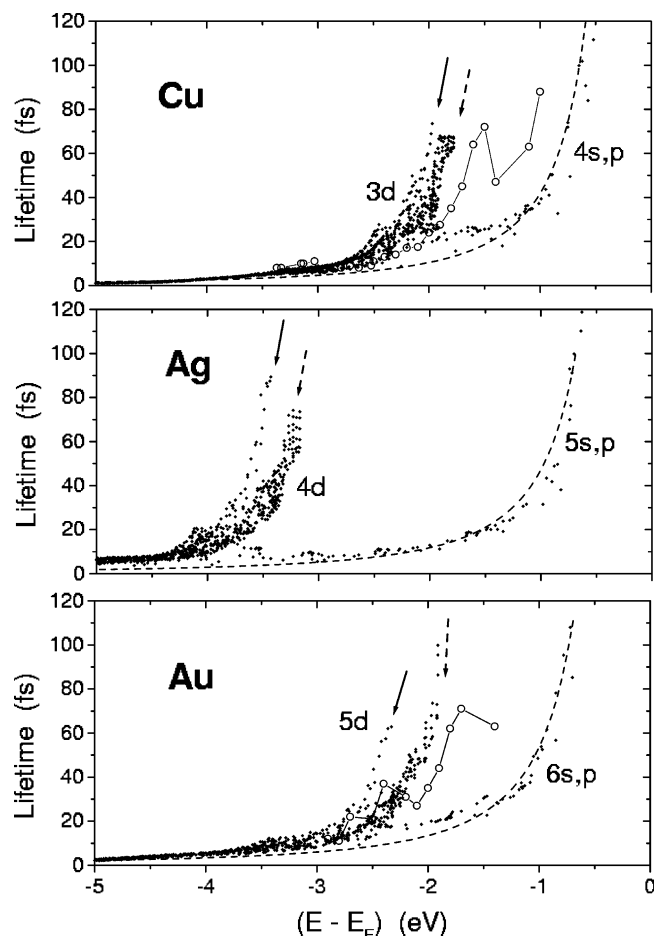


Figure 6. Calculated LMTO GW hole lifetimes (solid diamonds)²²⁶ in the sp and d states of noble metals. Open circles depict the evaluated data of ref 227. Dashed lines indicate the results of free electron gas theory. The solid arrow shows d hole lifetimes along the XL direction while the dashed arrow indicates d hole lifetimes along the WX direction.

therefore, for the comparison with experimental data, we present here the computed momentum-averaged lifetimes $\tau_o(E)$, group velocities $v_o(e)$, and IMFP $\lambda_o(E) = v_o(e) \tau_o(E)$.

In Figure 8 we show the averaged IMFP's in Au calculated within the GW and GW+T approaches and compare them with the GW IMFP in Pt. In Au at the excitation energy of about 1 eV, the IMFP obtained from the GW calculations is equal to 1300 Å, that is, much longer than the IMFPs deduced from photoemission experiments,²³⁵ 220–230 Å, and from BEEM measurements,²³⁶ 230–280 Å. The inclusion of the T-matrix terms gives a IMFP of approximately 470 Å; that is, multiple e–h scattering processes essentially improve the agreement between theory and experiment. The IMFPs in Pt appear to be much shorter than those in Au, even when the T-matrix effects are included in the calculations for Au. This can be explained in terms of the electronic structure of Pt. The band structure of Pt is very similar to the band structure of Pd (see subsection 3.3). In both metals, it is characterized by the high density of d states in the vicinity of the Fermi level. Therefore, the decay of an electron from these states to unoccupied d states is efficient (as discussed above for holes in noble metals) and results in IMFPs which are shorter than those in Au.

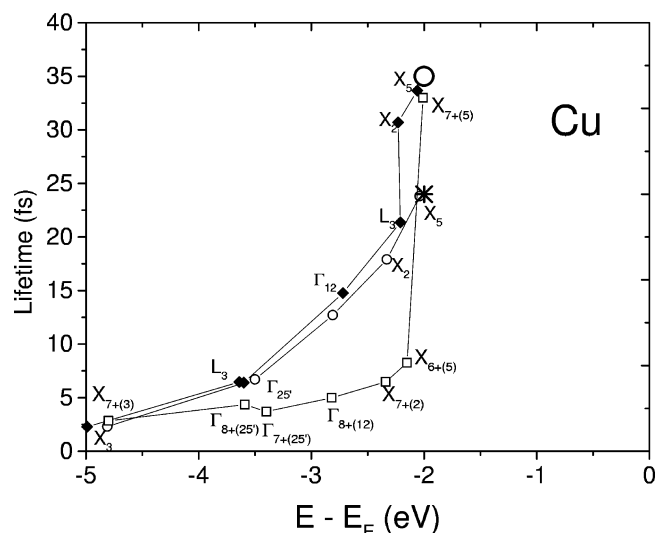


Figure 7. Calculated and experimental d hole lifetimes in some symmetry points of the Brillouin zone.²²⁹ Open squares are the experimental data of ref 233. A big open circle and a star are the TR-2PPE measured results of refs 231 and 232, respectively. Solid diamonds are the results of the FP LMTO GW calculation,²²⁹ and open circles are the data of the PPW GW evaluation.²²⁸ To provide comparison with the PPW GW and experimental data, the FP LMTO results have been shifted by -0.4 eV.

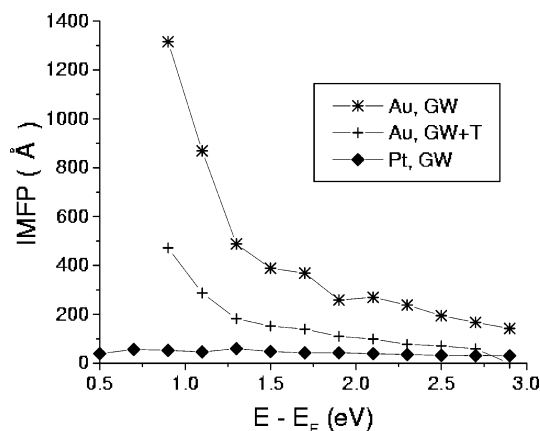


Figure 8. IMFPs (in Å) in Au and Pt as calculated within the GW and GW+T approaches.

3.3. Paramagnetic Transition Metals

The electronic structure of transition metals is characterized by d bands at and around E_F . As an example, we show in Figure 9 the band structure of palladium along symmetry directions together with the corresponding electron density of states. The latter shows a pronounced peak at E_F determined by d electrons. In other transition metals, this peak is shifted up to higher energies.²²⁵ This feature (d states at and above E_F) distinguishes transition metals from both simple and noble metals and leads to very distinct lifetimes in transition metals. In general, lifetimes in these metals are significantly shorter than those in simple and noble ones. This can be explained in terms of distinct density of states. In noble metals, the electronic structure in the energy interval 0–4 eV above E_F consist of 1–2 sp bands while in transition metals the band structure at these energies consists of 2–5 d bands. The bigger number of final states increases the efficiency of the electron decay and, thus, reduces the lifetime.

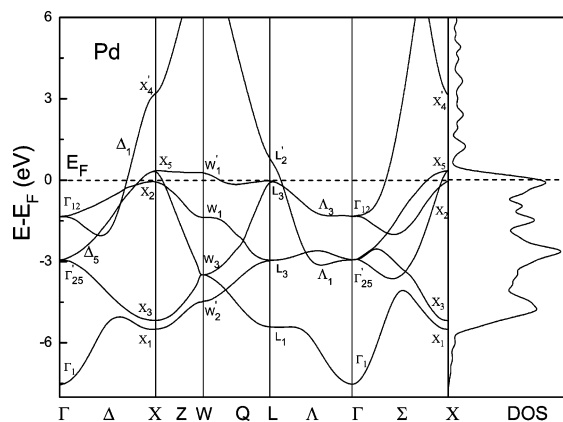


Figure 9. Electron energy bands for bulk Pd. The right panel shows the density of states.

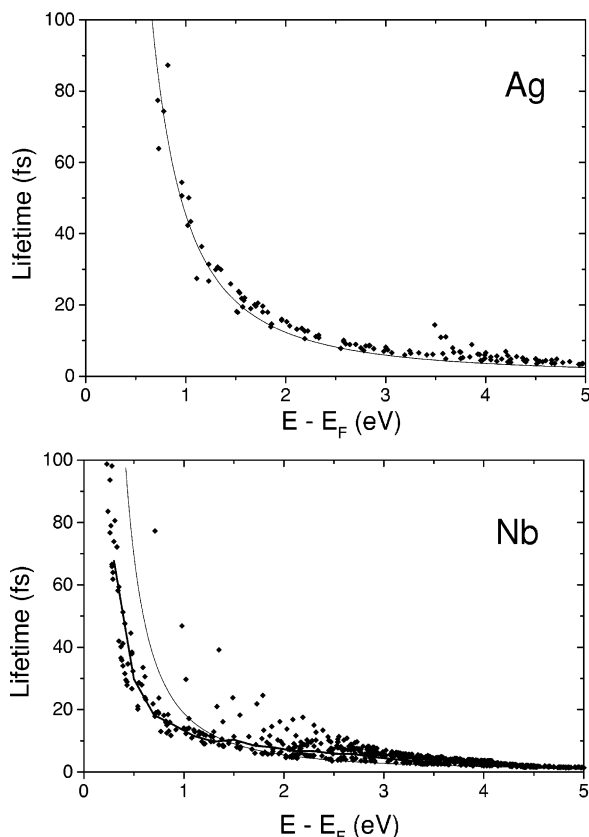


Figure 10. Electron lifetimes (less than 100 fs) in Ag (upper panel) and Nb (lower panel) as calculated by the LMTO RPA GW method are shown by solid diamonds.²³⁷ In the upper panel, the solid line depicts the free electron gas model with $r_s = 2.1$. In the lower panel, the momentum-averaged LMTO GW lifetimes are depicted by the thick solid line, whereas the thin solid line represents the lifetimes calculated by the free electron gas model with $r_s = 3.1$. The momentum dependence (anisotropy) of the lifetime is reflected by different positions of solid diamonds at the same energy.

Only a few many-body GW calculations of electron and hole lifetimes in transition metals have been published to date.^{221,237,240,242} Very recently, GW+T evaluations of excited electron lifetimes have been done for Pd and Ta.^{82,245} The general conclusion from all the calculations done is that, in contrast to the cases of simple and noble metals, the excited electron lifetimes in transition metals show a strong momentum dependence.^{221,237} We illustrate this effect in Figure 10, where momentum and energy resolved lifetimes are presented for electrons in Ag and Nb. As follows from the

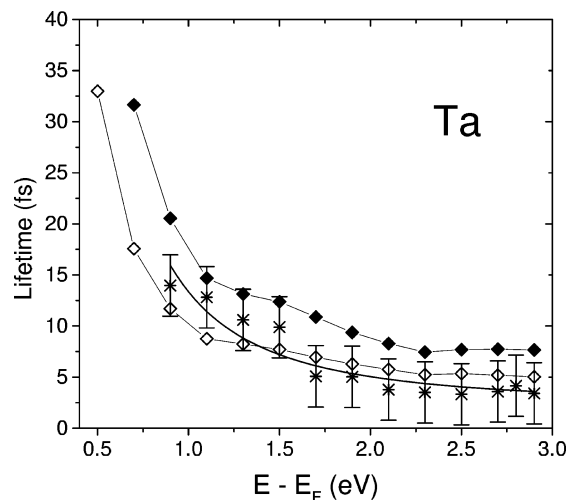


Figure 11. Experimental and momentum-averaged electron lifetimes in Ta versus excitation energy:²⁴⁵ (solid diamonds) theoretical momentum-averaged GW lifetimes; (open diamonds) theoretical momentum-averaged GW+T lifetimes; (stars) experimental data, shown together with the error bars. The thick solid line is a guide for the eye.

figure in Ag, the momentum dependence of the electron lifetime is much weaker than that in Nb. This can be attributed to a much stronger momentum anisotropy of the band structure of transition metals compared to that in noble ones. In Figure 11 we compare the TR-2PPE experimental data for the excited electron lifetimes in Ta with the lifetimes obtained from the GW and GW+T calculations.²⁴⁵ This comparison shows that the multiple scattering between holes and electrons included in the T -matrix produces noticeable contributions to the fast electrons' decay. For excitation energies higher than 1.6 eV, we find a very good agreement between experimental relaxation times and GW+T theoretical lifetimes. Below 1.6 eV, the experimental relaxation times are higher than the theoretical data. This can be attributed to cascade effects which are important for excited electrons at these energies.²⁴⁵

The role of the e-ph interaction in the excited electron and hole decay in transition metals has been studied in *ab initio* calculations of the e-ph coupling parameter λ , the Eliashberg spectral function, and the Γ_{e-ph} contribution by using Pd as an example.²⁴⁶ Sklyadneva *et al.*²⁴⁶ have shown that e-ph coupling is significantly stronger for both occupied and unoccupied d states than for sp unoccupied states. The strong “d band”—phonon coupling is dominated by low-frequency phonons while high-frequency phonons are suppressed by e-ph matrix elements (eq 66). It is a typical feature of transition metals caused by the coupling of d electrons to transverse phonon modes.²⁴⁷

3.4. Ferromagnetic Metals

Additional mechanisms to the ones discussed above of quasiparticle decay related with energy relaxation arise in ferromagnetic metals. In these materials, the majority- (spin up) and minority- (spin down) spin electrons form two subsystems and the decay of an electron with a certain direction of spin (up or down) can be accompanied by the creation of a Stoner pair (an electron with one direction of spin and a hole with the opposite spin direction) or/and magnon excitation. In Figure 12 we schematically show the decay mechanisms for an excited electron. We discuss these mechanisms by using recent calculations for Fe and Ni.^{81,248}

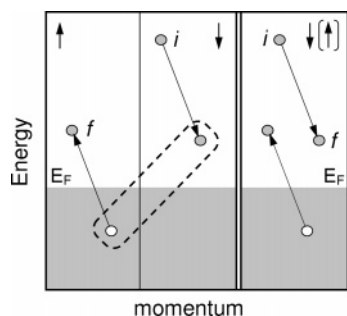


Figure 12. Left panel: decay of the excited spin-down electron in the minority band with the creation of an electron–hole pair in the majority band. The Stoner pair is in the rectangle pictured by the dashed line. Right panel: decay of the excited spin-down (up) electron in the minority (majority) band with the creation of an electron–hole pair in the same band.

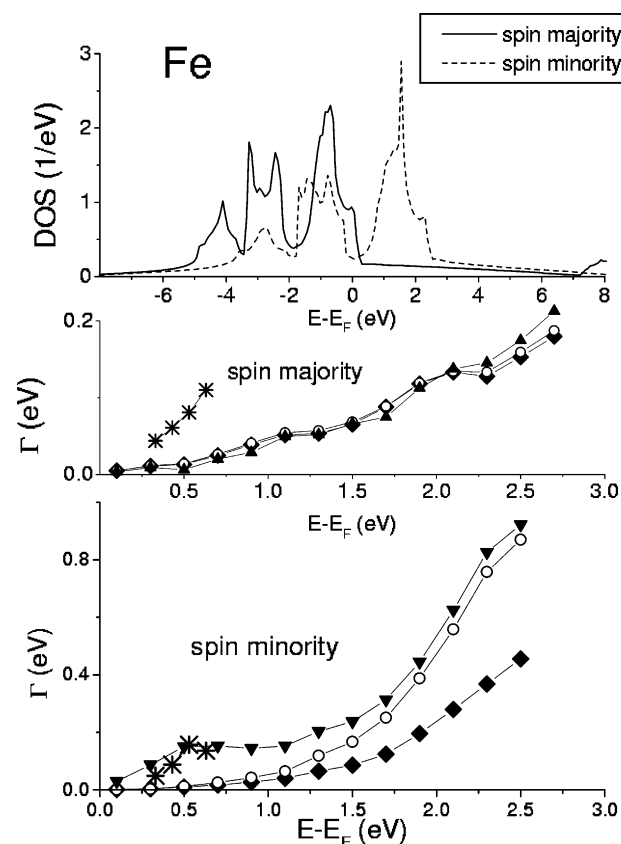


Figure 13. Calculated⁸¹ and experimental inverse lifetimes of excited electrons in Fe. Solid diamonds show the GW contribution to Γ , open circles show the GW+T non-spin-flip contribution, and black triangles show the complete GW+T (non-spin-flip + spin-flip) Γ -values. Stars show the experimental inverse lifetimes of refs 100 and 249.

In Figures 13 and 14 we show the calculated spin-projected densities of states as well as the GW and GW+T momentum-averaged inverse lifetimes, Γ , for Fe and Ni, respectively. Within the GW+T formalism, the contribution of non-spin-flip processes to the inverse lifetimes is described by the GW term and by the T -matrix term with $\sigma_1 = \sigma_2$ whereas the spin-flip contributions follow from the T -matrix term with $\sigma_1 \neq \sigma_2$.⁸¹ The spin-flip part of the inverse lifetime for an excited electron in the state $\psi_{\mathbf{q},i,\sigma}$ is determined by the unoccupied states $\psi_{\mathbf{k},n',-\sigma}$ with lower energy and opposite spin and by the transition probabilities between the $\psi_{\mathbf{q},i,\sigma}$ and the $\psi_{\mathbf{k},n',-\sigma}$ states weighted by $\text{Im } T_{\sigma,-\sigma}(\omega)$ at energy $\omega = \epsilon_{\mathbf{q},i,\sigma} - \epsilon_{\mathbf{k},n',-\sigma}$.⁸¹ In the case of Fe, the GW calculation

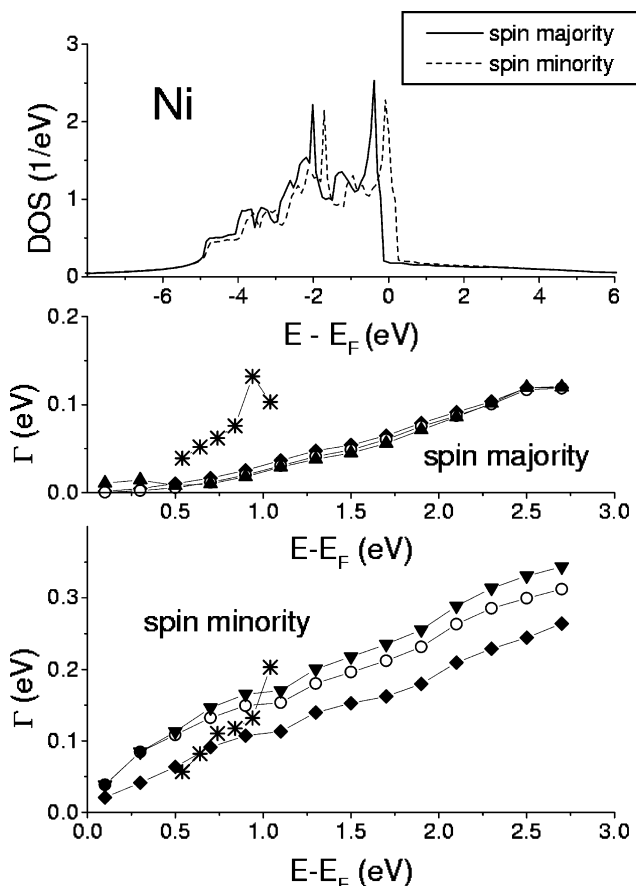


Figure 14. Calculated⁸¹ and experimental^{100,249} inverse lifetimes of excited electrons in Ni. Notations are as in Figure 13.

disagrees with measurements¹⁰⁰ for both directions of spin (Figure 13). The inclusion of the non-spin-flip contribution (electron decay in the same spin channel, right panel of Figure 12) from the T -matrix strongly increases the line width of the spin minority state for energies larger than 1 eV, while for smaller energies the spin-flip processes (electron decay via creation of the Stoner pair and excitation of magnon, left panel of Figure 12) dominate, resulting in good agreement with the measured line width. For the spin majority states, the T -matrix contribution is small and does not modify the results obtained from the GW calculations. This disagrees with the experiment but it is well compatible with the Fe band structure: the transitions from 3d ($\sigma = -1/2$) \rightarrow 4p ($\sigma = 1/2$), which accompany the de-excitations of spin-majority electrons, result in a small contribution to the spin-majority line width due to the small density of 4p_{1/2} states at all energies.⁸¹ Similar to the case of Fe, for the spin majority states in Ni the effect of the electron–hole multiscattering processes is also small while for the spin-minority states the situation is different. For the latter states, the difference between the GW and the GW+T inverse lifetimes is mostly due to the non-spin-flip multiple scattering processes. The contribution from the spin-flip processes is small.

The inelastic lifetimes, calculated for Fe and Ni within the GW+T approach,⁸¹ have been employed in order to also calculate the spin-resolved inelastic mean free path.²³⁴ The main results of these calculations are shown in Figure 15. Both experimental and theoretical data demonstrate a big spin asymmetry of IMFPs in Fe and Ni: $\lambda_{\text{spin-up}} \gg \lambda_{\text{spin-down}}$. This is an important property used in spintronic devices, e.g., spin-valve transistors and magnetic tunnel transistors, to realize the switching of current depending on the direction

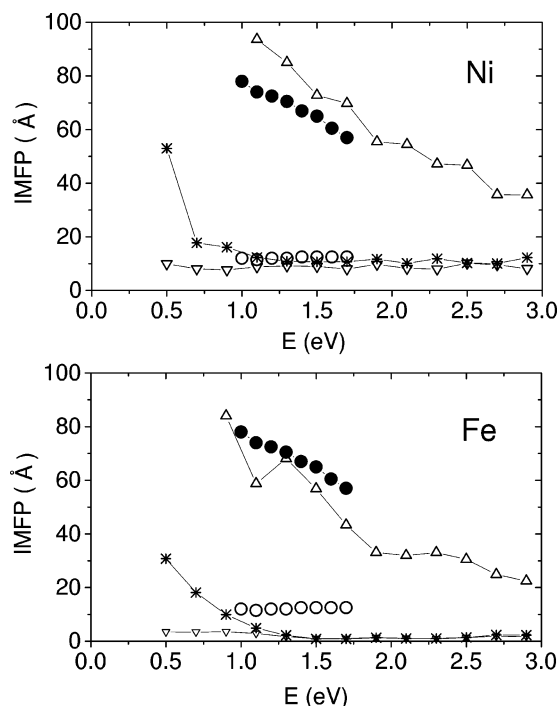


Figure 15. Spin-resolved inelastic mean free path in Ni and Fe calculated within the GW and GW+T approaches. Up triangles show spin-majority IMFP from the GW calculations; down triangles show the spin-minority GW IMFP corrected for T-matrix effects. Stars show the GW results for the spin-minority electrons without T-matrix corrections. Solid (open) circles are experimental data for the spin-majority (-minority) electrons in the Ni₈₀Fe₂₀ alloy from ref 238.

of the applied magnetic field.²³⁹ The calculation results for Ni agree well with experimental data for permalloy Ni₈₀Fe₂₀ (experimental data for pure Ni and Fe are absent). The T-matrix effects (i.e. generation of Stoner's pairs and spin waves in Fe and non-spin-flip multiple scattering in Ni) appear to be important at the energy of excited electron below 1 eV, whereas above 1 eV, i.e., in the energy region important for spintronic devices, the IMFP is well described within the GW approach.

3.5. Comparison of Theoretical and Experimental Lifetimes

Theoretical and experimental results on the study of excited electron lifetimes in simple, noble, and transition metals are summarized in Table 2. The momentum averaged lifetimes, $\tau_{e-e}(E)$, obtained from *ab initio* GW and GW+T calculations, are shown together with the lifetimes evaluated by using eq 2 for the free electron gas model for $E - E_F = 0.5, 1.0$, and 2.0 eV and are compared with the relaxation times deduced from TR-2PPE measurements. As follows from the table, in general, the *ab initio* momentum averaged lifetimes do not follow a precise inverse quadratic scaling with an excitation energy. However, in some cases, the lifetimes can be well fitted by this scaling function using the effective r_s parameter that is different from a "geometrical" definition, $4/3\pi r_s^3 n_0 = \Omega_0$, where n_0 and Ω_0 are respectively the number of valence electrons and the volume per atom. This is the case of noble metals.²²⁶ In Mg and Al, quite accurate scaling is achieved for r_s values obtained from the "geometrical" definition. For transition and rare earth metals, the notion of r_s is not well defined at all. Nevertheless, even for these metals, sometimes it is possible to find

an effective r_s value to approximate the measured or/and calculated lifetime dependence on energy by the inverse quadratic scaling.^{237,250}

By comparing the QF lifetimes with the GW ones for simple and noble metals, one can note that good agreement between these data is obtained only for Mg and Al at energies of 1 and 2 eV. For Be, the disagreement can be attributed to the complicated band structure (Figure 5) that leads to a very strong momentum dependence of the electron and hole lifetimes.^{219,223} For noble metals, the disagreement can be attributed to the absence of d-electrons in the free electron gas model.

As follows from the table, the measured relaxation times are generally shorter than the GW (GW+T) lifetimes, τ_{e-e} . This can be attributed to several factors. First, the experimental relaxation times contain the contribution from the e-ph interaction: the inclusion in theory of this interaction reduces the lifetime. Second, the transport effect results in the reduction of the measured relaxation time.^{251,252} Third, the refilling of the excited state with the cascade electrons from higher excited states increases the relaxation time. For a one-to-one comparison of theoretical lifetimes and measured relaxation times, it is necessary to include in the evaluations all the three above-mentioned factors. In principle, the e-ph contribution to the inverse lifetime can be obtained from first-principles calculations, as was recently done for bulk Be²²³ and Pd.²⁴⁶ However, accurate evaluation of the two other factors is more problematic since it requires the use of nonequilibrium theories.

4. Excitations on Clean Metal Surfaces

As mentioned in the Introduction, an analysis of theoretical and experimental research on electron and hole excitations in surface and image-potential states on clean metal surfaces has been presented in a review by Echenique *et al.*⁷⁴ Here we incorporate an analysis of new experimental and theoretical findings to give a comprehensive perspective and updated idea of all the work done for clean surfaces.

4.1. Excitations in Surface States

One of the conclusions of Echenique *et al.*⁷⁴ was that for surface states on Al and Mg surfaces there was no agreement between the results of the GW calculations^{26,74,253,254} and the photoemission measurement data of the 1980s.^{255–258} In recent photoemission measurements of the temperature dependence of a hole line width in a surface state on Mg(0001), a much better agreement with theory was found.²⁰³ It was also shown that the e-ph coupling in the surface state, $\lambda \approx 0.27$, is close to that, $\lambda \approx 0.30$, in bulk Mg. This result does not seem surprising, since the Mg(0001) $\bar{\Gamma}$ surface state is located in a narrow energy gap and, hence, it is of very bulklike character.^{259,260} Another photoemission measurement has been performed for hole surface states on Bi(110).³⁷ In contrast to earlier measurements of the e-ph coupling in hole surface states on Bi(100),¹⁸⁹ it was found that on Bi(110) the e-ph coupling is quite weak and the coupling parameter λ is similar to that on the Mg(0001) surface. Despite this similarity in λ , the hole decay mechanisms on Mg(0001) and on Bi(110) are different. On Mg(0001), the $\bar{\Gamma}$ surface state energy is of ≈ -1.6 eV (Table 3) and, hence, the e-e contribution, $\Gamma_{e-e} = 92$ meV,²⁰³ is mostly responsible for the hole decay (the e-ph contribution, Γ_{e-ph} , is only of ≈ 20 meV²⁰³). On Bi(110), the energies of

Table 2. Momentum Averaged Lifetimes, τ_{e-e} , (fs) Obtained from *Ab Initio* GW Calculations of Real Metals (Calcd) and Lifetimes Evaluated from Eq 2 for the Quinn–Ferrell (QF) Free Electron Gas Model⁶⁸ Together with the TR-2PPE Measured Relaxation Times (Exp) for Excited Electrons at Energies $E - E_F = 0.5, 1.0, 2.0$, and 3.0 eV^a

metal		τ_{e-e} (fs)			
		0.5 eV	1.0 eV	2.0 eV	3.0 eV
Be ($r_s = 1.87$)	calcd	~200 [219]	85 [219]	40 [219]	10 [219]
	QF	220	55	14	6
	exp				
Mg ($r_s = 2.66$)	calcd	66 [219]	19 [219]	6 [219]	3 [219]
	QF	91	23	6	3
	exp				
Al ($r_s = 2.07$)	calcd	105 [219]	37 [219]; 66 [221]; 56 [82]	10 [219]; 20 [221]; 16 [82]	4 [219]; 9 [221]; 7 [82]
	QF	171	43	11	5
	exp	33 [251]	22 [251]	13 [251]	
Cu ($r_s = 2.67$)	calcd		62 [219]; 40 [226]; 45–50 [221]	14 [219, 226]; 15 [221]	6 [219]; 7 [221, 226]
	QF	90	23	6	3
	exp	~90 [231]	44–65 [231]	16–32 [231]; 17–27 [241]	5–28 [241]
Ag ($r_s = 3.01$)	calcd		44 [226]	16 [226]	6 [226]
	QF	67	17	4	2
	exp				
Au ($r_s = 3.01$)	calcd		58 [226]; 48–63 [221,242]	23 [227]; 17–20 [221]; 18 [226]	13 [227]; 9 [221]; 12 [226]
	QF	67	17	4	2
	exp	200 [243]	87 [243]	26 [243]	9 [243]
Fe \uparrow	calcd	60 [81]	18 [81]	5 [81]	
	exp	8.5 [100]			
Fe \downarrow	calcd	4.5 [81]	4.5 [81]	1 [81]	
	exp	≈ 5 [100]			
Ni \uparrow	calcd	68 [81]	20 [81]	8 [81]	
	exp	18 [100]	7 [100]		
Ni \downarrow	calcd	6 [81]	4 [81]	2.5 [81]	
	exp	13 [100]	5 [100]		
Nb	calcd	30 [237]	13 [237]	8 [237]	4 [237]
	exp				
Mo	calcd	166 [244]; 150 [244]	39 [244]; 30 [244]	10 [244]; 7 [244]	3 [244]; 2 [244]
	exp	50–77 [244]	20 [244]	5–8 [244]	1–4 [244]
Rh	calcd	20 [244]; 17 [244]	7 [244]; 5 [244]	3 [244]; 2 [244]	2 [244]; 2 [244]
	exp	10–14 [244]	3–4 [244]	3–4 [244]	2–7 [244]
Pd	calcd	12 [82]; 9 [82]	9 [82]; 8 [82]; 10–13 [221]	6 [82]; 5 [82]; 6–10 [221]	3–4 [82]; 3 [82]; 4 [221]
	exp				
Ta	calcd	33 [245]	10 [245]; 18 [245]	6 [245]; 9 [245]	5 [245]; 8 [245]
	exp		14 [245]	5 [245]	3 [245]
Yb	exp	78 [250]	137 [250]		

^a For ferromagnetic Fe and Ni, the data are given for both spin-majority and spin-minority states. The lifetimes for Yb have been measured by using STS.²⁵⁰

the hole pockets near the $\bar{\Gamma}$ and \bar{M} symmetry points are small (they are of the order of the $\bar{\Gamma}$ hole surface state on Ag(111), $\approx -(50\text{--}60)$ meV³⁷). Hence, as in the case of Ag(111),³² the Γ_{e-e} is expected to be small too and the dynamics of holes in surface states on Bi(110) is expected to be dominated by the e–ph interaction.³⁷ A similar mechanism of the hole decay in surface states is also expected for Bi(111), where the e–ph coupling was found to be even stronger, $\lambda \approx 0.40$,²⁶⁷ than that on Bi(110).

Recently, Bauer *et al.*^{27,268} measured the energy and line width of the $\bar{\Gamma}$ d surface state on the (0001) surface of the lanthanide metals La, Gd, Ho, and Lu by using STS at low temperature, 10 K. This state, being close to E_F , is located in a local band gap around the $\bar{\Gamma}$ point (see, for instance, calculations by Kurth *et al.* for Gd²⁶⁹). Due to interaction of d electrons with partly filled f shells in Gd and Ho, their d surface states are spin-split: an occupied majority-spin surface state just below E_F and an unoccupied minority-spin surface state just above E_F (see Table 3). Bauer *et al.* have found that the minority-spin surface states show an unusually large line width, $\Gamma \approx 130$ meV, that was attributed to a strong e–e interaction in these flat bands²⁷ and to a strong e–ph coupling in the later publication.²⁹ A different interpretation was given by Allen,²³ who showed, by using the simple

“ferromagnetic Kondo lattice” model, that this width can be explained by electron–magnon (e–m) interaction.

Summarizing the results shown in Table 3, it can be noted that a modern state of the theory that includes both the e–e and e–ph interaction gives electron and hole line widths of the surface state on simple and noble metal surfaces in good agreement with recent measurements by PES and STS. In the case of the Pd(111) surface, a better agreement with TR-2PPE measurements²⁷⁰ can be achieved by the inclusion of the e–ph contribution to the line width. For the rare-earth metals, it seems necessary to perform a detailed theoretical study of all the e–e, e–ph, and e–m interactions to discriminate a dominating mechanism of excited electron (hole) decay in the $\bar{\Gamma}$ d surface state.

4.2. Excitations in Image-Potential States

New contributions shedding light on new aspects of the decay mechanisms of excited electrons in image-potential states have recently been published.^{56,271,279,280} Borisov *et al.*²⁷¹ analyzed the role of resonant one-electron transfer in the decay of the population of resonance image potential states. These states have been found experimentally and/or theoretically, for instance, on the noble metal surfaces Cu(111), Ag(111), and Au(111)^{21,157,281} as well as on

Table 3. Energies (in eV) and Line Widths (in meV) for Different Surface States at Low Temperatures^a

surface state		energy	Γ_{e-e}	Γ_{e-ph}	Γ_{calcd}	Γ_{exp}
Be(0001)	$\bar{\Gamma}$	-2.73	265	80	345 [201]	350 [201]
	\bar{M}_1	-1.8	72	80	152 [201]	(380) [261]
Be(10 $\bar{1}0$)	\bar{A}	-0.42	53	80	133 [202]	130 [202]
		-0.39				185 [188]
Mg(0001)	$\bar{\Gamma}$	-1.6	83 [253], 92 [254], 91 [203]	25 [253], 19 [262]	108 [253], 110	(~500) [258], 133 [203]
		-1.7				(~200) [255]
	\bar{M}	-0.96	32 [254]	9 [262]	41	
	$\bar{\Gamma}$	-2.75	67 [265], 131	18	149 [26]	(500) [256], (450) [257]
Al(100)	$\bar{\Gamma}$	-4.56	336	36	372 [253]	(~1500) [257]
Cu(111)	$\bar{\Gamma}$	-0.445	14	8	22 [32]	24 [32]
		-0.435				23 \pm 1 [266]
Cu(110)	\bar{Y}	-0.510	8 [265]			\leq 32 [264]
Ag(111)	$\bar{\Gamma}$	-0.067	2	4	6 [32]	6 [32], 5 [263]
		-0.063				6 \pm 0.5 [266]
Au(111)	$\bar{\Gamma}$	-0.505	14	4	18 [32]	18 [32]
		-0.484				21 \pm 1 [266]
Pd(111)	$\bar{\Gamma}$	+1.35	37 [270]			(54) [270]
La(0001)	$\bar{\Gamma}$	+0.130				49 \pm 10 [268]
Gd(0001)	$\bar{\Gamma}$	-0.182 \uparrow				44 [27]
		+0.491 \downarrow				132 [27]
Ho(0001)	$\bar{\Gamma}$	-0.09 \uparrow				19 [27]
		+0.347 \downarrow				125 [27]
Lu(0001)	$\bar{\Gamma}$	-0.017				2 \pm 1 [268]

^a The calculated values (Γ_{calcd}) are decomposed in electron–electron (Γ_{e-e}) and electron–phonon (Γ_{e-ph}) contributions. Γ_{e-ph} values for Cu, Ag, Au(111), and Al(100) surfaces are from microscopic computations^{24,26} while for the Mg(0001) surface Γ_{e-ph} is from *ab initio* calculations²⁶² and other values are from 3D Debye model evaluations for $T = 0$ K. Values for Γ_{exp} in parentheses were measured at room temperature.

Table 4. Widths of the Image-State Resonances (in meV)^a

n	Ag(111) $E_u = -0.66$ eV		Cu(111) $E_u = -0.69$ eV		Au(111) $E_u = -1.95$ eV		Be(0001) $E_u = -3.95$ eV
	calcd	exp	calcd	exp	calcd	exp	calcd
1	(33 [75])	(22 \pm 10/6 [289, 290])	(29 [75])	(30 \pm 10 [44])	410 405 [123]	160 \pm 40 [21] 230 [292]	900
2	38.1	\geq 33 [289]	40.6	47 \pm 10 [51] 37.6 [291]	62.8	61 [123]	108
3	12.7	10 [289]	13.4	16.5 \pm 2.5 [51]	19.5		36
4	5.4		5.6		8.2		12.3

^a The first column for each surface corresponds to the present results. Numbers in parentheses correspond to the conventional image states stationary within the one-electron picture. E_u stands for the energy of the top of the projected band gap with respect to the vacuum level. calcd = calculated; exp = experimental.

the simple metal surfaces Be(0001),¹⁵⁷ Be(10 $\bar{1}0$),²⁸² MgB₂(0001),²⁸³ Al(100), and Al(111).^{284,285} Borisov *et al.*²⁷¹ studied Cu(111), Ag(111), Au(111), and Be(0001) by using the wave propagation method (see subsection 2.2.1). They showed that, in contrast to image-potential states located in the projected gap (this is the case for Cu(100)²⁸⁶ and Ag(100)⁷⁴) on Cu(111) and Ag(111), the line width of the second ($n = 2$) image state is wider than that of the first ($n = 1$) image state. We summarize the calculated results for the first four image-potential states in Table 4. This unusual result can be easily explained by the different nature of the $n = 1$ and $n = 2$ states. The $n = 1$ state lies in the gap while the $n = 2$ state is degenerate in energy with bulk states (see Figure 2). Then the line width of the $n = 1$ state is determined by many-body inelastic scattering processes while the decay of the $n = 2$ state is determined by more efficient one-electron charge transfer. On other surfaces, where all image states are resonances, they show a regular behavior: the line width decreases with the increase of the quantum number n . Moreover, the line width of resonance image states on all the surfaces studied obeys the n^3 scaling established theoretically^{19,20,287} for the gap image states and confirmed experimentally in TR-2PPE measurements.⁴⁶ This result can be understood from the quasi-classical arguments. Indeed, for the electron moving under the action of the image

potential and colliding from time to time with the surface, the rate of the electron escape into the metal is given by the fixed probability of the transmission through the metal–vacuum interface multiplied by the collision frequency. Since the difference in energies of the image state resonances is relatively small, the transmission probability is basically constant through the n -series, while the collision frequency is proportional to n^{-3} .²⁸⁸ Thus, the resulting resonance charge-transfer rate (width) has an n^{-3} dependence. Another important point of the calculation²⁷¹ is that the calculated line widths are in good agreement with available experimental data (see Table 4). This confirms that the decay of excited electrons in resonance image states is mostly due to one-electron transfer from the image state to underlying bulk and surface states.

On surfaces of ferromagnetic materials, the gap image-potential states are expected to be spin-split due to the spin-split character of the bulk band structure projection. For these states, the exchange splitting between majority- and minority-spin states is comparable with the total line width^{21,42} that includes lifetime broadening and quasielastic scattering. This makes difficult measuring the intrinsic line width (lifetime broadening) of individual image states. However, recently, time-, energy-, and spin-resolved 2PPE measurements of a thin Fe film on Cu(100) by Schmidt *et al.*²⁷⁹ have overcome

Table 5. Lifetimes (in fs) Measured by TR-2PPE and Calculated Using the GW Approximation for Image-Potential States on Clean Metal Surfaces: calcd = calculated; exp – experimental

metal	ref	lifetime				
		$n = 1$	$n = 2$	$n = 3$	$n = 4$	$n = 5$
Li(110)	calcd [277]	18	44			
Cu(001)	exp [46, 295]	40 ± 6	120 ± 15	300 ± 20	630	1200
	exp [297]	41.3	150	406		
	calcd [286]	38	168	480		
Cu(119)	exp [274]	15 ± 5	39 ± 5	105 ± 15	200 ± 20	350 ± 40
Cu(117)	exp [274]	15 ± 5	39 ± 5	95 ± 15	190 ± 20	350 ± 40
Cu(111)	exp [44, 51]	18 ± 5	14 ± 3	40 ± 6		
	calcd [75]	23				
Cu(775)	exp [394]	18 ± 2				
Ag(001)	exp [295]	55 ± 5	160 ± 10	360 ± 15		
	calcd [30]	55	219	658		
Ag(111)	exp [275]	32 ± 10	≤ 20			
	calcd [75]	20				
Au(100)	calcd [278]	22		264		
Fe(110)	exp [279]	$16 \pm 2 \uparrow, 11 \pm 2 \downarrow$	93			
	calcd [278]	31				
	calcd [278]	37				
Ni(100)	exp [298]	16 ± 5				
	calcd [278]	20	101	287		
Ni(111)	exp [272]	7 ± 3				
	calcd [278]	15				
Ru(0001)	exp [495]	11				
	calcd [276]	14				
	calcd [278]	14	70			
Pd(100)	calcd [278]	11	56			
Pd(111)	exp [270]	25 ± 4				
	calcd [270]	22	89			
	exp [273]	26 ± 7	62 ± 7			
Pt(111)	calcd [273]	29	73			

this problem and found spin-dependent lifetimes for $n = 1$ and $n = 2$ (see Table 5). They obtained $\tau_1 = 16 \pm 2$ fs and $\tau_1 = 11 \pm 2$ fs for the majority- and minority-spin electrons, respectively, in the $n = 1$ state. The corresponding intrinsic line widths $\Gamma_1 = 41$ meV and $\Gamma_1 = 60$ meV compare well with the found exchange splitting of 56 ± 10 meV for this state. For the $n = 2$ state, the values $\tau_2 = 47 \pm 3$ fs ($\Gamma_1 = 14$ meV) and $\tau_1 = 35 \pm 3$ fs ($\Gamma_1 = 19$ meV) were obtained for the majority- and minority-spin electrons, respectively. In this case, the intrinsic line widths are much bigger than the respective exchange splitting, 7 ± 3 meV. Schmidt *et al.*²⁷⁹ also showed that quasielastic scattering processes are spin-dependent.

Application of an external electric field to a metal surface induces a Stark shift of intrinsic surface states²⁹³ as well as of image-potential states.⁵⁶ This effect has been identified in STM and STS measurements of binding energies of surface and image states by comparing these energies with photoemission results.^{21,38,42,56,74,266,293} An electric field between the probe tip of a scanning tunneling microscope and the surface of the sample induces a Stark shift of image-potential states by ~ 5 eV, so it is important to know how much this field affects the dynamics of excited electrons. Many-body calculations of the lifetime of electrons in image states on Cu(100) with an applied electric field have recently been done by Crampin.²⁸⁰ He showed that an increase of bias voltage leads to an increase of the intrinsic line width of an image state. Two mechanisms are responsible for this increase. First, the applied field pushes an image state closer to the surface, producing larger overlap of this state with underlying bulk and surface states. This in turn increases the imaginary part of the self-energy and, respectively, the line width. Second, the applied field pushes up the energy level of the image state, opening more final states (more

decay channels) for the excited electron decay. This also increases the imaginary part of the self-energy and the line width. The Crampin analysis showed that the tip-induced change in the electron lifetime has to be taken into account in the STM studies of the dynamic properties of surface electronic states, especially high-energy states.

As mentioned in section 3, in many metals, plasmon excitations have energies of 10–20 eV. Therefore, these excitations are beyond the relevant energy interval 0–4 eV for the decay of image-potential-state electrons. In Ag, however, both the surface and bulk plasmons have energies around 3.8 eV. These collective excitations can influence the decay of image-potential states via the participation of d-electrons in the screening of electron–electron interaction.^{28,30} The effect of d-electrons on the screening can be taken into account by using the s–d polarization model of Liebsch^{205,294} that replaces the d states by a polarizable medium characterized by the local dielectric function $\epsilon_d(\omega)$. It had been expected that the inclusion of the d band effect and therefore of the surface-plasmon excitation as a new channel for the decay of image-potential states would reduce their lifetimes. García-Lekue *et al.*,²⁸ however, showed that the subtle combination of the spatial variation of s–d polarization and the characteristic nonlocality of the electron–electron interaction near the surface actually yields longer lifetimes for the $n = 1$ state on Ag(100) which are in excellent agreement with time-resolved 2PPE measurements.²⁹⁵ The presence of collective excitations thus explains why the lifetimes of the image-potential states on Ag(100) are longer than those on Cu(100) (see Table 5).

In Table 5 we show the measured TR-2PPE lifetimes of excited electrons in image-potential states on noble and transition metals surfaces. For comparison, we also give the theoretical lifetimes obtained from the GW calculations with

the one-dimensional potentials of refs 157 and 197. Note that the theoretical lifetimes are represented in Table 5 only by the e–e contribution since the e–ph contribution to the decay rate of electrons in image states is normally small ($\Gamma_{\text{e-ph}} \lesssim 1$ meV for the first image state and significantly smaller for the higher image states) and, thus, can be ignored for image states.²⁹⁶ As follows from the table, a good agreement between the TR-2PPE and theoretical lifetimes is obtained for the first ($n = 1$) image state on all the metal surfaces except for surfaces of ferromagnetic metals, Fe and Ni (for Co(0001) there is no available experimental data). For the latter surfaces, the calculated lifetimes are higher by a factor of 2 compared to the measured data. This can be attributed to the model used for calculations of the electronic structure of these materials. The band structure obtained with a one-dimensional model potential^{157,197} does not contain d-electron bands, which means a smaller number of electrons per atom compared to that in the real metal. This leads to weaker screening and, consequently, to higher lifetimes. It is believed that *ab initio* calculations which take d-electrons and the spin-dependence of all electrons into account can give lifetimes of electrons in image states in much better agreement with the TR-2PPE data. For the higher image states, the agreement between the theory and experiments is less impressive than that for the $n = 1$ image state. The origin of this disagreement is not yet clear.

4.3. Collective Excitations on Clean Metal Surfaces

In the jellium-like models, the surface-response function predicts a zero width for surface plasmons in the long-wavelength limit. The theory predicts that, with increasing of momentum q_{\parallel} parallel to the surface, the width rapidly increases due to decay into electron–hole pairs. This would lead to the situation that collective excitations with small momenta could not affect electronic excitations with energies less than the surface plasmon energy. However, experimentally, the surface plasmons exhibit a finite width even at $q_{\parallel} = 0$. On typical metal surfaces such as Al, Hg, and Mg, the surface plasmon width is of the order of 1 eV.^{299,300,303,305} Since surface plasmon properties in the $q_{\parallel} = 0$ limit are determined by the bulk dielectric function $\epsilon(\omega)$, the experimental surface-plasmon widths $\Delta\omega_{\text{sp}}$ at $q_{\parallel} = 0$ should be approximately described by the measured bulk dielectric function $\epsilon(\omega)$. Indeed, in the case of Ag, Li, Hg, and Mg, the experimentally observed surface-plasmon width is well described in this manner.²⁰⁵ Nevertheless, for K and Al the width was found to be considerably larger than that predicted in this way. The results of the first calculations of the surface plasmon width with the full inclusion of three-dimensional electronic structure for the Mg(0001) and Al(111) surfaces have been presented recently in refs 210 and 211, respectively. The calculations show that both a realistic electronic structure calculated within an *ab initio* approach and a proper treatment of exchange–correlations are crucial for the description of the surface plasmon width for the entire momentum region. A very good agreement has been obtained with experimental data, as is appreciated in Figure 16 for the Mg(0001) surface. Based on this agreement, it was concluded that other possible sources such as defects, steps, and phonons do not influence the surface plasmon decay. It was also demonstrated that the inclusion in the theory of band structure effects only in the direction perpendicular to the surface is not sufficient to describe the surface plasmon

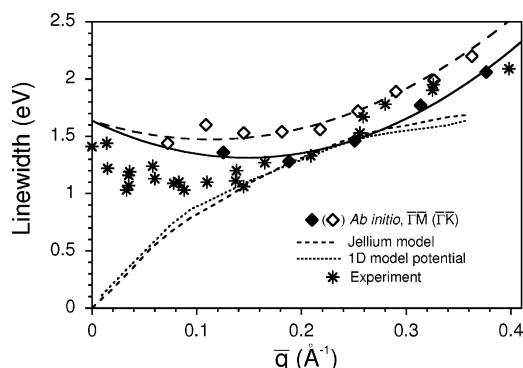


Figure 16. (a) Surface plasmon width dispersion for Mg(0001) calculated with the momentum-dependent kernel of ref 306. *Ab initio* data for the $\overline{\Gamma M}$ ($\overline{\Gamma K}$) direction of the surface Brillouin zone are shown by the filled (open) diamonds. The solid (long dashed) line is the corresponding best data fit. The dashed (dotted) line presents the jellium model (one-dimensional model potential¹⁵⁷) dispersion. Stars indicate experimental data.³⁰³

width in the small momenta region. Additionally, for both Mg(0001) and Al(111), the calculations gave an initial negative dispersion of the surface plasmon width, a behavior that was also observed experimentally for a variety of metal surfaces such as Ag(110),^{301,302} Mg(0001),³⁰³ mercury,³⁰⁰ graphite,³⁰⁴ and Al(111).³⁰⁵

The energies of strongly localized sp surface states at the (111) noble metal surfaces have quasi-parabolic dispersion with momentum parallel to the surface. Hence, these states can be considered to form a quasi 2D electron gas with a 2D Fermi energy equal to the surface-state binding energy at the center of the surface Brillouin zone. In the absence of the 3D bulk electrons, this 2D electron gas would support a 2D collective oscillation with the dependence of its energy on the 2D momentum q_{\parallel} given by the equation³⁰⁷

$$\omega_{2D} = (2\epsilon_F^{2D} q_{\parallel})^{1/2} \quad (84)$$

This equation shows that, with increasing wavelength, plasmon frequencies in a 2D electron gas go to zero and, therefore, should contribute to the decay of all electronic excitations. However, due to their square-root dependence on the wave vector, these plasmons do not affect electron–hole and phonon dynamics significantly near the Fermi level.

Recently, it has been demonstrated that due to the presence of the 3D bulk electrons the dynamical screening at surfaces provides a mechanism for the existence of a new collective mode, the energy of which has a linear dependence on the 2D momentum in the small q_{\parallel} region. It has been shown that metal surfaces where a partially occupied quasi-2D surface-state band coexists in the same region of space with an underlying 3D electron continuum support a well-defined acoustic-like surface plasmon.^{213,308} In this case, a combination of the nonlocality of the 3D dynamical screening and the spilling out of the 3D electron density into the vacuum allows the formation of the 2D electron-density acoustic-like oscillations at metal surfaces.^{309,310} To date, the acoustic surface plasmon properties, such as energy and line width dispersions, have been calculated for Be(0001) and (111) noble metal surfaces with the use of the surface model potentials of refs 157 and 197. Recent calculations have demonstrated that this collective mode should be well defined in the energy range from zero up to, at least, several hundred millielectronvolts.²¹³ In Figure 17 the results reported in ref 213 for the Cu(111) surface acoustic plasmon line width are

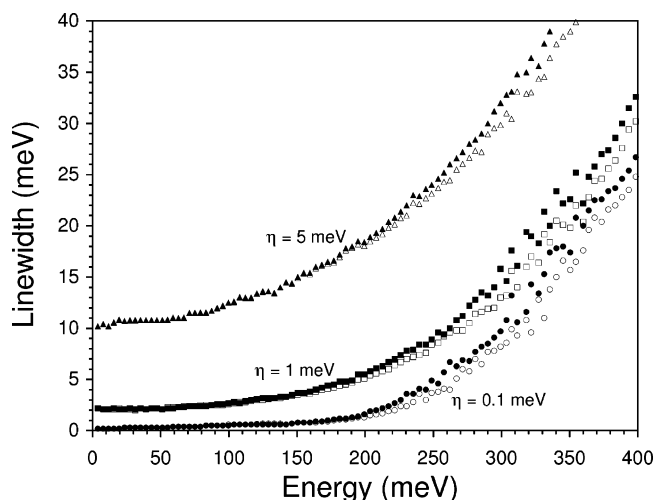


Figure 17. Line width of the acoustic surface plasmon in the Cu(111) surface versus plasmon energy, as obtained from the imaginary part of the surface-response function $g(q_{||}, \omega)$ of eq 82 for three values of the broadening parameter $\eta = 0.1, 1$, and 5 meV entering eq 80.²¹³ Solid (open) symbols represent the line width with (without) inclusion of transitions between 2D and 3D states in the evaluations of the noninteracting density-response function of eq 80.

presented. Acoustic surface plasmon decay can occur by exciting electron–hole pairs either through transitions between 2D and 3D states or through transitions within the 3D continuum of bulk states. At small energies below $\omega \sim 110$ meV, where an acoustic surface plasmon can only decay by exciting electron–hole pairs within the 3D subsystem, one can see that its line width is entirely determined by the external broadening parameter η . With an increase of plasmon energy above ~ 110 meV, the 3D intraband contribution to the line width significantly increases. On the other hand, by comparing the results with (solid symbols) and without (open symbols) inclusion of transitions between 2D and 3D electronic states in the evaluation of the $\chi(z, z', q_{||}, \omega)$, one can draw a conclusion about their low level of importance in the acoustic plasmon decay in the entire energy range considered. Whereas, due to its small energy, this acoustic surface plasmon should influence the decay rate of all electronic excitations at the metal surfaces, its relative impact is not clear at the moment. To clarify this point, additional investigations are required.

5. Overlayers on Metal Surfaces

5.1. Metal Overlayers on Metal Surfaces

The growth of ultrathin metal films with thicknesses ranging from a fraction of a saturated atomic monolayer to several monolayers on a metal substrate can produce a variety of effects in the electronic structure. *First*, the adfilm can remove or modify the intrinsic surface state of the substrate. This is the case for sodium adlayers on Cu(111)^{311–318} and on Al(100).^{319–321} *Second*, if the substrate has a local band gap or symmetry band gap in the direction normal to the surface, it is possible for electrons to be trapped in quantum well (QW) states. These states form 2D electron gases with metal densities localized in the adfilm. Systems with local band gaps are, for instance, Fe on Au(100),³²² Ag on Au and Au on Ag,^{323–327} and Pb on Cu(111).^{328,329} Typical systems with the symmetry band gaps are adfilms of Ag on Fe(100)³²⁴ and on V(100).^{330,331} *Third*, adfilms with reason-

ably large thickness can support surface states (states localized at the adfilm–vacuum interface). These surface states are easily formed by noble metal adfilms on noble metal substrates.^{324–327,332–335} *Fourth*, adfilms with a sharp adfilm–substrate interface can support clear interface states which can be detected in photoemission measurements. An example of such systems is Mg adfilms grown on W(110). In recent photoemission measurements,^{336,337} a clear Mg interface state was found for a number of thicknesses of Mg adfilms. Moreover, it was shown that this state is spin-split due to W substrate-induced spin–orbit interaction. *Fifth*, in many cases, the growth of ultrathin films causes the change of two-dimensional translational symmetry,^{338,339} resulting in the folding of the substrate electron bands. The folded substrate bands partly cover the substrate energy gap, thus changing the character of the quantum-well state from the QW gap state to QW resonance. This change can affect the decay mechanisms of the excited electrons (holes) in QW states.⁸⁵

Of the two contributions to the lifetime broadening of QW states (electron–electron, Γ_{e-e} , and electron–phonon, Γ_{e-ph}), the latter has been investigated in detail for Ag/Fe(100),^{191,340} Ag/V(100),^{204,331} and Na/Cu(111).^{312,318,341} These investigations have been motivated by several reasons: (1) to explain the measured hole quantum-well states line width, it is important to measure both Γ_{e-e} and Γ_{e-ph} contributions; (2) in ultrathin films, the e–ph coupling parameter λ can be very different from λ in the corresponding bulk metals,^{324,331} which is important for the search for new superconducting materials; (3) the λ parameter can strongly vary with the variation of the adfilm thickness;³³¹ (4) λ can be directly extracted from the temperature dependence of the hole QWS line widths obtained from photoemission measurements. For QW states with binding energies larger than the Debye frequency of the material of interest, only the e–ph contribution, Γ_{e-ph} , is temperature dependent (see eq 68) and the slope of this dependence gives λ . However, this slope reflects e–ph coupling only if noticeable amounts of thermal defects such as vacancies or/and interstitial atoms do not appear with the increase of temperature. In noble metals and many transition metals, the effect of thermal defects on the $\Gamma_{e-ph}(T)$ can be safely avoided in the temperature interval ≈ 0 –300 K. In this temperature interval, Paggel *et al.*¹⁹¹ measured λ in the sp and d hole states for a 10-layer film of Ag on Fe(100). They found that e–ph coupling is much stronger in the sp hole state ($\lambda \approx 0.5$) than that in the two d hole states ($\lambda \approx 0.05$) of the adfilm. These results can be compared with those of e–ph coupling in bulk Pd. This metal is a neighbor of Ag in the periodic table and shows a similar structure in the density of electron states. The main difference between the two DOSs is that in Pd the DOS is shifted up toward E_F by ≈ 4 eV and the peak related to the top of the 4d states is located at E_F instead of at ≈ -4 eV as in bulk Ag. In recent first-principle calculations of the e–ph interaction in Pd, Sklyadneva *et al.*²⁴⁶ showed that the e–ph coupling parameter λ at the top 4d state, X_5 , at the X point is equal to 0.05 and in the Δ_1 sp band $\lambda \approx 1.0$ and $\lambda \approx 0.35$ at E_F and at the X point, respectively. However, only a few Pd d-electron states show a very small value of λ ; the majority of d states exhibit λ values which are comparable with λ in the sp states and in many cases are much larger than λ in the sp states.

Kralj *et al.*²⁰⁴ studied the layer dependence of λ in the sp-QW state of Ag adfilms on V(100). They showed that λ

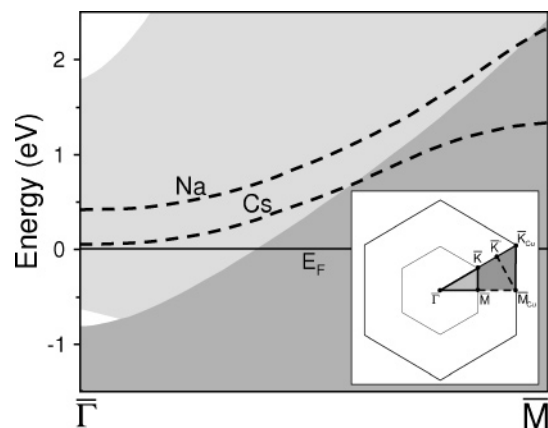


Figure 18. Dispersion of $p(2\times 2)$ Na and Cs quantum well states in the $\bar{\Gamma} - \bar{M}$ direction.⁸⁵ The dark gray area indicates the projection of bulk Cu states onto the (1×1) SBZ, while the light gray area shows the closing of the gap around $\bar{\Gamma}$ after back-folding from the $\bar{M} - \bar{M}_{\text{Cu}}$ and $\bar{M}_{\text{Cu}} - \bar{K}'$ symmetry directions defined in the inset.

strongly varies with the number of adlayers at thicknesses of 1–4 Ag monolayers and that for thicker films it approaches the Ag bulk value. This variation was interpreted in terms of the interaction of the photohole with the potential step oscillations induced by the Ag surface atom vibrations at the Ag–vacuum interface.²⁰⁴

More theoretical work has been done to evaluate the e–ph interaction in Na ultrathin films on Cu(111). In the pioneering work of Hellsing and coauthors,³¹² the e–ph coupling constant was calculated for the QW state in 1 monolayer (ML) of Na/Cu(111) by assuming that vibrations of a Na monolayer can be represented by a single phonon mode with Na atom vibrations in the direction perpendicular to the monolayer plane (Einstein mode). This model accounted for the whole QW state width, that in general includes contributions from inelastic e–e scattering as well as from one-electron processes and from scattering on defects. Later it was shown that the inelastic e–e scattering contribution is not negligibly small and should be included in the description of the QW state dynamics in 1 ML of Na/Cu(111).³¹⁸ Very recently, Borisova *et al.*³⁴² have shown that in 1 ML of Na/Cu(111) clear Na perpendicular modes do not exist. All perpendicular vibrations with Na atoms involved have the largest weight in the Cu(111) substrate. Hence, the contribution to λ in the QW state should be formed by many modes. This was assumed in the estimations of the e–ph contribution by Chulkov *et al.*³¹⁸ where the phonon-induced contribution, $\Gamma_{\text{e-ph}}$, was shown to be comparable with the e–e inelastic contribution, $\Gamma_{\text{e-e}}$. The perpendicular Na vibrational mode was shown to arise for Na coverages $\theta < 1$ ML. It becomes stronger as coverage is further reduced. This fact makes the role of the Einstein mode much more important for coverages lower than 1 ML of Na.

The role of another decay mechanism of electrons excited in a QW state, namely elastic one-electron scattering, was recently studied by Corriol *et al.*⁸⁵ using $p(2\times 2)$ overlayers of Cs and Na on Cu(111) as an example. The growth of these overlayers creates a surface unit cell which is larger than the Cu(111) substrate unit cell; thus, it decreases the reciprocal unit cell and leads to folding of the substrate electron bands. This folding makes the Na and Cs QW states degenerate with the Cu bulk bands, as shown in Figure 18, and introduces a new mechanism for the decay of electron states which are not present in the case of the gap QW states.

Table 6. Line Width Contributions (in meV) of Various Scattering Channels for the $p(2\times 2)$ Na and Cs Overlayer Quantum Well States^a

	energy	Γ_{elastic}	$\Gamma_{\text{e-e}}$	$\Gamma_{\text{e-ph}}$	Γ_{total}	Γ_{exp}
Cs	42	9.4 ± 3	< 0.1	7.5 ± 3	17 ± 3	18 ± 2
Na	408	7.4 ± 3	0.4	9 ± 3	16.8 ± 3	16 ± 3

^a The energy (in meV) of these states is given with respect to E_F . Γ_{elastic} represents elastic scattering, $\Gamma_{\text{e-e}}$ represents electron–electron scattering, and $\Gamma_{\text{e-ph}}$ represents electron–phonon scattering. Γ_{total} is the resulting total width. Γ_{exp} are the STS experimental values.⁸⁵

It was found (see Table 6) that the many-body inelastic e–e scattering contribution to the QW state line width is small while the one-electron (elastic) scattering contribution gives half of the experimentally observed line width. The rest is given by e–ph scattering.

5.2. Insulating Overlayers on Metal Surfaces

Overlayers other than metallic ones are also possible and indeed influence the dynamics of excited electronic states at surfaces. Depending on their interactions with the excited electrons, they can lead to various phenomena. As examples, we can mention the localization processes, such as formation of small polarons⁴ or electron solvation.^{343,467} The case of molecular overlayers on surfaces has recently been reviewed by Zhu.³⁴⁴ Below, we will concentrate on the case of a thin layer of an insulator covering a metal surface. Detailed experimental and theoretical studies have demonstrated that the dynamics of excited states at surfaces is deeply modified in the presence of a thin layer of an insulating material. In many cases, the layer acts as a spacer layer; that is, it produces an overall repulsive potential for electrons which prevents a low energy electron from penetrating the insulator layer and, thus, efficiently separates the substrate electronic states from the vacuum ones. This is a big difference with regard to metallic overlayers, where the electron–overlayer potential is overall attractive, leading to the appearance of quantum well states located inside the layer.

The first experimental studies on the excited electron dynamics at surfaces in the presence of spacer layers by Harris *et al.*^{345,346,493} addressed the role of different parameters of the system. In particular, the key influence of the relative energy position of the electronic excited state and of the insulator band gap was clearly demonstrated. Harris *et al.* studied the case of image states on a Ag(111) surface covered by a thin Xe overlayer.^{345,346,493} They showed that, if degenerated with the Xe layer band gap, the image state retains its character and it is located in the vacuum outside the rare gas layer. As a consequence, it is located in a region of space where the image charge attraction is weaker and, thus, the binding energy of the image state is smaller than that on the clean metal surface. The penetration of the image state inside the metal substrate is also much decreased compared to the clean metal surface case, and thus, the image state decay rate due to inelastic electron–electron interactions in the substrate is decreased. At this point, it must be stressed that the decay of the image state involving inelastic electron–electron interactions that is dominant on clean metal surfaces cannot occur in an insulator, due to the lack of available final states for the transitions. Thus, the image state decay still has to involve the metal substrate electrons. Another situation is met if the image state energy is outside the insulator band gap, so that the image state electron can easily

penetrate the overlayer. The character of the excited states is then quite different from the previous case. Excited quantum well states localized inside the layer can appear similarly to the case of metal overlayers. As well, states localized both in the layer and in the vacuum can be formed. These states exhibit a mixed image state—quantum well state character. The energy and the width of these states strongly depend on their spatial localization. The presence of an insulator layer can thus, *a priori*, lead to the existence of states with very different characteristics. Detailed TR-2PPE studies have been reported for image states on insulators in a variety of systems consisting of, e.g., rare gas layers on noble metal substrates,^{150,291,345–347,493–495} alkanes on Ag(111),⁴⁹³ oxygen molecules on Cu(111),⁴⁹⁴ nitrogen molecules on Cu(111),³⁴⁸ naphthalene on Cu(111),³⁴⁹ *n*-heptane on Au(111),¹²³ and *p*-xylene on Ag(111).³⁵⁰

Similar to the case of clean metal surfaces,³⁴ inelastic intraband scattering processes have been observed for dielectric layers on metal substrates.^{348,350} TR-2PPE experiments revealed that for small electron momenta parallel to the surface, k_{\parallel} , the time-resolved photoemission signal maximizes for pump–probe time delays larger than that for large k_{\parallel} . This brings evidence for the time evolution of the momentum distribution of excited electrons and, in particular, for transitions from high to low k_{\parallel} states within the same image state continuum. Thus, the movement parallel to the surface of an electron in an image state with a nonzero k_{\parallel} is slowing down due to its interaction with the overlayer. Detailed analysis of the experimental data and, in particular, of the rise and fall time of the photoemission signal as a function of k_{\parallel} leads to the interpretation of this relaxation process as due to energy transfer to the frustrated rotation of the molecules in the layer³⁴⁸ or to friction of the image state electron with energy transfer to the substrate electrons.^{34,350}

On the theoretical side, the effect of an insulator layer on excited electronic states at surfaces was first treated using a continuous dielectric medium (CDM) model.^{345,347} The basic idea of the CDM³⁵¹ is to consider the overlayer as a continuous medium, which can be characterized by the electrostatic properties of the infinite insulator medium, the permittivity ϵ , and the energy position of the conduction band minimum. Then, classical electrostatics is used to compute the potential felt by the image state electron interacting with the metal + overlayer system. Potential discontinuities at interfaces are removed by an ad-hoc procedure. This modeling, associated with some parameter adjustment, reproduces the experimental results in certain systems.^{345,347} In particular, it accounts quite well for the various trends mentioned above. However, this approach fails for certain systems, such as Ar on Cu(100).³⁵² Besides the use of an adjustment procedure, this approach neglects the effect of the overlayer crystallography, as well as the variation of the medium characteristics with the layer thickness. A one-dimensional (1D) model of rare gas layers has been developed that represents the rare gas layer by a potential modulated perpendicular to the surface, following the atomic planes, and invariant by translation parallel to the surface. It allows one to account for the effect of the rare gas layer (ref 353, see details in the article by Gütde *et al.* in this issue).

A three-dimensional parameter-free approach has been recently developed to describe the interaction of a low energy electron with an Ar layer adsorbed on a metal.¹⁵² It is based

on a pseudopotential description of the electron–Ar interaction and incorporates the actual crystallographic structure of the layer. It consists first in determining the pseudopotential, the sum of a short-range part and of a long-range polarization part, that reproduces the scattering phase shifts for a low energy electron interacting with a free Ar atom. Then, knowing the crystallographic structure of the Ar layer, one sums all the interaction potentials between the active electron and the Ar atoms, taking into account the mutual polarization effects. This mutual polarization is the essence of the dielectric character of solid Ar. Indeed, all the Ar atoms are polarized by the active electron and its image in the metal substrate; this creates dipoles on the various Ar atoms that polarize each other. The mutual polarization problem is solved by a self-consistent iterative method.¹⁵² In this way, the external field brought by the active electron is properly screened by the Ar medium. Tests on bulk Ar show that this approach quantitatively reproduces the behavior of low energy electrons in Ar. The total potential felt by the active electron is then obtained as the sum of the electron-layer and electron-substrate potentials, with the latter being the local potential introduced by Chulkov *et al.*¹⁵⁷ to represent the electron interaction with a clean metal surface.

The wave packet propagation approach (see section 2.2.1 for details on the procedure) has been used to determine the characteristics of image states in the Ar/Cu(100) system modeled with the 3D microscopic potential described above. The results of this study account for the available experimental data.^{150,152} Figure 19 presents the electron densities of the $n = 1$ image states for 1 ML and 4 ML of Ar on Cu(100). The calculation is three-dimensional, but the figure only presents a cut of the 3D density in the plane perpendicular to the surface. In bulk Ar, the bottom of the conduction band is located above the vacuum level,^{152,354} so that we expect the image states to be repelled by the Ar layer and to be confined in the vacuum outside the layer. This is fully confirmed by the calculation (Figure 19). As the electron penetrates from the vacuum into the Ar layer, the electron density decreases on the average, consistent with the insulator character of the layer. The electron density further decreases inside the metal substrate because of the projected band gap. As a result, in the 4 ML case, the probability of finding an image state electron inside the metal is extremely small. A very well marked structure appears at the location of the Ar atoms in the layer, and it corresponds to the orthogonality constraint of the image states to the inner levels that are bound in the electron–Ar pseudo potential. When averaged parallel to the surface, the electron density decreases steadily as the electron penetrates the layer and the substrate and only exhibits small modulations following the Ar planes. Comparing parts a and b of the figure, one can see that as the Ar layer thickness increases, the electron is repelled further away in the vacuum, leading to a decrease of its binding energy.

Figure 20 presents a comparison between the computed and measured energies and lifetimes of the $n = 1, 2$, and 3 image states in Ar/Cu(100).¹⁵⁰ The microscopic representation of the Ar layer is seen to lead to an excellent agreement with TR-2PPE experimental data for the state energy. The microscopic approach was also used to get the effective mass of the image states, m_{eff} , for electron motion parallel to the surface. m_{eff} is defined from the dispersion relation $E(\mathbf{k}_{\parallel})$ calculated with the WPP approach. It was found to be slightly smaller than the free electron mass, m_e , with the difference

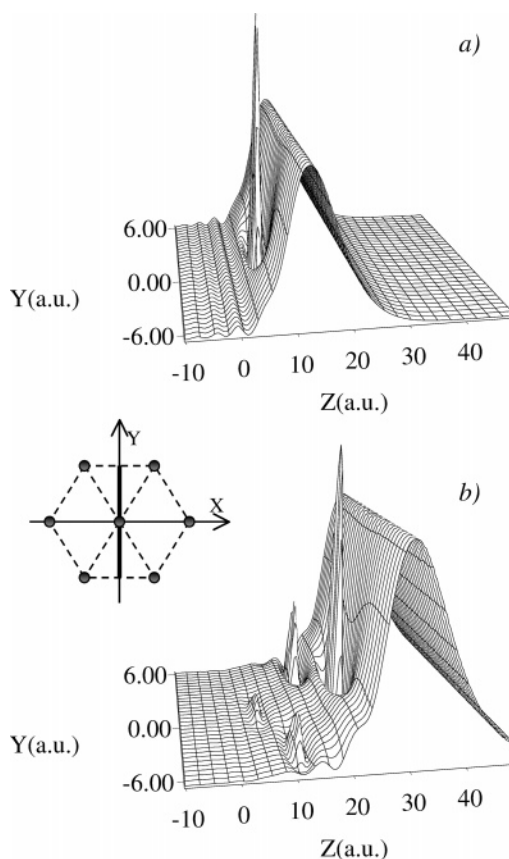


Figure 19. Two-dimensional cut of the 3D electron density corresponding to the ($k_{\parallel} = 0$) $n = 1$ image state on a Cu(100) surface covered by 1 ML (part a) and 4 ML of Ar (part b). The Z-axis is perpendicular to the surface ($Z > 0$ in a vacuum, the Cu image plane is located at $Z = 0$), and the Y-axis is one of the axes parallel to the surface. The position of the Y-axis with respect to the hexagonal array in the outer Ar layer is given in the inset. The thick segment along the Y-axis indicates the range shown in the figure.

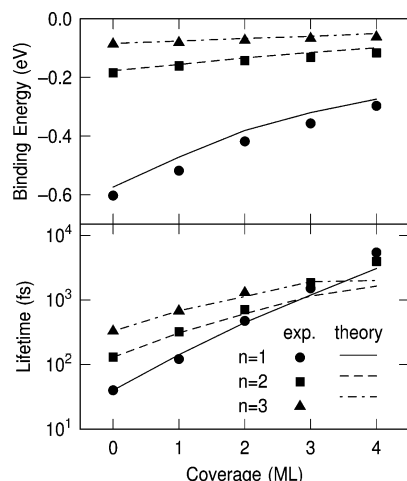


Figure 20. Binding energy (in eV, upper part) and lifetime (in fs, lower part) of the $n = 1, 2$, and 3 image states on Ar/Cu(100) as functions of the Ar coverage expressed in monolayers, ML. Symbols show the experimental results, and lines show the results of the 3D microscopic study.¹⁵⁰

varying according to the penetration of the image state wave function inside the Ar layer. This is consistent with experimental results¹⁵⁰ that reported an image state effective mass equal to m_e within a 10% accuracy. Indeed, the image states

are predominantly located in the vacuum for which a free electron mass is expected, and they slightly penetrate the Ar layer, for which an effective mass of the order of that in bulk Ar ($0.47m_e$ in the 3D microscopic description) is expected. As for the lifetime of the n image state, τ_n , it has been computed using a bulk penetration approximation. The change of lifetime between clean Cu and Ar covered surfaces (Ar/Cu) was obtained as the ratio between the bulk penetrations, p_n , of the image states:

$$\frac{\tau_n(\text{Ar/Cu})}{\tau_n(\text{cleanCu})} = \frac{p_n(\text{cleanCu})}{p_n(\text{Ar/Cu})} \quad (85)$$

This approximation is based on the qualitative idea that, since the image state decay comes from inelastic interactions of the excited electron with bulk electrons, it should be weighted by the wave function penetration into the bulk. Despite the fact that this approximation neglects the nonlocal effects, it gives quite reasonable results in the Ar/Cu case, as has been recently demonstrated with many-body calculations based on the above-mentioned 1D modeling.³⁵⁵ The results of the microscopic description approach for the lifetime are shown in Figure 20 together with TR-2PPE experimental data. Both sets exhibit the expected trend of increasing τ_n when the layer thickness increases. The agreement is quite good, deteriorating progressively with the layer thickness. One can notice that, in both sets, the relative magnitude of the lifetime for the various n states is noticeably changing with n . This has been interpreted as an effect of the different tunneling probabilities of the image states through the Ar layer.¹⁵²

One of the qualitative results of the above study that could look surprising at first sight is noteworthy: an atomically thin Ar layer has a clear insulator character. Indeed, it could be argued that a single monolayer would have shown some porosity. However, it does not. This feature has consequences for several other systems. First, on the (111) surfaces of noble metals, the projected band gap does not overlap the vacuum level. Then, the higher lying image states are, in fact, resonances with quite short lifetimes due to their decay by resonant one-electron transfer into the bulk. In this case too, the presence of an insulator layer that separates vacuum from the bulk substrate results in a significant lengthening of the resonance lifetime.^{123,291} A very extreme case is that of a free-electron metal covered by an Ar layer that has been studied theoretically using the 3D microscopic approach.³⁵⁶ On a free-electron metal, the image potential is present but no band gap can prevent the electron from escaping into the bulk. Only extremely broad resonances, if any (see the discussion in refs 357 and 358), can appear in such a case. It was shown³⁵⁶ that a thin Ar layer adsorbed on a free-electron metal surface leads to the existence of well-defined long-lived image resonances, quite comparable to the usual image states seen on surfaces exhibiting a surface-projected band gap.

The presence of a thin insulator layer also influences the surface state on the (111) surfaces of noble metals. The energy change due to the presence of a thin rare gas layer (up to a few monolayers) could be observed both by STS and photoemission.^{359–362} The surface state band bottom was found to move up by around 50–150 meV, increasing from Ar to Xe. The case of surface states on Au(111) was further studied using the CDM model described above for image states. Though not fully quantitative, this study allowed one

to interpret the surface state energy shift as a result of the change of the image potential outside the surface due to screening by the rare gas layer.³⁶²

Besides the change in the dynamics of the electronic states already present at a clean substrate surface, an insulator layer on a metal can lead to the appearance of new states, located inside the insulator layer. As we have already mentioned, for heavy rare gas layers such as Xe, quantum well states can be formed.^{345,493} Observed in the Xe/Ag(111) system, these states have an energy below the vacuum level. Thus, these are bound states in a one-electron picture, since they can escape neither into the metal, because of the projected band gap, nor into vacuum. The quantum well states correspond to quantization of the rare gas conduction band inside the layer, similar to the quantum well states observed in the case of metal overlayers on metals. The higher lying states resulting from the quantization of the conduction band for a Xe overlayer are located above the vacuum level. These are quasi-stationary states in a one-electron picture, and they can decay by electron transmission through the rare gas–vacuum interface. For the lighter rare gases, the bottom of the conduction band is above the vacuum level. All the levels corresponding to the quantization of the conduction band inside the layer are quasi-stationary (resonances) in a one-electron picture in this case.

A theoretical study using the microscopic description of the Ar layer brought evidence for the existence of quantum well resonances in the Ar/Cu(100) system.¹⁵² For thin Ar layers (up to 4 ML), the quantum well resonances were extremely broad with widths in the few hundreds of millielectronvolts range, corresponding to a very high transmission of the Ar–vacuum interface. Analysis of the corresponding wave functions confirmed their origin: quantization of the Ar conduction band. This conclusion was further supported by computation of the dispersion relation $E(\mathbf{k}_{\parallel})$. It corresponded to an effective mass around $0.6m_e$, which was quite close to the electron effective mass inside bulk Ar, consistent with the Ar conduction band origin of the states. Experimentally, the quantum well resonances have been observed and analyzed in detail in the Ar/Cu(100) over a large range of layer thickness by TR-2PPE as well as by one-photon photoemission^{363,364} (see also the article by Güttele *et al.* in this issue). Analysis of the evolution of these states with the layer thickness has revealed an interesting change of their character. For thin layers, these are quantum well resonances inside the layer, but for thick enough layers, they change into interface states located at the metal–Ar interface. Indeed, if we consider a very thick Ar layer on a metal as a continuous medium, we can expect the image potential outside the metal to be very similar to that in the clean metal case, except for a factor, ϵ , where ϵ is the bulk Ar permittivity. Then, image states very similar to the usual ones on clean surfaces should appear, though with a much weaker binding energy converging toward the bottom of the conduction band of the layer. These “image states in an insulator” appear if the insulator layer is thick enough to encompass their breadth; otherwise, reflection at the insulator–vacuum interface transforms these states into the quantum well resonances discussed above. It is remarkable that these states could be observed by photoemission over a very large range of layer thickness, since these states are buried inside the layer, with both the incident photon and the outgoing electron having to travel through the Ar layer. The above interpretation of the evolution of states from quantum-well resonances

to buried image states was supported by calculations using a 1D model for the Ar layer.^{363,364}

Quasi-stationary levels localized inside an insulator thin film and corresponding to the quantization of the insulator conduction band have also been experimentally observed quite a few years ago in another physical context: electron transmission through an insulator thin film adsorbed on a metal surface.^{354,365,366} In these experiments, an electron beam of variable energy was sent toward a metal surface covered by a thin insulator film (rare gas, methane) and the intensity of the transmitted current was recorded as a function of the incident electron energy. The transmission probability was found to exhibit a series of peaks, the positions of which depended on the layer thickness. These peaks have been interpreted as signatures of the quantization of the electron motion perpendicular to the surface; they are the direct analogue of Perot–Fabry transmission resonances in optics. Detailed analysis of the peak position as a function of the layer thickness provided information on the electronic band structure of solid Ar.³⁵⁴ One can then stress that similar quantized states associated with the rare gas conduction band could be found in very different situations: quantum well states, quantum well resonances, and interface states observed in 2PPE experiments and resonances observed in transmission experiments.

Effects of the weak electron transmission through a thin rare gas layer have also been reported in the case of transient states localized on an atom on the surface or on an atom moving with respect to the surface. This is, for example, the case of the core-excited $\text{Ar}^*(2p_{3/2}^{-1}4s)$ adsorbed on a metal surface (see refs 148 and 487 and section 6.5.1 in this review). If the Ar^* atom is located in an Ar layer adsorbed on a metal surface, then the 4s electron transfer to the bulk is much slowed if the 4s electron has to go through the Ar layer. A similar effect was invoked in the case of electron stimulated desorption processes from a surface covered by a rare gas layer.³⁶⁷ In that case, the desorbing ions have to travel through a rare gas layer before escaping into vacuum. As shown by charge-transfer rate computations using the CDM model,³⁶⁸ neutralization of desorbing negative ions is strongly weakened by the presence of a rare gas layer since electron transfer implies tunneling of the electron through a rare gas layer. This change in ion neutralization leads to an increase of the negative ion desorption yield.

The effect of an insulator layer on a metal substrate has also been observed and analyzed for molecular negative ion resonances formed by electron scattering. Transient capture of an electron by a molecule opens the way toward various processes involving an energy transfer from the incident electron to the target molecule: vibrational and electronic excitation of the molecule, dissociation, rearrangement, or desorption (see, e.g., reviews in refs 369–371). When the molecule is adsorbed on a surface, the characteristics (energy and width) of the negative ion resonance are modified by the molecular environment. Electron scattering by molecules adsorbed on a rare gas layer has been studied experimentally in detail.^{372,373} Such resonances in electron scattering are located usually well above the vacuum level, so that the resonances are degenerated with the rare gas conduction band. Although transmission through the layer is possible, theoretical studies using the CDM model³⁷³ or a 3D microscopic description of the layer³⁷⁴ have shown that the reflectivity of the rare gas–vacuum interface is playing a dominant role inducing interferences between scattered waves

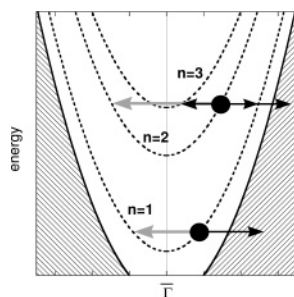


Figure 21. Adsorbate-induced scattering of the Cu(100) image state electrons. The figure shows the energy of the image states (dashed lines) as a function of the electron momentum parallel to the surface, k_{\parallel} . The shaded area represents the 3D bulk states. The intraband and interband scattering processes, that lead to dephasing and population decay of the image states and that are allowed by energy conservation, are indicated schematically by horizontal arrows. Gray arrows indicate the intraband scattering, and black arrows indicate the interband scattering.

and leading to a stabilization of the $N_2(^2\Pi_g)$ molecular resonance in the case of the N_2 molecules adsorbed on an Ar layer on a metal substrate.

6. Adsorbates on Metal Surfaces

The dynamics of excited electrons at surfaces has been discussed above in the case of perfect and clean surfaces. However, one can expect an excited electron localized in the surface area to be extremely sensitive to any modification or any defect on the surface. In particular, adsorbates are very efficient in perturbing the dynamics of excited electrons at surfaces. We can distinguish two kinds of effects induced by adsorbates: (i) A localized adsorbate or defect on a surface acts as a scatterer for the excited electrons traveling on the surface in, e.g., image or surface states, thus perturbing their dynamics; (ii) an adsorbate can itself support localized transient excited states. These states are important in the context of reaction mechanisms, since very often, surface mechanisms involve the transient formation of an excited electronic state localized on an adsorbate as an efficient way of transferring energy between the electronic and the nuclear degrees of freedom.

6.1. Scattering of Delocalized States by Adsorbates

In the case of an electron in an excited-state delocalized on a surface, such as a surface state or an image potential state, one can picture the electron as traveling not far from the surface with a momentum k_{\parallel} , parallel to the surface. On a clean, perfect surface, this electron is traveling quasi-freely. In the presence of a low density of adsorbates at random positions on the surface, one can still consider this electron as quasi-free. However, from time to time, it is scattered by an adsorbate. Because of the very large mass difference between an electron and an adsorbate, one can assume the adsorbate to remain immobile during the scattering so that the electron energy is conserved in the scattering process. Two different scattering processes are possible, as depicted in Figure 21. In a first process, the electron is transferred into another electronic band at constant energy, e.g., scattering from an image potential state into a substrate bulk state or into another image state continuum. This interband scattering process leads to a decrease of the excited state population, i.e., to population decay. In a second process, the electron remains in the same electronic band while it

changes its quantum state at constant energy; for example, an electron initially in a k_{\parallel} state of the n -th image potential state continuum is scattered into the k'_{\parallel} state of the same continuum such that $k_{\parallel} = k'_{\parallel}$, so that only the direction of propagation is changed. This intraband scattering process leads to the decay of the coherence of the electron, without population decay (a process also called “pure dephasing”). In the optical Bloch equation formalism,³⁷⁵ which is very often used to analyze the coherence dynamics of a system, these two processes correspond to the population lifetime T_1 and to the pure dephasing time T_2^* .

In the case of a low adsorbate density on the surface and of a random distribution of the adsorbates on the surface, we can assume that the different scattering centers are independent and incoherent. It is then easy to relate the perturbation induced in the excited-state dynamics by the adsorbate to the scattering cross sections of an individual adsorbate. The corresponding population decay rate Γ_{decay} and “pure dephasing” rate Γ_{deph} are given by refs 153–155:

$$\begin{aligned}\Gamma_{\text{decay}} &= k_{\parallel} n_0 \sigma_{\text{inter}} \\ \Gamma_{\text{deph}} &= k_{\parallel} n_0 \sigma_{\text{intra}}\end{aligned}\quad (86)$$

where σ_{inter} and σ_{intra} are the scattering cross sections for interband and intraband scattering, respectively. n_0 is the adsorbate surface density, and k_{\parallel} is the electron traveling momentum in the initial state. Both population decay and “pure dephasing” contribute to the broadening of the level, and the total broadening rate of the excited state is given by

$$\Gamma_{\text{total}} = k_{\parallel} n_0 (\sigma_{\text{inter}} + \sigma_{\text{intra}}) = k_{\parallel} n_0 \sigma_{\text{total}} \quad (87)$$

where σ_{total} is the total scattering cross section, i.e., the sum of the interband and intraband scattering cross sections.

It is worth noting that the above scattering processes induced by the adsorbates are one-electron processes. On a clean surface, image states are stable in a one-electron formalism and they decay via multielectron interactions or electron–phonon interactions (see e.g. section 2). In the case of a surface covered by adsorbates at random positions, the translational invariance of the surface is broken and one-electron decay processes of the image states are possible. As follows from eqs 86 and 87, the excited state lifetime and the pure dephasing time should vary linearly with the adsorbate coverage for low adsorbate densities on the surface. The above relations implicitly assume that scattering by the different adsorbates is independent and incoherent. This implies that the distance between two adsorbates is larger than the adsorbate scattering cross section (in 2D, the cross sections have the dimension of a length) and then the inverse of the electron momentum, k_{\parallel} . As follows from our studies, σ_{total} diverges as $1/k_{\parallel}$ as k_{\parallel} goes to zero. This limits the applicability of the above relations to finite k_{\parallel} values and to low adsorbate coverages of the surface. These two conditions can be combined into a single condition, $k_{\parallel} \lambda_{\text{MFP}} \gg 1$, where λ_{MFP} is the electron mean free path on the surface. This is the Joffe–Regel condition,³⁷⁶ beyond which a new scattering regime appears. When the coverage increases and when the ranges of action of the different scatterers on the surface start to overlap, the above relations are not valid anymore and another formulation should be sought to describe the adsorbate effect on excited states in which scattering by one adsorbate occurs under the influence of all the other adsorbates on the surface (see, e.g., the discussion in refs

154 and 377). One can also stress that the above scattering view of the adsorbate effect only applies to the case of adsorbates at random positions on the surface. The situation is quite different in the case of an ordered adsorbate layer. The periodicity of the adsorbate-induced potential along the surface leads to band-folding effects (see section 5). Under band-folding, the surface localized states may either remain bound states in a one-electron picture or decay into the 3D continuum of the bulk states via the exchange of a reciprocal lattice vector of the adsorbate lattice.

The effect of the presence of various adsorbates on image states has been studied theoretically in various systems using the scattering formalism outlined in section 2.2.1. The main ingredients in the calculation are (i) the interaction potential between the electron and the clean surface, V_{e-surf} , which defines the unperturbed image potential states, and (ii) the local perturbation introduced by the adsorbates, V_{ads} . The wave packet propagation study of electron evolution in the $V_{e-surf} + V_{ads}$ compound potential allows extracting the scattering cross sections (both intraband and interband) for an electron initially in a given image state continuum (see section 2.2.1). The model potential developed in ref 157 is used to describe the V_{e-surf} interaction. This potential is a function of the electron coordinate perpendicular to the surface only. Free-electron motion parallel to the surface is then assumed. This model potential has been derived from first principle calculations to reproduce the main features of the electronic band structure at the $\bar{\Gamma}$ point (projected band gap, energies of the image, and surface states). Different representations of the V_{ads} potential have been used depending on the type of adsorbed species under study. These involved pseudopotentials for alkali adsorbates^{153–155} or Ar adsorbates,¹⁵⁵ model potentials for electronegative adsorbates,¹⁵⁵ or potentials extracted from first principles DFT calculations of the adsorbate–substrate system in the case of Cu adatoms on a Cu(100) surface.¹⁴⁹ In this last case, joining a model potential description to a V_{ads} potential extracted from DFT calculations has several advantages. It allows us to properly include the image potential and, thus, to get a proper description of the image states, which would not be the case with a local exchange–correlation potential in the DFT treatment. On the other hand, the adatom-induced perturbation, being extracted from a comparison between DFT calculations on Cu(100) and Cu/Cu(100) systems, retains all the information from this first principle approach.

As an example of the effect of scattering by adsorbates on image state dynamics, Figure 22 presents the adsorbate-induced decay rate of the $n = 1$ and $n = 2$ image states on a Cu(100) surface with Cs adsorbates.¹⁵³ The results are shown as a function of the electron energy with respect to the vacuum level (the bottoms of the $n = 1$ and $n = 2$ image state continua are located at -0.573 and -0.177 eV, respectively). The decay rate is expressed in millielectronvolts for a Cs coverage of the surface equal to one Cs adsorbate per 1000 Cu surface atoms.

As a first remark, the adsorbate-induced decay rate exhibits a few structures as a function of the electron energy. Some of these structures are related to the opening of new decay continua for the image states; for example, the structure labeled (1) is associated with the opening of the $n = 2$ image state continuum as a decay channel for scattering of an $n = 1$ electron. Similarly, the structures labeled (2) and (5) are associated with the thresholds of the $n = 3$ and $n = 4$ continua. Other structures, such as structures (3) and (4),

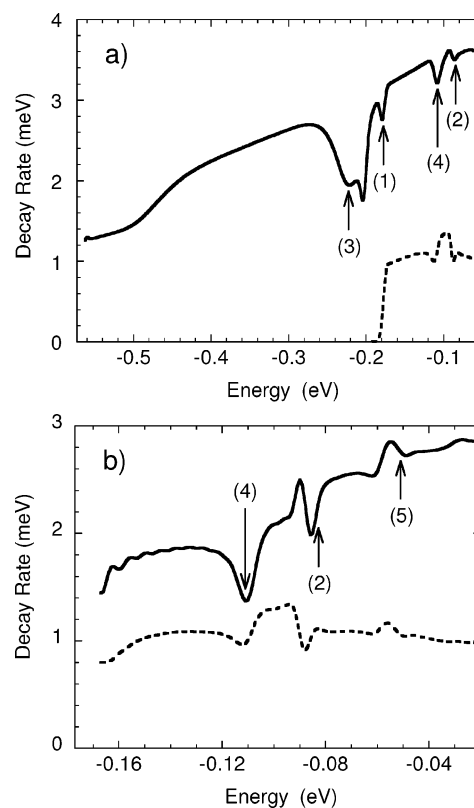


Figure 22. (a) Total and partial decay rates (in meV) of the $n = 1$ image state on a Cu(100) surface induced by electron scattering from Cs adsorbates. The theoretical results¹⁵³ are presented as functions of the electron total energy measured with respect to the vacuum level. The abscissa-axis starts at the bottom of the $n = 1$ image state continuum (-0.573 eV). The Cs adsorbate coverage corresponds to 1 Cs adsorbate per 1000 Cu surface atoms. Assignment of the structures is explained in the text. Solid line: total decay rate. Dashed line: partial decay rate corresponding to the interband transition into the $n = 2$ image state continuum. (b) The same as above for the $n = 2$ image state. The abscissa-axis starts at the bottom of the $n = 2$ image state continuum (-0.177 eV). Solid line: total decay rate. Dashed line: partial decay rate corresponding to the interband transition into the $n = 1$ image state continuum.

located slightly below the image state continua thresholds, are due to adsorbate-induced resonances, associated with the localization of the image state continua (see the discussion below in section 6.3). The adsorbate-induced resonances can appear as peaks or as dips in the scattering cross sections, as they are associated with the transient capture of the scattered electron by the adsorbate. The decay induced by Cs adsorbates on Cu(100) is quite efficient: for energies close to $\bar{\Gamma}$, the $n = 2$ decay rate induced by Cs adsorbates amounts to 1.5 meV for a 0.001 ML coverage. This can be compared to the decay rate of the $n = 2$ image state on clean Cu(100), which is in the 4–5 meV range.^{286,295} Thus, for Cs coverages in the few 10^{-3} ML range, the lifetime of the $n = 2$ image state is dominated by adsorbate scattering. So, even trace concentrations of alkali adsorbates are able to significantly affect the dynamics of the image states at surfaces. Another qualitative feature appears in Figure 22. When they are possible, transitions between image states are very efficient. Thus, decay of the $n = 2$ image state is dominated by the interband scattering into the $n = 1$ image state continuum. This is attributed to a large spatial overlap, that favors transitions between image states rather than from an image state into substrate bulk states.

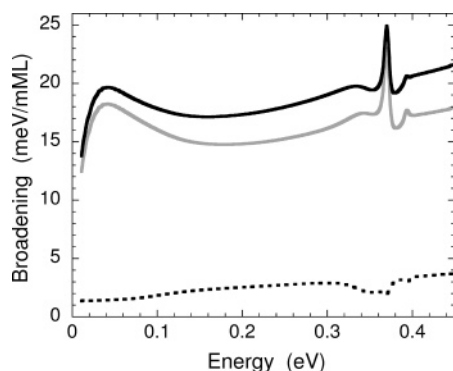


Figure 23. Broadening (in meV/mML) of the $n = 1$ image state on a Cu(100) surface induced by Cs adsorbates. The theoretical results¹⁵⁴ are presented as a function of the electron translational energy parallel to the surface, so that zero energy corresponds to the bottom of the $n = 1$ image state continuum (-0.573 eV with respect to the vacuum level). Dotted line: population decay rate. Gray line: dephasing rate. Solid line: total broadening.

In the case of scattering of Cu(100) image states by alkali adsorbates, the interband scattering process appears to be significantly weaker than intraband scattering; that is, adsorbate-induced decay is weaker than adsorbate-induced pure dephasing. This is illustrated in Figure 23, which shows the decay rate, the pure dephasing rate, and the total broadening rate (sum of the first two) for the $n = 1$ image state of the Cu(100) surface covered with Cs adsorbates.¹⁵⁴ The rates are expressed in millielectronvolts per millimonomolayer (meV/mML). Results are presented as a function of the electron energy with respect to $\bar{\Gamma}$: $E - E_{\bar{\Gamma}} = k_{\parallel}^2/2$. The pure-dephasing rate appears to be an order of magnitude larger than the decay rate. In this system, this is attributed to the presence of a strong dipolar part in the scattering potential, V_{ads} . Alkalis adsorb as positive ions on metal surfaces at low coverages, and the adsorbate charge is screened by its image charge in the metal, leading to a large local electric dipole (for Cs/Cu(100) it amounts to 7 au). The long-range dipolar part of V_{ads} efficiently scatters the electron for distant collisions, leading to large intraband cross sections. The angular momentum resolved intraband scattering probabilities (see section 2.2.1) slowly decrease when m , the angular momentum of the scattered electron, is increased. In contrast, interband scattering, i.e., adsorbate-induced decay processes, requires more short-range collisions; their convergence with increasing m is much faster, leading to a decay rate significantly smaller than the pure dephasing rate in this system. The general trend of decreasing scattering cross sections with increasing m can be understood from the centrifugal barrier growth, $m^2/2\rho^2$, which does not allow an electron to approach close enough to the scatterer.

Theoretical study of the effect of different adsorbates on the dynamics of image states on Cu(100) surfaces allowed for the characterization of the relative importance of the various processes and their link with the scatterer properties.

(a) As illustrated above, alkalis are very efficient scatterers, leading to significant contributions in the image state decay, even for very low adsorbate densities, in the 10^{-3} ML range.^{153–155} Local dipoles induced by alkali adsorbates lead to a very efficient pure dephasing process, an order of magnitude stronger than the decay process.

(b) Tests for a model electronegative adsorbate were performed with a V_{ads} taken as a repulsive Coulomb potential associated with its electric image in the metal.¹⁵⁵ The induced dephasing rate was found to be of the same order, though

numerically different from that of an analogous alkali. This confirms the role of the dipolar potential as a key ingredient for the dephasing process. For all the systems that were studied, the strength of the dephasing process was found to follow the importance of the dipolar potential; however, there is no direct proportionality, and the situation is far from perturbative. Decay induced by a model electronegative adsorbate is much less efficient than that by an alkali adsorbate (except at large traveling energies). This confirms the importance of short-range interactions for the decay process: in the electronegative adsorbate case, the repulsive Coulomb potential prevents the electron from approaching close to the adsorbate center.

(c) Ar adsorbates (V_{ads} pseudopotential taken from ref 152) were found to be much weaker scatterers than charged adsorbates.¹⁵⁵ Indeed, the long-range part of the V_{ads} potential is only due to polarization of the Ar adsorbate; it is weaker and of shorter range than the dipolar potential present in the alkali adsorbate case, and thus, it leads to a much weaker dephasing rate, quickly decreasing with n . As for the population decay rate, it is typically 2 orders of magnitude smaller than that for alkalis.

(d) Cu adatoms on Cu(100) are associated with a dipole smaller than that of alkalis. The Cu adatom-induced processes are quite efficient though significantly smaller than those for alkalis, in particular the dephasing process. The relative importance of decay and dephasing is found to vary with the image state principal quantum number, with the decay dominating for $n > 1$.¹⁴⁹

Experimentally, the influence of surface defects, in particular of adsorbates, on the dynamics of image and surface states has been recognized very early. Kevan^{378–380} was the first to propose scattering by adsorbates and defects as a major broadening cause in photoemission experiments. Since then, the development of TR-2PPE techniques in the femtosecond range allowed the direct study in the time domain of the excited state dynamics and, in particular, of the excited state lifetime and coherence decay time. Analysis of the adsorbate effect revealed, in certain cases, a linear variation with the adsorbate density, consistent with the independent scattering framework outlined above. For example, line widths of surface and image states in photoemission experiments have been found to vary linearly with the adsorbate coverage^{379–384} in the low adsorbate coverage range. In the case of Na adsorbates on Cu(111) surfaces, the experimental broadening induced by the adsorbates³⁸³ was found to be quite large, around 12 meV/mML at the bottom of the $n = 1$ image state continuum. The magnitude of this effect is quite consistent with the one found in the theoretical studies presented above which showed scattering by alkalis to be very efficient in perturbing the image state dynamics;¹⁵⁴ in the Na/Cu(111), the theoretical prediction for the total broadening was found to be 5 meV/mML at the bottom of the $n = 1$ continuum, quickly rising to 17 meV/mML for electron traveling energies in the few 100 meV range.

More recently, detailed TR-2PPE studies were devoted to the dynamics of image potential states on Cu(100) in the presence of Cu adatoms or of CO adsorbates.^{297,385–390} In the range of low adsorbate coverages, these experiments showed a linear variation of the image state lifetime and coherence decay time, with a slope typically in the 0.1–1 meV/mML range. Scattering by CO or by Cu adatoms was found to affect the electron dynamics in qualitatively different

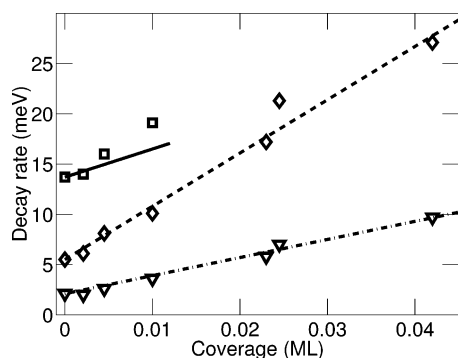


Figure 24. Population decay rate of the $n = 1$, $n = 2$, and $n = 3$ image states on Cu(100) induced by Cu adatoms. The decay rate (in meV) is presented as a function of the adatom coverage of the surface (in monolayers). Theoretical results from ref 149 (lines) are compared to the experimental results from Refs 387 and 388 (symbols). Full line and open squares: $n = 1$ image state. Dashed line and open diamonds: $n = 2$ image state. Dashed–dotted line and open triangles: $n = 3$ image state.

ways: CO adsorbates lead to larger changes in the dephasing rate than in the decay rate, whereas Cu adatoms lead to the opposite relative importance. Experimental data on the effect of Cu adatoms can be compared with recent theoretical results obtained in a joined DFT-WPP study of scattering of Cu(100) image states by Cu adatoms.¹⁴⁹ Figure 24 presents the population decay rate of the $n = 1$, $n = 2$, and $n = 3$ image states on Cu(100) as a function of the Cu adatom coverage.¹⁴⁹ The theoretical value is obtained by adding the computed contribution due to scattering by adatoms to the population decay rate on clean surfaces as determined from experiment.^{387,388} An excellent agreement can be seen in Figure 24 between theory¹⁴⁹ and the experimental data from refs 387 and 388. Two qualitative features seen in Figure 24 can be highlighted. First, the population decay rate is much perturbed by Cu adatoms and the image state dynamics appears to be dominated by adsorbate scattering for coverages in the range of a few 10^{-2} ML. Second, the effect of scattering by the Cu adatoms is not a monotonic function of n , the principal quantum number of the image states. This may seem surprising, since one would expect these Rydberg-like states to exhibit simple scaling laws as a function of n . Typically a perturbation located close to the surface would induce rates varying like n^{-3} , reflecting the variation of the spatial spread of the image state wave function in the vacuum region. Detailed analysis of the Cu/Cu(100) theoretical results showed that, although not perfect, simple scaling laws can be retrieved when looking at individual processes, with the situation being different in the case shown in Figure 24 where several channels contribute to the induced population decay. Indeed, at $\bar{\Gamma}$, an $n = 1$ image state electron can only be scattered into bulk states whereas an $n = 2$ electron can also be scattered into the $n = 1$ continuum. Transitions between image states have been shown both experimentally and theoretically to be very efficient when they are possible,^{153,297,389–391} and this accounts for the increased decay rate when going from $n = 1$ to $n = 2$.

The presence of adsorbates on a surface is not only perturbing the time evolution of image and surface states, it is also changing their energy. Keeping the above scattering view, forward scattering at a vanishing angle does not correspond to inter- or intraband scattering, but it is associated with a phase shift of the electronic wave traveling on the surface, thus leading to a change of the traveling energy of the electron.¹⁵⁴ In the limit of small energy change and

low adsorbate coverage, this energy change, ΔE , is equal to¹⁵⁴

$$\Delta E = \sqrt{2\pi k_{\parallel}} n_0 \text{Re}(f(0)e^{-i\pi/4}) \quad (88)$$

where $f(0)$ is the scattering amplitude at zero angle and n_0 is the adsorbate concentration. In the case of alkali/Cu(111), ΔE reaches the few meV per mML range. For higher coverage, an approach has been developed to represent the adsorbate coverage dependence of the image state energy.³⁷⁷ Basically, it consists of singling out one adsorbate and grouping together all the other distant ones. Averaging the potential created by the distant adsorbates allows for the perturbation of the V_{ads} potential discussed above by all the distant adsorbates. This produces a new compound potential $V_{\text{e-surf}} + V_{\text{ads}}$ that depends on the adsorbate coverage of the surface. Application of this approach to the computation of the image state energy in the Na/Cu(111) system³⁷⁷ reproduces very well the coverage dependence observed by Fischer *et al.*³¹⁷ It could also provide a basis for the extension of the scattering approach of decay and dephasing to large adsorbate coverage.

Defects other than adsorbates at surfaces can also scatter a surface state or image state electron and thus alter their dynamics. The presence of steps, for example, has been shown to influence the image state dynamics. Various processes can occur when an image state electron approaches a step: it can be scattered into another electronic band, it can be reflected by the step, or it can cross the step. These various processes lead to coherence and population decay of the image state, in a way similar to scattering by adsorbates. Experiments have been performed with vicinal surfaces; in this case, scattering occurs due to the irregularities in the step–terrace sequence which breaks the translational invariance of the surface, whereas the periodicity introduced by the vicinal surface results in a folding of the image state bands.^{392–394} The effect of the steps shows up as a momentum dependence of the state lifetime for electrons traveling perpendicular to the step, associated with an asymmetry of the lifetime between electrons propagating up-stairs or down-stairs.^{393,394}

Scattering of surface electrons by adsorbates is influencing many phenomena at surfaces and not only the dynamics of image and surface state electrons. The next section discusses the case of scattering by defects and nanostructures at surfaces as probed by STM. Scattering by adsorbates is also invoked in a few other fields as surface resistivity^{395,396} and its link to surface infrared reflectivity,^{397,398} or surface electromigration.^{399,400}

6.2. Scattering by Defects Probed by Scanning Tunneling Microscopy

The above-discussed experiments looked at the effect of scatterers on delocalized states at surfaces, by studying their global properties (energy, lifetime, coherence time) corresponding to an integration of the scatterer effect over the entire surface. These scattering effects can be looked at more directly and locally in an STM experiment that images the electronic density of states close to the Fermi energy. If a scatterer (a step or an adsorbed impurity) is present on the surface, it generates standing waves that can be observed as a spatial modulation in the local density of states. These have been imaged experimentally, for both surface state^{401–405} and image state electrons^{56,406} scattered by steps or impurities.

Detailed analysis of these standing waves and of the decay of the corresponding modulation when moving away from the scatterer allows the extraction of several parameters of the continuum states: the energy dispersion relation of the 2D continuum, the reflectivity, the scattering phase shift, and the coherence length. Scattering by individual adsorbates is also involved in the treatment of the long-range interaction between them.^{407–411} It has been shown that a significant part of this interaction is mediated by surface state electrons and that the long-range interaction oscillates with a period given by the Fermi momentum and a phase equal to the scattering phase shift of the adsorbate.⁴¹²

The same scattering processes also play a very important role in artificially designed nanostructures at surfaces. Electrons confined in quantum corrals or between steps experience scattering at the edges of the structure which confines them.^{413–419} For example, a resonator can be formed by manipulating adsorbed atoms one by one to form a closed line of atoms encircling a given region of the surface. The electrons in the 2D surface state continuum are reflected by the line of adsorbates, leading to interferences and to a “particle-in-a-box” quantization. It is noteworthy that scattering at the edge of the structure leads to the same kind of processes as those discussed in the previous subsection: reflection on the structure edge, transmission through the structure edge, or scattering into the 3D bulk states. The last two processes appear as losses leading to the broadening of the states quantized in the structures. The corresponding finite width has been discussed theoretically using different models.^{414–419}

Similar effects can also be found in the case of finite size adsorbate islands on a surface. The image state and surface state electrons can be confined on the island, and the scattering at the edge of the island leads both to quantization and to decay of the quantized states. Photoemission studies of incomplete adsorbate layers on surfaces show the coexistence of two kinds of image states: on the adsorbate islands and on open substrate patches.^{21,345} A detailed STM study of surface state confinement on Ag islands on Ag(111) revealed all the variety of different confined states that could be formed.⁵⁵ The widths of these quantized states have also been addressed. Recently, the problem of confinement of image states on Ar islands on Cu(100) has been investigated, by a WPP approach (see section 2.2.1) allowing the quantitative treatment of electron scattering at the island edge. It showed that electron transmission through the island edge has a very high probability, leading to an efficient decay of the confined states even for rather large island sizes.⁴²⁰

6.3. Localization of 2D Continua by Defects at Surfaces

As discussed above in connection with Figure 22, the study of image state electron scattering by an alkali adsorbate reveals the existence of resonances, i.e., of transient states localized on the adsorbate site with an energy slightly below the thresholds of the image state continua.¹⁵³ Similar states appearing below the bottom of the image state or surface state continuum have also been found in the case of atoms interacting with certain surfaces, e.g. Cu(111).^{83,160} Similarly, for atoms interacting with a thin metal film,⁴²¹ the presence of the projectile leads to states splitting off the bottom of the 2D continua of the thin film. The origin of these extra states has been discussed¹⁴⁷ in connection with a theorem

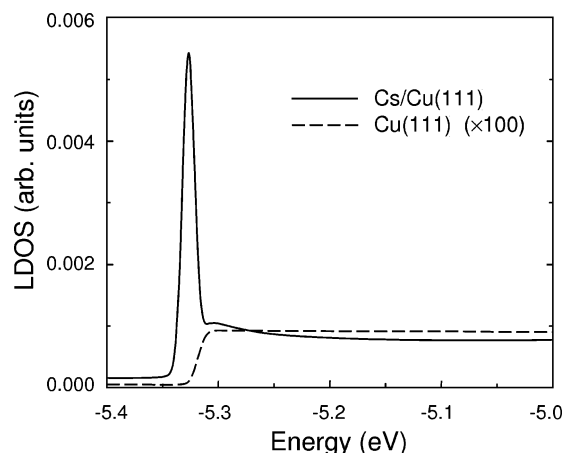


Figure 25. LDOS as a function of the electron energy for the Cs/Cu(111) (full line) and clean Cu(111) (dashed line) systems. The probe point is located $6a_0$ above the Cs adsorbate, in the on-top position. The energy is in eV and refers to the vacuum level. The resolution of the LDOS has been limited by a Gaussian filter with a width of 12 meV. Note the multiplicative factor on the clean Cu(111) curve.

by Simon,⁴²² who showed that an attractive potential with certain properties always has a bound state in 2D and 1D. One could then expect that a 2D continuum perturbed by an attractive adsorbate will lead to a bound state, i.e., that the adsorbate will induce a localization of the 2D continuum. Zaremba *et al.* confirmed this idea, demonstrating that the potential of an ion screened by a 2D electron gas still supports bound states despite not being attractive in some regions of space.^{423,424} However, the surface problem is a 2D problem embedded in 3D. The bound state resulting from the adsorbate-induced localization is not stationary, but it is a quasi-stationary state, or resonance, as it can decay into the 3D continuum of bulk states.

The localization phenomenon is illustrated in Figure 25, which presents the theoretical prediction for the local density of states (LDOS) calculated at $6a_0$ above a Cs adsorbate on a Cu(111) surface.¹²⁶ The LDOS has been computed using a wave packet propagation approach (see section 2.2.1). The result for the Cs/Cu(111) system is compared to the LDOS for a clean Cu(111) surface. On the clean surface, the LDOS is rather flat and exhibits a sharp step at the energy of the bottom of the surface state continuum, as expected for a 2D continuum. The step should be infinitely sharp, and it appears rounded in Figure 25 due to the finite propagation time (energy resolution estimated of the order of 12 meV). When the Cs adsorbate is present, the localization of the 2D surface state continuum induced by the adsorbate results in a narrow peak appearing slightly below the surface state continuum bottom. The finite width of the peak reflects the quasi-stationary nature of the adsorbate-induced state which can decay into the 3D states of bulk Cu. Similarly to the case of the clean Cu(111) LDOS, an additional broadening is due to the finite propagation time in the calculation. In the present Cs/Cu(111) case, the adsorbate possesses localized resonance states deriving from the atomic orbitals of the Cs atom. These resonances are located more than 2 eV above the bottom of the surface state continuum (see the next section), and the localization brings a new state split off the bottom of the 2D continuum. This follows from the properties of the 2D density of states as argued via Simon's theorem; however, it can also be simply demonstrated with the model Anderson–Newns Hamiltonian applied to a 2D continuum problem (see

the next section and ref 83) that an extra state appears below the 2D surface state band bottom.

The WPP approach can also be used to compute the wave functions of such extra states appearing from 2D localization (see section 2.2.1). For the coordinate perpendicular to the surface, the wave function of such a resonant state is very similar to the wave function of the “mother” 2D continuum. Parallel to the surface, the resonant state has a finite extension corresponding to its binding energy with respect to the 2D continuum. This wave function is very different from that of the “usual” adsorbate localized states which correspond to the various atomic orbitals of the adsorbate atom perturbed by their interaction with the surface.

The localization of the image state continuum has been predicted to occur for alkali adsorbates,¹⁴⁷ as well as for Ar adsorbates.¹²⁶ In the latter case, no bound state exists in the free adsorbate system; nevertheless, the weak attractivity of the V_{ads} potential is able to induce a localization of the image state continuum, though with an extremely small binding energy. A similar localization effect has been predicted for the surface state continuum.¹²⁶ Scanning tunneling microscopy experiments in the spectroscopic mode (STS) have recently revealed these extra states resulting from the surface state localization by Cu adatoms on a Cu(111) surface.^{151,425} A detailed joined theory–experiment analysis¹⁵¹ of the various peaks in the local density of states allowed us to recognize all the peaks corresponding to atomic orbitals and to assign the peak appearing just below the Cu(111) surface state continuum and localized around the Cu adatoms to the localization phenomenon. Peaks localized around adsorbates and located just below the surface state continuum have been observed in several other systems: Cu and Co adsorbates on Au(111),⁴²⁶ Ag on Ag(111),⁴²⁵ and S adsorbates on Ag(111).⁴²⁷ No detailed assignment could be performed as for Cu/Cu(111), but the similarity between these systems and the Cu/Cu(111) system strongly suggests that, in these systems too, the surface state localization is the origin of the surface state band edge peaks.

Finally, one can also mention other instances where the localization of a 2D continuum could be invoked: steps^{406,428–432} and atomic lines⁴³³ have been found to be associated with states localized on the defect and located just below the bottom of a 2D continuum. In these cases, the perturbing potential is 1-dimensional and it leads to 1D states localized perpendicular to the defect and delocalized parallel to it.

6.4. Transient States Localized on Adsorbates at Surfaces

Excited electronic states localized on adsorbates have attracted a lot of interest. Indeed, these states are often invoked as intermediates in surface reaction mechanisms: the formation of an excited state favors an energy transfer from the excited electron to the heavy particle motion and thus opens the way toward rearrangement processes. In this context, the lifetime of the transient state is a key parameter and often a very short lifetime is a bottleneck in the reaction scheme.⁴³⁴ Another key parameter for the dynamics of an intermediate state is its dephasing time, which controls the evolution of the coherence of the excited state, once it has been created. This parameter governs the possibility of coherent control⁴³⁵ of the reaction path; such a possibility has been recently demonstrated on a surface process.⁴³⁶

Generally, on a metal surface, the most efficient decay process of an excited electronic state localized on an adsorbate is a one-electron energy-conserving electron transfer process in which the discrete excited electron is resonantly transferred into the continuum of metal states (resonant charge transfer (RCT) process). Other processes in which the energy of the excited state is partly transferred to a multielectron excitation in the metal are also possible. However, when it is possible, the one-electron RCT process is in general more efficient than multielectron processes. In many cases, an easy way to picture the quasi-stationary excited states located on the adsorbate is to consider an atom colliding on the surface. When an atom approaches a metal surface down to chemisorption distances, its electronic levels couple with the metal continuum of states, so that the resonant charge-transfer process presents the characteristics of a discrete state-continuum transition. Stationary atomic states thus become quasi-stationary states, or resonances, localized on the adsorbate.

Early studies of the adsorbate-induced resonances trace back to the model Anderson–Grimley–Newns (A-G-N) Hamiltonian, which was first introduced by Anderson to treat the dilute impurity problem in bulk metals.⁴³⁷ Later it was adapted by Grimley and Newns to study the chemisorption of adatoms on a metal surface.^{438,439} Here, we limit ourselves to the simplest example; a detailed discussion of the A-G-N Hamiltonian can be found in ref 440. In a simple one-electron picture, one considers an atomic orbital of the adsorbate $|a\rangle$ corresponding to the energy level E_a coupled to the continuum of metal states $|\mathbf{k}\rangle$. Assuming the orthonormality of the $\{|a\rangle, |\mathbf{k}\rangle\}$ basis, the Hamiltonian of the system takes the form

$$H = |a\rangle E_a \langle a| + \sum_{\mathbf{k}} |\mathbf{k}\rangle E_{\mathbf{k}} \langle \mathbf{k}| + \sum_{\mathbf{k}} \{ |a\rangle V_{a\mathbf{k}} \langle \mathbf{k}| + \mathcal{C}\mathcal{C} \} \quad (89)$$

where $E_{\mathbf{k}}$ is the energy of the \mathbf{k} continuum state and $V_{a\mathbf{k}} = \langle a|H|\mathbf{k}\rangle$ are the coupling matrix elements. $\mathcal{C}\mathcal{C}$ stands for the Hermitian conjugate. The density of states projected on the atomic state $|a\rangle$ can be straightforwardly obtained from the diagonal element of the Green function:

$$n_a(\omega) = -\frac{1}{\pi} \text{Im} G_{aa}^+(\omega) \quad (90)$$

$$= -\frac{1}{\pi} \text{Im} \left\langle a \left| \frac{1}{\omega + i\eta - H} \right| a \right\rangle \quad (91)$$

Introducing a broadening

$$\Gamma(\omega) = 2\pi \sum_{\mathbf{k}} |V_{a\mathbf{k}}|^2 \delta(\omega - E_{\mathbf{k}}) \quad (92)$$

and a shift function

$$\Lambda(\omega) = \mathcal{P} \left(\sum_{\mathbf{k}} \frac{|V_{a\mathbf{k}}|^2}{\omega - E_{\mathbf{k}}} \right) \quad (93)$$

where \mathcal{P} stands for the Cauchy principal part, the Green function takes the form

$$G_{aa}^+(\omega) = \frac{1}{\omega - E_a - \Lambda(\omega) + i\Gamma(\omega)/2} \quad (94)$$

In the weak coupling limit (small V_{ak}), the density of states $n_a(\omega)$ presents a Lorentzian profile centered at

$$E = E_a + \Lambda(E) \quad (95)$$

with the width $\Gamma = 2\pi \sum_{\mathbf{k}} |V_{ak}|^2 \delta(E - E_{\mathbf{k}})$. E and Γ are associated, respectively, with the position and the width of the quasi-stationary adsorbate-localized state.

At this point, it is interesting to go back to the 2D localization problem (see also ref 83). Let us assume that $|\mathbf{k}\rangle$ are the states of a 2D surface state continuum and that the atomic orbital energy E_a is located at positive energy with respect to the bottom of the surface state continuum. The energies of the quasi-stationary states are given by the E solutions of eq 95. Summing over the degeneracies and switching from summation over \mathbf{k} to integration over the continuum energy, ϵ , in eq 93, we obtain the shift function $\Lambda(E)$ as

$$\Lambda(E) = \mathcal{P} \left(\int_0^\infty \frac{|V_{a\epsilon}|^2}{E - \epsilon} d\epsilon \right) \quad (96)$$

The surface state is a two-dimension continuum, and so, the threshold law for the interaction is such that $|V_{a\epsilon}|^2$ goes to a constant when ϵ goes to 0^+ . As a consequence, the shift function (eq 96) has a logarithmic divergence for E going to zero. For negative energies, the shift function $\Lambda(E)$ is negative and monotonic, and it behaves as A/E for large negative E . As a consequence, eq 95 always has a solution for negative energies; that is, there always exists a bound state for such a problem, even if E_a is positive. For small discrete state-continuum interactions, the binding energy becomes exponentially small. Thus, the 2D localization phenomenon is always present if there is an adsorbate-localized state transforming into a resonance located at positive energies with respect to the 2D continuum bottom. However, this requirement is more restrictive than the conditions imposed by Simon's theorem, where the existence of a localized level E_a is not required (see above).

While the A-G-N Hamiltonian provides the basic understanding of the adsorbate-induced resonances at surfaces, quantitative calculations of the resonance energies and widths are beyond the scope of this approach. The first nonperturbative studies of the quasi-stationary states localized on adsorbed species were performed in the case of a free-electron metal surface by Lang and Williams with the density functional approach.⁴⁴¹ For later studies based on the DFT approach, we refer the reader to a recent review paper.⁴⁴²

However, the most active developments in the study of atomic resonances at surfaces came from the field of collisional charge transfer between atomic projectiles and surfaces. Here, the knowledge of the energies and widths of the quasi-stationary states localized on the projectile is required to compute charge fractions in the scattered/sputtered beams. Several theoretical methods have been developed and applied for atom-surface distances ranging from chemisorption to large separations. All these methods address the same basic problem: they search for the quasi-stationary states (resonances) for a given model of the one-electron interaction potential between the excited electron and the adsorbate (projectile) + substrate system. These resonances correspond to the transient adsorbate states, and their width is equal to the RCT rate, i.e., to the inverse of the adsorbate state lifetime against electron transfer. The

various approaches listed below are exact for the given model potential. They differ in the method chosen to locate the quasi-stationary states: the complex scaling method,⁴⁴³ the scattering approach for the coupled angular mode method (CAM),⁴⁴⁴ stabilization,^{445,446} close coupling,^{447,448} or wave packet propagation.^{83,449} The latter approach has been presented in more detail in section 2.2.1. These methods allow parameter-free determinations of the charge-transfer characteristics. In the case of free-electron metal surfaces, they yield predictions in quantitative agreement with experimental results on collisional atom-surface charge transfer.^{450,451}

On free-electron metals, the charge transfer rate is found to vary roughly exponentially with the atom-surface distance and to reach the 1 eV range for typical adsorption distances. For alkali adsorbates, for example, this leads to lifetimes shorter than 1 fs for the adsorbate localized states. The model-potential methods agree with *ab initio* density functional studies performed specifically on the adsorbate/surface system.^{441,442,452-454} The very fast charge-transfer process in fact precludes any role of such excited states as intermediates in a reaction scheme. In this context, the experimental observation by TR-2PPE of a very long-lived excited state in the alkali/Cu(111) system was very attractive.⁴⁵⁵⁻⁴⁵⁹ In the Cs/Cu(111) system, the lifetime reaches a few tens of femtoseconds. At low alkali coverage, alkalis adsorb on a metal surface as positive ions.^{442,460,461} The long-lived excited-state localized on the alkali then corresponds to the transfer of an electron from the metal substrate on the adsorbate.

The experimentally observed drastic reduction of the charge-transfer rate on Cu(111) was reproduced by wave packet propagation studies and explained as due to the peculiarities of the electronic band structure of the Cu(111) surface.^{83,141,462} The Cu(111) surface exhibits a projected band gap (L-gap) in the $\langle 111 \rangle$ direction normal to the surface, and the alkali adsorbate-induced resonance lies inside this projected band gap. In fact, for most of the studied systems, alkali-adsorbate localized resonances have an energy typically 2 eV below the vacuum level. The effect of the L-gap on the Cs-localized excited state is illustrated in Figure 26, which presents the electron density associated with the resonant wave function in the case of a free-electron metal and in the case of a Cu(111) metal surface. The interpolated image of the logarithm of the electron density is shown in cylindrical coordinates (the z -axis is normal to the surface and goes through the adsorbate center). In the free-electron case, one recognizes the Cs atomic orbital perturbed by the interaction with the surface and centered around the adsorbate at the origin of the coordinates. The resonant electron transfer appears as a large electronic flux along the normal to the surface. The RCT process corresponds to electron tunneling from the adsorbate to the substrate. It is much favored along the surface normal, which is the "easiest" direction due to the lowest potential barrier separating the atomic potential well and the metal.

The situation is quite different for Cu(111). In Figure 27 we schematically show the different states of the 3D bulk or 2D surface continua which are energetically available for RCT from the adsorbate localized state. The adsorbate-induced resonance lies within the projected band gap. There is no bulk state propagating along the normal to the surface at this energy, and thus, resonant electron transfer from the Cs orbital is impossible along the normal to the surface. Hence, electron transfer has to involve states with a finite k_{\parallel}

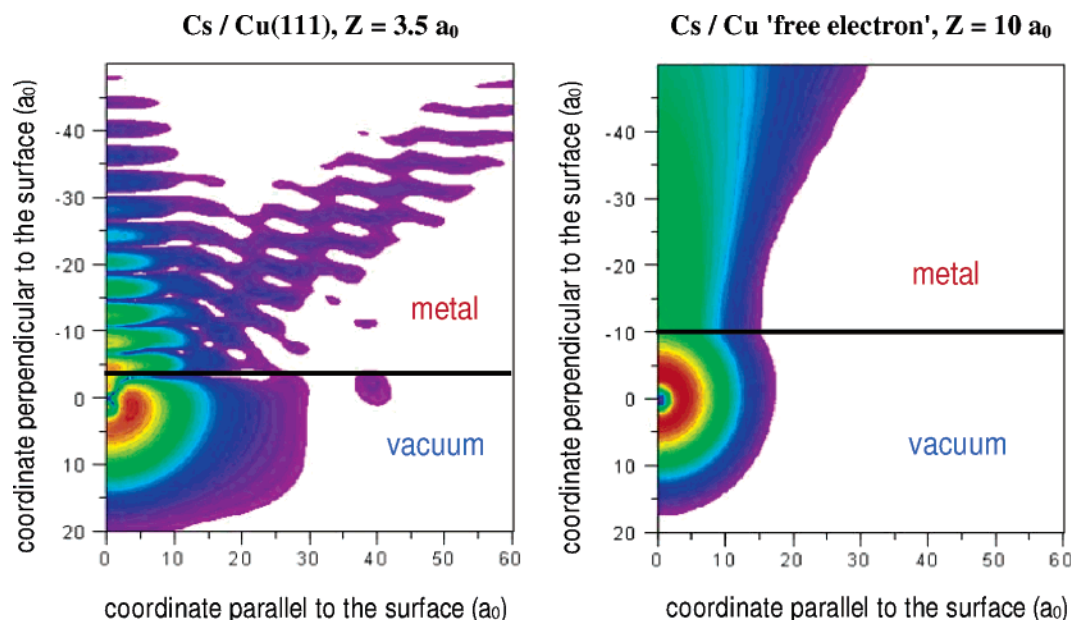


Figure 26. Interpolated image of the quasi-stationary Cs-localized state in the case of the Cs atom located (left) at $3.5a_0$ (adsorption distance) from the image plane of a Cu(111) surface and (right) at $10a_0$ from the image plane of a free-electron metal surface. The position of the image plane of the metal surface is indicated by the horizontal black line. The logarithm of the electronic density (square modulus of the wave function) is presented in cylindrical coordinates parallel and perpendicular to the surface. z , the coordinate perpendicular to the surface, is positive in a vacuum. The Cs atom center is located at the origin of coordinates. The electron density decreases when going from red to violet. White corresponds to very small electron densities.

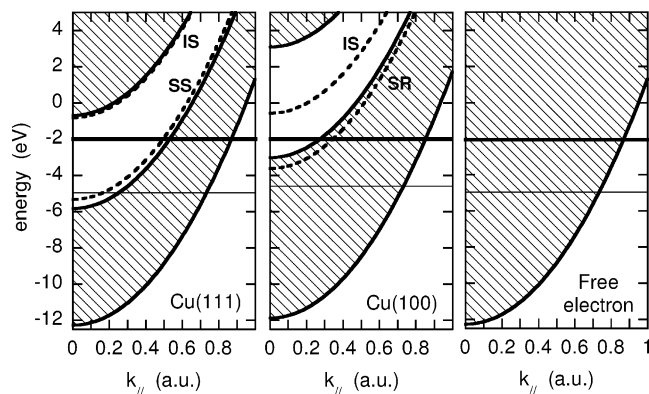


Figure 27. Energy of the electronic states in the model Cu(111), Cu(100), and free electron metal surfaces, as a function of the electron momentum parallel to the surface, $k_{||}$. Vacuum is at zero energy. The 3D electronic states are represented by the hatched area. The surface and first image states (dashed lines) are labeled SS and IS, and the surface resonance on Cu(100) is labeled SR ($E_{SS} = -5.33$ and $E_{IS} = -0.82$ eV for Cu(111) and $E_{SR} = -3.62$ and $E_{IS} = -0.57$ eV for Cu(100)). The thick horizontal line indicates the Cu states degenerate with the adsorbate-localized resonance state. The thin horizontal line indicates the Fermi energy.

and, thus, occurs along the closest possible direction to the surface normal that is compatible with the Cu(111) band structure. This situation is reflected in Figure 26, where the electronic flux into the metal appears at a finite angle away from the surface normal. So, on Cu(111), the metal states that can be expected to participate the most actively in the RCT process are missing (see Figure 27). As a consequence, the one-electron RCT decay rate of the adsorbate-localized resonance is reduced by nearly 2 orders of magnitude as compared to the free-electron case. One can also notice a strong distortion of the Cs electronic cloud due to the interaction with the surface. The polarization of the Cs-localized state repels the electronic cloud away from the surface and further enhances

the band gap stabilization effect (see the discussion in ref 462).

In such a case where the one-electron-transfer process is quasi-blocked, the multielectron inelastic processes can also play a role in the decay of the population of the adsorbate-induced resonance. Both contributions have been computed using a parameter-free approach. The RCT part was computed using the WPP approach outlined in section 2.2.1, also allowing us to compute the wave function of the transient state. This wave function was then used in the many-body approach outlined in section 2.1 to get the multielectronic inelastic charge-transfer rate. This yields lifetimes of the excited states that are in good agreement with experiment; in particular, they reproduce the differences between Cu(111) and Cu(100) substrates as well as the differences between the various alkali adsorbates on a Cu(111) surface.^{84,143} Table 7 presents a summary of the theoretical results and their comparison with existing experimental data. It is noteworthy that, in agreement with experimental data, the lifetime of the alkali adsorbate-localized state increases along the Na, K, Rb, Cs sequence for the alkali/Cu(111) system. This is attributed to the difference between the various alkali atom polarizabilities, since the polarization of the resonance wave function away from the surface plays a crucial role in the band gap stabilization effect. Observe also that the RCT rate is much larger for the Cs/Cu(100) system than for the Cs/Cu(111) surface. Both surfaces possess a projected band gap in the direction of the surface normal (L-gap for Cu(111) and X-gap for Cu(100)). However, in the Cs/Cu(100) system, the adsorbate localized state lies closer to the bottom of the projected band gap (see Figure 27). Then, smaller $k_{||}$ continuum states are involved in the RCT, and the band gap stabilization effect is reduced.

The very long lifetime of the Cs-localized excited state in the Cs/Cu(111) system makes it a good intermediate for surface reactions. Indeed, it has been shown to mediate

Table 7. Decay Rates for the Alkali/Cu(111) and Alkali/Cu(100) Systems^a

	Na/Cu(111)	K/Cu(111)	Rb/Cu(111)	Cs/Cu(111)	Cs/Cu(100)
Theoretical Results (refs 84 and 143)					
E_0 (eV)	-2.17	-2.21	-2.17	-1.98	-1.46
Γ_{RCT} (meV)	70	16	10	7	112
$\Gamma_{\text{e-e}}$ (meV)	22	18	17	15	20
τ (fs)	7	19	24	30	5
Experimental Results					
τ (fs)	1.6 (300 K) [459]		25 (33 K) [459]	15 \pm 6 (300 K) [455, 456] 50 (33 K) [457, 459]	6 \pm 4 (300 K) [456]

^a The decay rates presented here have to be compared with a typical 900 meV value for a free-electron-like substrate (0.7 fs lifetime). E_0 is the energy with respect to the vacuum level, Γ_{RCT} is the one-electron decay rate, $\Gamma_{\text{e-e}}$ is the inelastic electron–electron decay, and $\tau = 1/(\Gamma_{\text{RCT}} + \Gamma_{\text{e-e}})$ is the level lifetime.

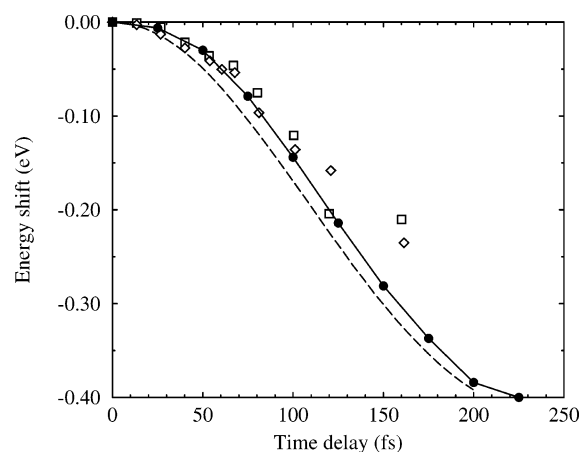


Figure 28. Energy shift of the position of the maximum of the energy spectrum of photoemitted electrons in a TR-2PPE experiment on the Cs/Cu(111) system. The energy shift (in eV) is presented as a function of the time delay (in fs) between the two laser pulses. Theoretical results from ref 144 (dashed line) and ref 146 (full lines with black dots) are compared to the experimental results from ref 458 (open squares and diamonds).

photodesorption of the alkali adsorbate.⁴⁵⁸ This desorption process corresponds to the well-known Menzel–Gomer–Redhead mechanism:^{463,464} the Cs adsorbate is initially at its equilibrium position as a positive ion; the incident photon transfers an electron from the substrate to the alkali, forming the resonant state; the interaction between this state and the surface is repulsive, and the alkali starts to move away from the surface. After a certain time, the excited state decays by electron transfer into the metal and if the energy that has already been transferred to the heavy particle motion is large enough, desorption occurs. The desorption motion induced by photoabsorption has been clearly evidenced by TR-2PPE:⁴⁵⁸ as the time delay between the two photons is increased, the energy of the intermediate state is changing, revealing the Cs desorption motion. Figure 28 shows the shift of the maximum of the photoemission spectrum as a function of the delay between the two photons.⁴⁵⁸ The long lifetime of the Cs* state allows for the monitoring of its evolution over more than 150 fs, during which the Cs* energy changes by around 0.3 eV. In the Cs/Cu(111) system, the efficiency of the photodesorption process is limited by the large mass of the desorbing particle. The photoinduced desorption motion has been studied theoretically using the same modeling as the one used to compute the Cs* excited-state lifetime. Two different studies have been performed. In the first one,¹⁴⁴ assuming a classical motion of the desorbing Cs, the electron evolution was followed with the WPP approach. This showed that the Cs* is evolving adiabatically as the atom desorbs.

In the second work,¹⁴⁶ the quantal motion of the desorbing particle was treated together with the explicit effect of the two laser pulses. These two approaches reproduced extremely satisfyingly the experimental observations from ref 458 (see Figure 28), thus fully confirming the scheme of the Cs* evolution.

The existence of the Cs* desorption motion brings in an interesting point, connected to the interpretation and analysis of TR-2PPE experiments. The usual analysis of TR-2PPE experiments^{241,455–458,465,466} involves the fit of the experimental data to a model based on Bloch optical equations.³⁷⁵ The transient excited state is then characterized by two times: the population decay time, T_1 , and the pure dephasing time, T_2^* (see section 6.1). In the usual Bloch optical equations approach, these two quantities do not change during the evolution probed by the TR-2PPE experiments, and this kind of modeling is well adapted to excited states whose characteristics do not evolve with time, such as, e.g., image states. However, such an approach cannot, a priori, be applied to situations where the electronic excitation triggers a reaction on the surface, such as, e.g., desorption,⁴⁵⁸ self-trapping,⁴ or solvation.⁴⁶⁷ Indeed, in that case, the excited state characteristics are expected to change along the reaction path. This problem clearly appears in the experimental results on the Cs/Cu(111) system as time-dependent photoemission signals that do not correspond to a Bloch optical equation modeling or as a lifetime of the excited state that depends on the experimental laser characteristics.⁴⁶⁸ This problem has been studied theoretically in the case of the Cs/Cu(111) system using a wave packet propagation approach.¹⁴⁶ It revealed a few effects: (i) a fast decay of the apparent signal is due to the variation of the excited state energy that brings it out of the experimental detection window, and (ii) a pure dephasing process appears as a direct consequence of the shift of the excited state energy. It also showed that the parameter-free model of the Cs/Cu(111) system is able to quantitatively reproduce the time dependence of the TR-2PPE signals and their variations with the laser characteristics.⁴⁶⁸

The effect of neighbors on the long-lived transient state energy and lifetime has also been investigated in the alkali/Cu(111) systems.^{141,377} The basic idea was to sum the potentials created around a given adsorbate by all the other adsorbates and average over a random distribution of adsorbates, in the same way as what has been discussed above for image states. In the alkali/Cu(111) system, summing up the long range dipolar potential is enough and allows us to get the effective potential created around one given adsorbate by all the others. This potential can be introduced in the WPP treatment, similarly to the case of a single adsorbate. These studies^{141,377} revealed that the long-

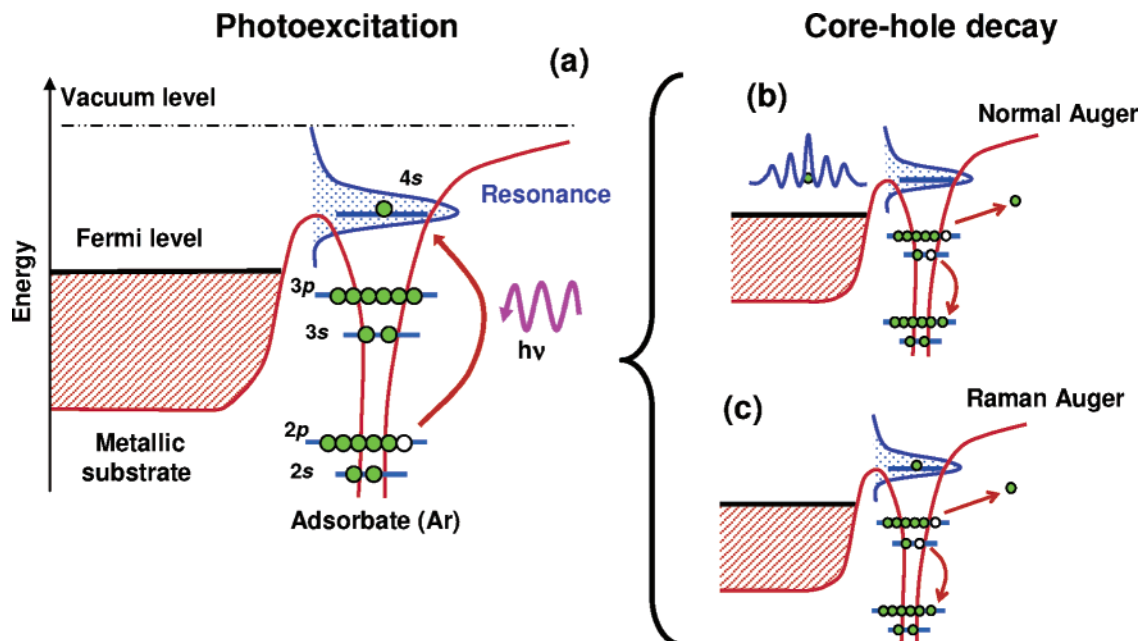


Figure 29. The so-called core-hole spectroscopy is based on the measurement of the intensity ratio of the two possible routes for the autoionization of a core-excited adsorbate in a metal surface. (a) The process is initiated by the excitation of a core electron into an unoccupied bound resonance. Then core-hole decay can occur either (b) once that electron has been transferred to the substrate (“normal Auger”) or (c) with the excited electron still localized in the resonance (“Auger resonant Raman”). Both channels can be distinguished, since their signals appear at different energies and show different behavior as a function of the initial photon energy (see the text).

lived state energy roughly varies such as $(\Delta\Phi)^{3/2}$ as a function of the adsorbate-induced work function change, $\Delta\Phi$, in agreement with experiment.^{317,455} A rather weak dependence of the quasi-stationary state lifetime on the adsorbate coverage has been computed, consistent with experimental observations.⁴⁵⁵ In this context, the effect of nonhomogeneous broadening (distribution of alkali adsorbate heights and disorder in the distribution of adsorbates on the surface) on the Na, Cs/Cu(111) excited states was found to be very large, dominating the natural width of the excited state.⁴⁶⁹

A few conclusions can be drawn from these detailed studies on the Cs/Cu(111) and alkali/Cu systems:

(i) It appears possible to have adsorbate systems with very long-lived excited states on metal surfaces, due to a projected band gap. However, not all systems with a projected band gap exhibit a long-lived state. For example, the $\text{CO}^-(2\pi^*)$ resonance of the CO molecule is very short-lived on a Cu(111) surface, as has been found experimentally^{470,471} and theoretically.^{462,472,473} A detailed analysis of several systems shows that the best case for a long-lived state is a neutral polarizable system, with a level not too low in the surface-projected band gap.⁴⁶²

(ii) A very long-lived excited state is likely to induce energy transfer between electronic and nuclear degrees of freedom, i.e., to induce a rearrangement process. For these very appealing systems, an explicit account for the evolution of the excited-state characteristics along the reaction path has to be included in the analysis of TR-2PPE signals in order to extract the proper characteristics of the system, i.e., the excited-state energy, lifetime, and coherence time.

6.5. Localized Excitons Formed by Inner-Shell Excitation in Surface Overlayers

Another kind of excited states localized on adsorbates can exist in the case of complete ordered layers. Consider, for example, the case of the core-excited $\text{Ar}^*(2p_{3/2}^{-1}4s)$ atom

inside an Ar layer on a metal surface. It is formed via X-ray absorption, with an inner 2p electron being excited to the 4s orbital. This excited state can decay by Auger relaxation of the 2p core hole, with the 4s electron as a spectator; this is the decay route of the free $\text{Ar}^*(2p_{3/2}^{-1}4s)$ state,^{474,475} and it is associated with a 6 fs lifetime. When adsorbed on a metal, another decay route appears: the 4s electron transfer into the metal. Because of the presence of the core-hole, this exciton is not mobile (i.e. remains localized around a given atomic center) on the time scale of the core-hole lifetime and, thus, it provides another example of a localized excitation on an adsorbate. Experimentally, such core-excited states have been much studied by synchrotron radiation experiments. Similar to the excited states discussed in the previous section, core-excited states can also induce various rearrangement processes at surfaces, and detailed studies have been devoted to the various ionic, neutral, and cluster desorption processes mediated by rare gas excitation in rare gas overlayers (see, e.g., a review in refs 476 and 477). In the context of the present review, we will stress two aspects: studies on the excited electron transfer into the metal and analysis of the effect of the neighbors in the adsorbed layers on the localized exciton.

The existence of two different channels for the autoionization of core-excited atoms adsorbed on metal surfaces is the basis of the so-called “core-hole clock” spectroscopy.^{478–486} These two decay routes are schematically illustrated in Figure 29. After the initial excitation (a) of a core electron into an unoccupied bound resonance, the Auger decay of the core hole can proceed (b) once the outer electron has been transferred into the substrate (“normal Auger” contribution) or (c) with this outer electron as a spectator (“Auger resonant Raman” contribution). These two decays lead to different characteristic energies of the Auger electrons, so that it is experimentally possible to measure the relative importance of the two contributions. Furthermore, the two processes can be distinguished due to their different behaviors with the

energy of the photon initially used for the excitation. In the case of the Auger resonant Raman channel, there is a linear relation between the kinetic energy of the electron emitted into the vacuum and the energy of the incident photon. This can be naively interpreted in terms of a *local* energy conservation, i.e., within the adsorbed atom. More precisely, in the Auger resonant Raman channel the coherence between the initial excitation process and the core-hole decay is preserved despite the presence of the substrate. On the contrary, for the normal Auger contribution, the kinetic energy of the Auger emitted electron is independent of the photon energy. This can be easily understood; once the outer electron has been transferred into the substrate, moving away from the adsorbate and suffering inelastic scattering processes in the metal, the memory of the initial photon energy (electron phase) is quickly lost. Therefore, the normal Auger decay channel can be interpreted as composed of two incoherent processes: (i) the core-hole excitation and subsequent charge-transfer into the substrate, followed by (ii) the core-hole decay of the cation left on the surface. Under the assumption that the decay time of the core hole (τ_{ch}) is not influenced by the adsorption, one can get the charge-transfer time (τ_{CT}) of the excited electron into the substrate from the ratio between resonant Raman (I_{R}) and normal (I_{N}) contributions. Defining the Raman fraction as $f = I_{\text{R}}/(I_{\text{R}} + I_{\text{N}})$, it can be easily shown that $\tau_{\text{CT}} \approx \tau_{\text{ch}} f / (1 - f)$. Taking into account the typical experimental uncertainties,⁴⁸⁷ this technique allows for the access of charge-transfer times in the range $0.1\tau_{\text{ch}} \leq \tau_{\text{CT}} \leq 10\tau_{\text{ch}}$. Typical values for τ_{ch} range from a few to 10 femtoseconds. Therefore, the core-hole clock spectroscopy provides a very efficient method for measuring fast charge transfer for core-excited adsorbates for which the Auger is the most efficient decay process. The sensitivity of the core-hole clock spectroscopy has been recently pushed to the atto-second range using Coster–Kronig decay channels.¹⁷⁴ In the Coster–Kronig transitions the initial and final holes belong to the same electronic shell (same principal quantum number, n). This translates into larger transition matrix elements and very fast decay times well below the femtosecond.

6.5.1. Charge Transfer Studies

Electron transfer between a core-excited atom and a metal substrate is expected to be rather similar to the one discussed in the previous section for lower energy excited states. Indeed, a core-excited atom has the structure of a compact ionic core with an outer excited electron around it. Very often, such excited states have been described using the so-called “Z+1” approximation, in which the core-excited state of the atom is compared to a low-lying state of the next atom in the periodic table. Within the “Z+1” approximation, one can expect an $\text{Ar}^*(2p_{3/2}^{-1}4s)$ atom to look like a $\text{K}(4s)$ atom (see, e.g., a discussion in refs 481 and 484). A few theoretical studies have been devoted to the adsorbate–substrate charge transfer in the case of core-excited atoms. In the first series of studies,¹⁴⁸ the $\text{Ar}^*(2p_{3/2}^{-1}4s)$ state has been studied within the WPP approach described in section 2.2.1. The electron interaction with the Ar^+ ionic core was described via a pseudopotential, and the effect of the Ar neighbors was described using the self-consistent microscopic treatment of ref 152. The results for Ar adsorbed on Cu surfaces were found to much resemble those for a K adsorbate, though they were not identical. In particular, while charge-transfer times are very fast on a free-electron metal (1.1 fs for a 1 ML of Ar coverage of the surface), they are much longer when the

4s orbital lies inside a surface-projected band gap. More precisely, the charge-transfer times are 12 fs for a 1 ML of Ar coverage on Cu(111) surfaces and 6.6 fs for a 1 ML of Ar coverage on Cu(100) surfaces.¹⁴⁸ This confirmed the validity of the criteria found for the observation of a band gap-induced reduction of the charge-transfer rate (see above and ref 462). It also stresses the fact that the presence of a core hole on the Ar adsorbate, i.e., the very large excitation energy of the state, does not qualitatively influence the dynamics of the outer electron. An experimental study using the core-hole clock method of the $\text{Ar}^*(2p_{3/2}^{-1}4s)/\text{Cu}(111)$ system⁴⁸⁸ yielded a charge-transfer time of 7 fs, also much larger than the one predicted for a free-electron system. Though the experimental time is not as large as the theoretical one,¹⁴⁸ it also confirms the charge-transfer blocking role of the surface-projected band gap. More recently, a joined experiment-theory study compared the $\text{Ar}^*(2p_{3/2}^{-1}4s)/\text{Cu}(111)$ and $\text{Ar}^*(2p_{3/2}^{-1}4s)/\text{Cu}(100)$ systems; the longer charge-transfer time on Cu(111) could be attributed to the higher energy position of the 4s orbital in the Cu(111) surface-projected band gap, that enhances the RCT-blocking effect of the projected band gap.⁴⁸⁹

One of the most complete sets of data has been accumulated for Ar on the close-packed Ru(0001) surface.^{482,487} The charge transfer dynamics in this system has been recently addressed using calculations of the surface Green function from *ab initio* density functional calculations¹⁸³ as described in section 2.2.2. The calculations are performed for symmetric slabs containing 9 or 11 metal layers plus a monolayer of Ar adsorbed on both the upper and bottom surfaces. Consistent with previous studies,⁴⁹¹ the most stable configuration of the Ar layer is found for the Ar atoms sitting directly on top of the Ru atoms on the surface. The calculations containing core-excited Ar^* are performed using supercells of different sizes along the lateral directions, thus corresponding to argon monolayers with different concentrations of $\text{Ar}^*(2p_{3/2}^{-1}4s)$ atoms. The cases studied correspond to the Ar_3Ar^* , Ar_8Ar^* , and $\text{Ar}_{15}\text{Ar}^*$ formula units. The *ab initio* pseudopotential⁴⁹² for Ar^* is constructed including a hole in the 2p shell and turns out to be quite similar to that of K. For an isolated Ar layer, the exciton associated with $\text{Ar}^*(2p_{3/2}^{-1}4s)$ can be easily calculated. Since the core hole effect is introduced in the pseudopotential, this is equivalent to a normal ground-state calculation. Unfortunately, this is not possible when the same layer is adsorbed on a metal slab. In such a situation, the ground state corresponds to the 4s electron being transferred to the lowest available level of the metal slab. Sánchez-Portal *et al.*¹⁸³ avoided this difficulty by performing constrained self-consistent calculations. In these calculations, one of the electrons is constrained to occupy a 4s atomic orbital linked to the $\text{Ar}^*(2p_{3/2}^{-1}4s)$ atom, while the rest of the electrons are allowed to freely accommodate the presence of such an excited adsorbate. With this procedure, the 4s exciton associated with the Ar^* atoms appears at ~ 4 eV above the Fermi energy, which compares well with the measured 3.4 eV.⁴⁸⁷ Combining the Hamiltonian obtained in the slab calculations with the Ru bulk Hamiltonian and recursive techniques, the surface Green function is calculated¹⁸³ (see section 2.2.2). For the experimental Ru–Ar distance (~ 3.5 Å), the calculated charge-transfer time for the 4s resonance is in the range of 1.9–2.5 fs (depending on the Ar^* concentration, see above), which is in quite good agreement with the experimental value of 1.5 fs.⁴⁸⁷ One of the most striking results of the calculations

is the very weak dependence of the charge transfer time on the height of the Ar monolayer above the Ru substrate. The charge transfer time only increases from 1.9–2.5 fs for a height of 3.5 Å to 3.14–4.11 fs for a 6 Å separation. The explanation of this fact relies once more on the electronic structure of the substrate. For energies higher than ~ 2 eV above the Fermi energy, the Ru(0001) surface presents a projected band gap around $\bar{\Gamma}$. Once in the gap region, the number of available states for propagation in bulk Ru increases as we move to lower energies, i.e., as we move closer to the band gap minimum. This situation is similar to that found for Cu(100) (see Figure 27). Thus, for a resonance inside the gap, we typically find that, the lower its energy position, the shorter its charge-transfer time. For the Ar/Ru(0001) system, increasing the Ru–Ar distance translates to a lower energy of the 4s level and, consequently, to an increment of the number of available final states for charge transfer. This effect partially compensates the smaller overlap between the 4s resonance and the states of the substrate, that tends to increase the charge transfer time, leaving a very weak dependence of the charge-transfer time on the Ru–Ar distance.

So far, we have restricted our discussion to the case of Ar on different metallic substrates. A recent joined experimental and theoretical study addressed a system exhibiting a much stronger substrate–adsorbate interaction, the $c(4 \times 2)\text{S}/\text{Ru}(0001)$ surface reconstruction.¹⁷⁴ The resonance studied in this case appears experimentally at 1.65 eV above the Fermi energy. In the density functional calculations of the ground state of this reconstruction (no core-excited S atoms), a corresponding very weakly dispersing and quite broad feature appears at ~ 2.0 eV (i.e. right below the projected band gap at $\bar{\Gamma}$). The reasonable agreement in the position of the level points to weak excitonic effects in this case, and therefore, the core hole was not included in the calculations. The nature of this resonance is quite different compared to the case of Ar/Ru(0001). While for weakly interacting Ar the resonance can be identified with the atomic 4s state, in the case of $c(4 \times 2)\text{S}/\text{Ru}(0001)$, the resonance (or resonances) can be pictured as composed of antibonding states coming from the hybridization of the 3p states of S with the neighboring Ru atoms. The corresponding bonding states, with a stronger S 3p character, can be found ~ 5 eV below the Fermi level. Assuming that an antibonding resonance appears in the same energy range for each of the three 3p states of sulfur, then the nature of the wave packet in which the electron is initially pumped will be strongly dependent on the excitation process. Since the electron is excited from a core state with *s* symmetry, it may be expected that, for linearly polarized light with an electric field **E**, the electron will be promoted to a state with maximum overlap with the linear combination $|P\rangle = E_x|3p_x\rangle + E_y|3p_y\rangle + E_z|3p_z\rangle$. The Green function projected onto $|P\rangle$, $G_{PP}^+(\omega)$, is then calculated. The survival amplitude $A(t)$ is obtained from $G_{PP}^+(\omega)$ in the energy range of interest. To do this, we make $\text{Re}[\tilde{A}(\omega)] = -\text{Im}[G_{PP}^+(\omega)]$ only in an interval of energies that extends from the Fermi level to 5 eV above it. Outside this energy window, $\text{Re}[\tilde{A}(\omega)]$ is made to smoothly become zero. $\text{Im}[\tilde{A}(\omega)]$ can be obtained from $\text{Re}[\tilde{A}(\omega)]$ using the well-known relations between the imaginary and the real parts of the Green functions.⁴⁹⁷ The charge-transfer time can be estimated by two methods: by fitting of $G_{PP}^+(\omega)$ with a Lorentzian or by directly estimating the time constant from the decay of $P(t) = |A(t)|^2$. Both methods produce similar

results, and indeed, a systematic variation of the time constant can be found for the decrease of the population of the initial wave packet with the polarization vector of the light. The results are shown in Figure 30. The shorter charge-transfer time (0.63 ± 0.15 fs) is found for the wave packet created with light polarized along the normal to the surface. This corresponds to the experimental geometry. The experimental value for the charge-transfer time is 0.32 ± 0.09 fs. Thus, both theory and experiment confirm that the charge-transfer time is well below the femtosecond range for this system. For different light polarization vectors, the theory predicts an increase of the charge-transfer time. This time is maximum (1.15 ± 0.15 fs) for polarizations parallel to the surface.

6.5.2. Effect of Ar Neighbors on the $\text{Ar}^*(2p_{3/2}^{-1}4s)$ State

The experimental and theoretical studies on core-excited Ar^* atoms discussed above were done using complete Ar layers adsorbed on metal surfaces, so that the Ar^* state was surrounded by a certain number of neighbors that influence the energy and the dynamics of the excited electron. Comparison between systems with different numbers of adsorbed layers reveals an interesting phenomenon: the charge-transfer time between Ar^* and the metal depends much on the position of the Ar^* atom in the layer or more precisely depends much on the number of Ar layers separating it from the metal. For $\text{Ar}^*(2p_{3/2}^{-1}4s)/\text{Cu}(111)$, the charge-transfer rate is increasing from 12 fs for a 1 ML layer to 260 fs (7700 fs) for Ar^* in the outer layer of a 2 ML (3 ML) coverage of the surface.¹⁴⁸ The strength of this effect is remarkable: the charge-transfer time is increasing by a factor 20–30 for each added monolayer. A similar effect has been observed using the core-hole clock method, on multilayered $\text{Ar}^*/\text{Xe}/\text{Ru}$ systems.^{482,487,490} These experiments also showed a drastic increase of the charge-transfer time when the electron has to tunnel through a rare gas layer. Such a low transmission efficiency of the rare gas Ar (or Xe) layer is attributed to its insulating properties: the 4s electron energy lies inside the Ar (or Xe) bulk band gap, and the 4s electron has to tunnel through the Ar layer in order to be transferred from Ar^* into the metal. The insulating property appears for a single Ar monolayer which already has a very low transmission efficiency. This effect has to be linked to the corresponding one observed for image states on rare gas layers on metal surfaces (see section 5.2). The image states are confined in the vacuum, out of the rare gas layer. Their decay involves inelastic interactions with bulk electrons; it also requires the transmission of the electron through the rare gas layer and exhibits the same insulating effect.^{150,152,291,345,493–495} One can notice that the electron transmission through an Ar layer in the $\text{Ar}^*(2p_{3/2}^{-1}4s)$ case¹⁴⁸ is weaker than that in the case of image states on Cu(100).^{150,152} This difference is attributed to the different energy positions of the excited state inside the Ar band gap that lead to different transmission efficiencies.

Ar neighbors located in the same layer as Ar^* or in outer layers were also found to influence the charge-transfer time, both experimentally and theoretically.^{148,487} This effect, much weaker than the transmission effect, has been attributed to the Ar neighbors perturbing the polarization of the outer electron and, through this, the stabilization effect of the projected band gap (see the discussion in ref 148). The effect of Ar neighbors on the energy of the $\text{Ar}^*(2p_{3/2}^{-1}4s)$ state has also been analyzed for Ar^* atoms in various environ-

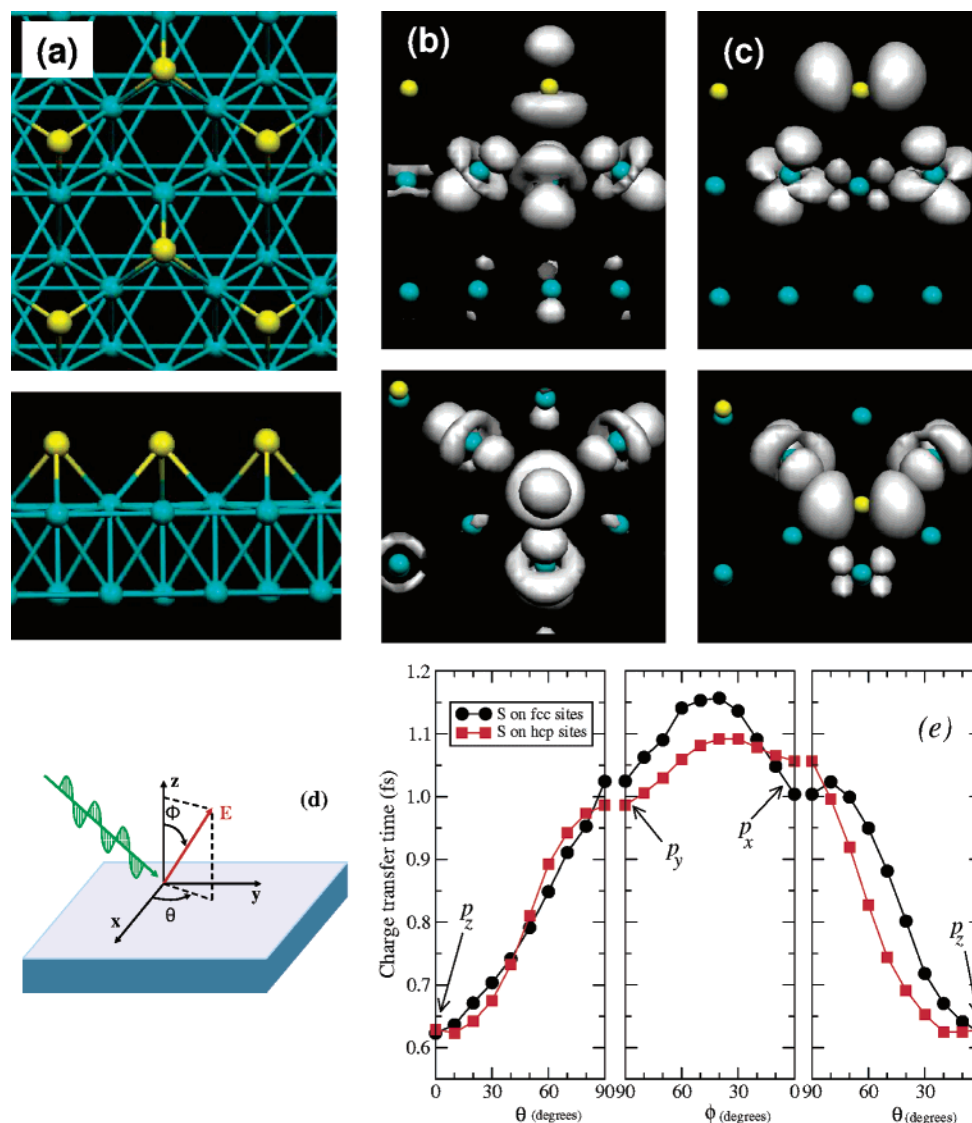


Figure 30. Theoretical charge transfer time for wave packets initially located at sulfur atoms on fcc and hcp hollow sites in the $c(4 \times 2)$ S/Ru(0001) surface. Panel (a) shows the structure of the surface (top and lateral views). Lighter (yellow) spheres represent the sulfur atoms in the surface; darker spheres correspond to the ruthenium atoms. The initial wave packets are constructed by projecting different linear combinations of the S 3p states onto the energy region corresponding to the resonance studied in ref 174. Panels (b) and (c) show the electron density associated with the initial wave packets corresponding respectively to the projection of p_z and p_x orbitals (top and lateral views are shown). The strong hybridization with the Ru atoms on the surface layer and the large dependence on the symmetry of the sulfur orbital contributions are evident. Experimentally, this should be reflected as a strong dependence of the core-hole spectroscopy measurements as a function of the polarization vector when using linearly polarized light (see the text). The x , y , and z coordinates shown in diagram (d) correspond to the crystallographic directions [100], [010], and [001]. The angles ϕ and θ define the orientation of the electric field vector of the radiation with respect to these axes. Panel (e) shows the charge transfer time as a function of the symmetry of the initial wave packet (i.e. the polarization of the electric field in the experiment). Circles and squares correspond respectively to sulfur atoms in fcc and hcp sites of the surface. The experimental geometry used in ref 174 corresponds to a polarization of the synchrotron light normal to the surface ($\phi = 0$).

ments.⁴⁹⁶ The insulating properties of Ar appear as a caging effect in which the 4s orbital is confined by its Ar neighbors, associated with the polarization of the surrounding Ar medium.

The analysis of the outer electron dynamics in core-excited systems showed that it follows the same general properties as those of excited states at much lower energy, with the presence of the core hole not influencing the outer electron dynamics. In addition, the localized character of these excitons inside complete layers make them an ideal playground to decipher the influence of neighboring atoms on the characteristics of an excited state (energy and lifetime), an important feature in the context of excited-state mediated reaction mechanisms at surfaces.

7. Summary and Outlook

Extensive theoretical study of electron and hole dynamics in bulk metals and at metal surfaces has been conducted since the middle of the 1990s. The developed models and first-principle calculations allowed one to study in detail the decay mechanisms of excited electrons (holes). In general, a good agreement with measurements by different spectroscopies has been obtained. However, despite great success achieved during the past decade in the study of electron and hole dynamics in bulk metals and at clean surfaces, as well as at surfaces with adatoms and adlayers, very much remains to be done in this very active research field. In particular, the decay mechanisms have been mostly explored in paramag-

netic and nonrelativistic (nonheavy) metals.^{74,219,226,237} In the future, one can expect more calculations for bulk ferromagnetics, for clean ferromagnetic metal surfaces, and for surfaces covered with magnetic adatoms and adlayers. In these systems, charge, spin, and phonon degrees of freedom are interrelated,^{27,29,498–500} thus giving rise to new decay mechanisms of excited electrons.^{23,25,42,81,279,498–500} The theoretical challenge for the future will be the extension of many-body calculations of quasiparticle dynamics to heavy metal and semimetal surfaces and ultrathin films. In these materials, a very strong spin–orbit splitting in surface bands^{266,501–512} can have drastic consequences for electron and hole dynamics in surface states. In particular, the splitting should influence the surface response function via the inclusion of all the spin-flip processes between the split surface bands with different spin directions. This splitting should also lead to different hole (electron) lifetimes in surface states compared to that for the nonsplit surface state. Of particular interest may be the study of laterally confined surface states. While they have been identified clearly, e.g., on noble metal surfaces,^{513–520} not much is known about their dynamic properties.^{149,151,406,521} More complex systems, such as quantum well states confined to a substrate surface, molecular-induced states on metal substrates, and spin-dependent quantum states on ferromagnetic surfaces, covered with molecules should be studied too. This extension should be accompanied by analysis of the role of different approximations used in the theory, for instance, the role of nonlinear effects in screening, the importance of vertex corrections in many-body calculations of the electron–electron contribution, and the role of short-range strong correlations in quasiparticle dynamics.

8. Acknowledgments

We gratefully acknowledge support by the Department of Education of the Government of the Basque Country, Spanish MCyT (Grant No. MAT2001-0946), and the European Community 6th Network of Excellence NANOQUANTA (NMP4-CT-2004-500198). The authors also want to thank M. Aeschlimann, F. Aryasetiawan, M. Bauer, R. Berndt, W. Berthold, G. Bihlmayer, S. Blügel, S. Crampin, A. Eiguren, Th. Fauster, S. Fölsch, B. Gumhalter, B. Hellsing, U. Höfer, Ph. Hofmann, A. K. Kazansky, Yu. M. Koroteev, J. Lagoute, A. Leonardo, D. C. Marinica, D. Menzel, T. Nagao, I. A. Nechaev, F. Olsson, M. Persson, H. Petek, J. M. Pitarke, M. Puska, F. Reinert, I. Yu. Sklyadneva, D. Teillet-Billy, M. Weinelt, and W. Wurth for enjoyable collaboration and discussions.

9. References

- (1) Dai, H. L.; Ho, W., Eds. *Laser Spectroscopy and Photochemistry on Metal Surfaces*; World Scientific: Singapore, 1995.
- (2) Ho, W. *J. Phys. Chem.* **1996**, *100*, 13050.
- (3) Bonn, M.; Funk, S.; Hess, C.; Denzler, D. N.; Stampfl, C.; Scheffler, M.; Wolf, M.; Ertl, G. *Science* **1999**, *285*, 1042.
- (4) Ge, N. H.; Wong, C. M.; Lingle, R. L., Jr.; McNeill, J. D.; Gaffney, K. J.; Harris, C. B. *Science* **1998**, *279*, 202.
- (5) White, J. D.; Chen, J.; Matsiev, D.; Auerbach, D. J.; Wodtke, A. M. *Nature* **2005**, *433*, 503.
- (6) Bartels, L.; Wang, F.; Möller, D.; Knoesel, E.; Heinz, T. F. *Science* **2004**, *305*, 648.
- (7) Nienhaus, H. *Surf. Sci. Rep.* **2002**, *45*, 1.
- (8) Haight, R. *Surf. Sci. Rep.* **1995**, *21*, 275.
- (9) Žutić, I.; Fabian, J.; Das Sarma, S. *Rev. Mod. Phys.* **2004**, *76*, 323.
- (10) Tamm, I. E. *Z. Phys.* **1932**, *76*, 849.
- (11) Tamm, I. E. *Phys. Z. Sowjetunion* **1932**, *1*, 733.
- (12) Shockley, W. *Phys. Rev.* **1939**, *56*, 317.
- (13) Gartland, P. O.; Slagsvold, B. *J. Phys. Rev. B* **1975**, *12*, 4047.
- (14) Kevan, S. D., Ed. *Angle-resolved Photoemission*; Studies in Surface Science and Catalysis, Vol. 74; Elsevier: Amsterdam, 1992.
- (15) Hüfner, S. *Photoelectron Spectroscopy—Principles and Applications*; Springer Series in Solid-State Science, Vol. 74; Springer: Berlin, 1995.
- (16) Cole, M. W. *Phys. Rev. B* **1970**, *2*, 4239.
- (17) Shikin, V. B. *Sov. Phys. JETP* **1970**, *31*, 936.
- (18) McRae, E. G. *Rev. Mod. Phys.* **1979**, *51*, 541.
- (19) Echenique, P. M.; Pendry, J. B. *J. Phys. C* **1978**, *11*, 2065.
- (20) Echenique, P. M.; Pendry, J. B. *Prog. Surf. Sci.* **1989**, *32*, 111.
- (21) Fauster, Th.; Steinmann, W. In *Photonic Probes of Surfaces*; Electromagnetic Waves: Recent Developments in Research, Vol. 2; Halevi, P., Ed.; North-Holland: Amsterdam, The Netherlands, 1995; Chapter 8, p 347.
- (22) Osgood, R. M., Jr.; Wang, S. *Solid State Phys.* **1997**, *51*, 1.
- (23) Allen, P. B. *Phys. Rev. B* **2001**, *63*, 214410.
- (24) Eiguren, A.; Hellsing, B.; Reinert, F.; Nicolay, G.; Chulkov, E. V.; Silkin, V. M.; Hüfner, S.; Echenique, P. M. *Phys. Rev. Lett.* **2002**, *88*, 066805.
- (25) Fedorov, A. V.; Valla, T.; Liu, F.; Johnson, P. D.; Weinert, M.; Allen, P. B. *Phys. Rev. B* **2002**, *65*, 212409.
- (26) Eiguren, A.; Hellsing, B.; Chulkov, E. V.; Echenique, P. M. *Phys. Rev. B* **2003**, *67*, 235423.
- (27) Bauer, A.; Mühligh, A.; Wegner, D.; Kaindl, G. *Phys. Rev. B* **2002**, *65*, 075421.
- (28) García-Lekue, A.; Pitarke, J. M.; Chulkov, E. V.; Liebsch, A.; Echenique, P. M. *Phys. Rev. Lett.* **2002**, *89*, 096401.
- (29) Rehbein, A.; Wegner, D.; Kaindl, G.; Bauer, A. *Phys. Rev. B* **2003**, *67*, 033403.
- (30) García-Lekue, A.; Pitarke, J. M.; Chulkov, E. V.; Liebsch, A.; Echenique, P. M. *Phys. Rev. B* **2003**, *68*, 045103.
- (31) Kröger, J. *Rep. Prog. Phys.* **2006**, *69*, 899.
- (32) Kliewer, J.; Berndt, R.; Chulkov, E. V.; Silkin, V. M.; Echenique, P. M.; Crampin, S. *Science* **2000**, *288*, 1399.
- (33) Echenique, P. M.; Flores, F.; Sols, F. *Phys. Rev. Lett.* **1985**, *55*, 2348.
- (34) Berthold, W.; Höfer, U.; Feulner, P.; Chulkov, E. V.; Silkin, V. M.; Echenique, P. M. *Phys. Rev. Lett.* **2002**, *88*, 056805.
- (35) Chulkov, E. V.; Leonardo, A.; Nechaev, I. A.; Silkin, V. M. *Surf. Sci.*, in press.
- (36) Matzdorf, R. *Surf. Sci. Rep.* **1998**, *30*, 153.
- (37) Kirkegaard, C.; Kim, T. K.; Hofmann, Ph. *New J. Phys.* **2005**, *7*, 99.
- (38) Reinert, F.; Hüfner, S. *New J. Phys.* **2005**, *7*, 97.
- (39) Dose, V. *Surf. Sci. Rep.* **1985**, *5*, 337.
- (40) Himpsel, F. J. *Comments Condens. Matter Phys.* **1986**, *12*, 199.
- (41) Smith, N. V. *Rep. Prog. Phys.* **1988**, *51*, 1227.
- (42) Donath, M. *Surf. Sci. Rep.* **1994**, *20*, 251.
- (43) Giesen, K.; Hage, F.; Himpsel, F. J.; Riess, H. J.; Steinmann, W. *Phys. Rev. Lett.* **1985**, *55*, 300.
- (44) Knoesel, E.; Hotzel, A.; Wolf, M. *J. Electron Spectrosc. Related Phenom.* **1998**, *88–91*, 577.
- (45) Schoenlein, R. W.; Fujimoto, J. G.; Eesley, G. L.; Capehart, T. W. *Phys. Rev. Lett.* **1988**, *61*, 2596.
- (46) Höfer, U.; Shumay, I. L.; Reuss, Ch.; Thomann, U.; Wallauer, W.; Fauster, Th. *Science* **1997**, *277*, 1480.
- (47) Petek, H.; Ogawa, S. *Annu. Rev. Phys. Chem.* **2002**, *53*, 507.
- (48) Bovensiepen, U. *Prog. Surf. Sci.* **2005**, *78*, 87.
- (49) Güdde, J.; Höfer, U. *Prog. Surf. Sci.* **2005**, *80*, 49.
- (50) Fauster, Th. *Surf. Sci.* **2002**, *507–510*, 256.
- (51) Weinelt, M. *J. Phys.: Condens. Matter* **2002**, *14*, R1099.
- (52) Binnig, G.; Rohrer, H. *Rev. Mod. Phys.* **1987**, *59*, 615.
- (53) Strosio, J. A.; Kaiser, W. J., Eds. *Scanning Tunneling Microscopy*; Academic Press: San Diego, CA, 1993.
- (54) Güntherodt, H.-J.; Wiesendanger, R., Eds. *Scanning Tunneling Microscopy*; Springer: Berlin, 1994–1996.
- (55) Li, J.; Schneider, W. D.; Berndt, R.; Crampin, S. *Phys. Rev. Lett.* **1998**, *80*, 3332.
- (56) Wahl, P.; Schneider, M. A.; Diekhöner, L.; Vogelgesang, R.; Kern, K. *Phys. Rev. Lett.* **2003**, *91*, 106802.
- (57) Pivetta, M.; Patthey, F.; Stengel, M.; Baldereschi, A.; Schneider, W.-D. *Phys. Rev. B* **2005**, *72*, 115404.
- (58) Kröger, J.; Limot, L.; Jensen, H.; Berndt, R.; Crampin, S.; Pehlke, E. *Prog. Surf. Sci.* **2005**, *80*, 26.
- (59) Abrikosov, A. A.; Gorkov, L. R.; Dzyaloshinski, I. E. *Methods of Quantum Field Theory in Statistical Physics*; Prentice-Hall: Englewood Cliffs, NY, 1963.
- (60) Mahan, G. D. *Many-particle physics*; Plenum Press: New York, 1990.
- (61) Inkson, J. C. *Many-body theory of solids*; Plenum Press: New York, 1984.
- (62) Fetter, A. L.; Walecka, J. D. *Quantum theory of many-particle systems*; McGraw-Hill: New York, 1971.
- (63) Hedin, L.; Lundqvist, S. *Solid State Phys.* **1969**, *23*, 1.
- (64) Aryasetiawan, F.; Gunnarsson, O. *Rep. Prog. Phys.* **1998**, *61*, 237.

- (65) Echenique, P. M.; Pitarke, J. M.; Chulkov, E. V.; Rubio, A. *Chem. Phys.* **2000**, 251, 1.
- (66) Rohlfing, M.; Louie, S. G. *Phys. Rev. B* **2000**, 62, 4927.
- (67) Wang, N.-P.; Rohlfing, M.; Krüger, P.; Pollmann, J. *Phys. Rev. B* **2005**, 71, 045407.
- (68) Quinn, J. J.; Ferrell, R. A. *Phys. Rev.* **1958**, 112, 812.
- (69) Smith, N. V. *Comments Condens. Matter Phys.* **1992**, 15, 263.
- (70) McDougall, B. A.; Balasubramanian, T.; Jensen, E. *Phys. Rev. B* **1995**, 51, 13891.
- (71) Chulkov, E. V.; Sarria, I.; Silkin, V. M.; Pitarke, J. M.; Echenique, P. M. *Phys. Rev. Lett.* **1998**, 80, 4947.
- (72) Osmá, J.; Sarria, I.; Chulkov, E. V.; Pitarke, J. M.; Echenique, P. M. *Phys. Rev. B* **1999**, 59, 10591.
- (73) Hedin, L. *Phys. Rev.* **1965**, 139, A796.
- (74) Echenique, P. M.; Berndt, R.; Chulkov, E. V.; Fauster, Th.; Goldmann, A.; Höfer, U. *Surf. Sci. Rep.* **2004**, 52, 219.
- (75) Chulkov, E. V.; Silkin, V. M.; Machado, M. *Surf. Sci.* **2001**, 482–485, 693.
- (76) Echenique, P. M.; Pitarke, J. M.; Chulkov, E. V.; Silkin, V. M. *J. Electron Spectrosc. Related Phenom.* **2002**, 126, 163.
- (77) Pitarke, J. M.; Zhukov, V. P.; Keyling, R.; Chulkov, E. V.; Echenique, P. M. *Chem. Phys. Chem.* **2004**, 5, 1284.
- (78) López-Bastidas, C.; Maytorena, J. A.; Liebsch, A. *Phys. Rev. B* **2002**, 65, 035417.
- (79) Springer, M.; Aryasetiawan, F.; Karlsson, K. *Phys. Rev. Lett.* **1998**, 80, 2389.
- (80) Aryasetiawan, F. In *Strong Coulomb Correlations in Electronic Structure Calculations*; Anisimov, V. I., Ed.; Gordon and Breach: Singapore, 2001.
- (81) Zhukov, V. P.; Chulkov, E. V.; Echenique, P. M. *Phys. Rev. Lett.* **2004**, 93, 096401.
- (82) Zhukov, V. P.; Chulkov, E. V.; Echenique, P. M. *Phys. Rev. B* **2005**, 72, 155109.
- (83) Borisov, A. G.; Kazansky, A. K.; Gauyacq, J. P. *Phys. Rev. B* **1999**, 59, 10935.
- (84) Borisov, A. G.; Gauyacq, J. P.; Chulkov, E. V.; Silkin, V. M.; Echenique, P. M. *Phys. Rev. B* **2002**, 65, 235434.
- (85) Corriol, C.; Silkin, V. M.; Sánchez-Portal, D.; Arnau, A.; Chulkov, E. V.; Echenique, P. M.; von Hofe, T.; Kliewer, J.; Kröger, J.; Berndt, B. *Phys. Rev. Lett.* **2005**, 95, 176802.
- (86) Eliashberg, G. M. *Zh. Eksp. Teor. Fiz.* **1960**, 38, 966 [*Sov. Phys. JETP* **1960**, 11, 696].
- (87) Eliashberg, G. M. *Zh. Eksp. Teor. Fiz.* **1962**, 43, 1005 [*Sov. Phys. JETP* **1962**, 16, 780].
- (88) Grimvall, G. In *The Electron–Phonon Interaction in Metals, Selected Topics in Solid State Physics*; Wohlfarth, E., Ed.; North-Holland: New York, 1981.
- (89) Gumhalter, B.; Petek, H. *Surf. Sci.* **2000**, 445, 195.
- (90) Gumhalter, B. *Surf. Sci.* **2002**, 518, 81.
- (91) Gumhalter, B. *Phys. Rev. B* **2005**, 72, 165406.
- (92) Sakaue, M.; Munakata, T.; Kasai, H.; Okiji, A. *Phys. Rev. B* **2002**, 66, 094302.
- (93) Sakaue, M.; Munakata, T.; Kasai, H.; Okiji, A. *Phys. Rev. B* **2003**, 68, 205421.
- (94) Sakaue, M. *J. Phys.: Condens. Matter* **2005**, 17, S245.
- (95) Nagy, I.; Alducin, M.; Juaristi, J. I.; Echenique, P. M. *Phys. Rev. B* **2001**, 64, 075101.
- (96) Nagy, I.; Alducin, M.; Echenique, P. M. *Phys. Rev. B* **2002**, 65, 235102.
- (97) Alducin, M.; Juaristi, J. I.; Nagy, I.; Echenique, P. M. *J. Phys.: Condens. Matter* **2002**, 14, 2647.
- (98) Juaristi, J. I.; Alducin, M.; Nagy, I. *J. Phys.: Condens. Matter* **2003**, 15, 7859.
- (99) Alducin, M.; Juaristi, J. I.; Nagy, I. *J. Electron Spectrosc. Related Phenom.* **2003**, 129, 117.
- (100) Knorren, R.; Bennemann, K. H.; Burgermeister, R.; Aeschlimann, M. *Phys. Rev. B* **2000**, 61, 9427.
- (101) Knorren, R.; Bouzerar, G.; Bennemann, K. H. *Phys. Rev. B* **2001**, 63, 094306.
- (102) Knorren, R.; Bouzerar, G.; Bennemann, K. H. *J. Phys.: Condens. Matter* **2002**, 14, R739.
- (103) Nechaev, I. A.; Chulkov, E. V. *Phys. Rev. B* **2005**, 71, 115104.
- (104) Nechaev, I. A.; Chulkov, E. V. *Phys. Rev. B* **2006**, 73, 165112.
- (105) Mahan, G. D. *Comments Condens. Matter Phys.* **1994**, 16, 333.
- (106) Karlsson, K.; Aryasetiawan, F. *Phys. Rev. B* **2000**, 62, 3006.
- (107) Kroes, G.-J. *Prog. Surf. Sci.* **1999**, 60, 1.
- (108) Kroes, G.-J.; Somers, M. F. *J. Theor. Comput. Chem.* **2005**, 4, 493.
- (109) Kroes, G.-J.; Gross, A.; Baerends, E. J.; Scheffler, M.; McCormack, D. A. *Acc. Chem. Res.* **2002**, 35, 193.
- (110) Bach, C.; Klüner, T.; Gross, A. *Chem. Phys. Lett.* **2003**, 376, 424.
- (111) Gross, A. *Surf. Sci. Rep.* **1998**, 32, 291.
- (112) Koch, C. P.; Klüner, T.; Freund, H.-J.; Kosloff, R. *J. Chem. Phys.* **2003**, 119, 1750.
- (113) Koch, C. P.; Klüner, T.; Freund, H.-J.; Kosloff, R. *Phys. Rev. Lett.* **2003**, 90, 117601.
- (114) Jorgensen, S.; Dubnikova, F.; Kosloff, R.; Zeiri, Y.; Lilach, Y.; Asscher, M. *J. Phys. Chem. B* **2004**, 108, 14056.
- (115) Lemoine, D.; Quattrucci, J. G.; Jackson, B. *Phys. Rev. Lett.* **2002**, 89, 268302.
- (116) Sha, X. W.; Jackson, B.; Lemoine, D.; Lepetit, B. *J. Chem. Phys.* **2005**, 122, 014709.
- (117) Morisset, S.; Aguilon, F.; Sizun, M.; Sidis, V. *J. Phys. Chem. A* **2004**, 108, 8571.
- (118) Saalfrank, P. *Curr. Opin. Solid State Mater. Sci.* **2004**, 8, 334.
- (119) Harris, S. M.; Holloway, S.; Darling, G. R. *J. Chem. Phys.* **1995**, 102, 8235.
- (120) Klamroth, T.; Kröner, D.; Saalfrank, P. *Phys. Rev. B* **2005**, 72, 205407.
- (121) Klamroth, T.; Saalfrank, P.; Höfer, U. *Phys. Rev. B* **2001**, 64, 035420.
- (122) Varsano, D.; Marques, M. A. L.; Rubio, A. *Comput. Mater. Sci.* **2004**, 30, 110.
- (123) Lindstrom, C. D.; Quinn, D.; Zhu, X.-Y. *J. Chem. Phys.* **2005**, 122, 124714.
- (124) Wall, M. R.; Neuhauser, D. *J. Chem. Phys.* **1995**, 102, 8011.
- (125) Mandelshtam, V. A.; Taylor, H. S. *Phys. Rev. Lett.* **1997**, 78, 3274.
- (126) Gauyacq, J. P.; Borisov, A. G.; Kazansky, A. K. *Appl. Phys. A: Mater. Sci. Process.* **2004**, 78, 141.
- (127) Tersoff, J.; Hamann, D. R. *Phys. Rev. B* **1985**, 31, 805.
- (128) *Numerical Grid Methods and Their Applications to the Schrödinger equation*; NATO ASI Series, Series C: Mathematical and Physical Sciences; Cerjan, C., Ed.; Kluwer Academic: Dordrecht, Germany, 1993; Vol. 412.
- (129) Lill, J. V.; Parker, G. A.; Light, J. C. *Chem. Phys. Lett.* **1982**, 89, 483.
- (130) Light, J. C. In *Time Dependent Quantum Molecular Dynamics*; NATO ASI Series, Series B: Physics; Broeckhove, J., Lathouwers, L., Eds.; Plenum: New York, 1992; Vol. 299, p 185.
- (131) Kosloff, D.; Kosloff, R. *J. Comput. Phys.* **1983**, 52, 35.
- (132) Littlejohn, R. G.; Cargo, M.; Carrington, T., Jr.; Mitchell, K. A.; Poirier, B. *J. Chem. Phys.* **2002**, 116, 8691.
- (133) Kosloff, R. *J. Phys. Chem.* **1988**, 92, 2087.
- (134) Van Hove, M. A.; Weinberg, W. H.; Chan, C. M. *Low Energy Electron Diffraction*; Springer-Verlag: Berlin, 1986.
- (135) Feit, M. D.; Fleck, J. A., Jr.; Steiger, A. *J. Comput. Phys.* **1982**, 47, 412.
- (136) Park, T. J.; Light, J. C. *J. Chem. Phys.* **1986**, 85, 5870.
- (137) See the following review paper: Leforestier, C.; Bisseling, R. H.; Cerjan, C.; Feit, M. D.; Friesner, R.; Guldberg, A.; Hammerich, A.; Jolicard, G.; Karlein, W.; Meyer, H.-D.; Lipkin, N.; Roncero, O.; Kosloff, R. *J. Comput. Phys.* **1991**, 94, 59 and references there in.
- (138) Neuhauser, D.; Baer, M. *J. Chem. Phys.* **1989**, 91, 4651.
- (139) Seideman, T.; Miller, W. H. *J. Chem. Phys.* **1992**, 97, 2499.
- (140) Jolicard, G.; Leforestier, C.; Austin, E. J. *J. Chem. Phys.* **1988**, 88, 1026.
- (141) Borisov, A. G.; Kazansky, A. K.; Gauyacq, J. P. *Surf. Sci.* **1999**, 430, 165.
- (142) Olsson, F. E.; Borisov, A. G.; Gauyacq, J. P. *Surf. Sci.* **2006**, 600, 2184.
- (143) Borisov, A. G.; Gauyacq, J. P.; Kazansky, A. K.; Chulkov, E. V.; Silkin, V. M.; Echenique, P. M. *Phys. Rev. Lett.* **2001**, 86, 488.
- (144) Borisov, A. G.; Kazansky, A. K.; Gauyacq, J. P. *Phys. Rev. B* **2001**, 64, 201105.
- (145) Kazansky, A. K.; Borisov, A. G.; Gauyacq, J. P. *Surf. Sci.* **2005**, 577, 47.
- (146) Gauyacq, J. P.; Kazansky, A. K. *Phys. Rev. B* **2005**, 72, 045418.
- (147) Borisov, A. G.; Kazansky, A. K.; Gauyacq, J. P. *Phys. Rev. B* **2002**, 65, 205414.
- (148) Gauyacq, J. P.; Borisov, A. G. *Phys. Rev. B* **2004**, 69, 235408.
- (149) Olsson, F. E.; Borisov, A. G.; Persson, M.; Lorente, N.; Kazansky, A. K.; Gauyacq, J. P. *Phys. Rev. B* **2004**, 70, 205417.
- (150) Marinica, D. C.; Ramseyer, C.; Borisov, A. G.; Teillet-Billy, D.; Gauyacq, J. P.; Berthold, W.; Feulner, P.; Höfer, U. *Phys. Rev. Lett.* **2002**, 89, 046802.
- (151) Olsson, F. E.; Persson, M.; Borisov, A. G.; Gauyacq, J. P.; Lagoute, J.; Fölsch, S. *Phys. Rev. Lett.* **2004**, 93, 206803.
- (152) Marinica, D. C.; Ramseyer, C.; Borisov, A. G.; Teillet-Billy, D.; Gauyacq, J. P. *Surf. Sci.* **2003**, 540, 457.
- (153) Borisov, A. G.; Gauyacq, J. P.; Kazansky, A. K. *Surf. Sci.* **2002**, 505, 260.
- (154) Borisov, A. G.; Kazansky, A. K.; Gauyacq, J. P. *Surf. Sci.* **2003**, 526, 72.
- (155) Borisov, A. G.; Kazansky, A. K.; Gauyacq, J. P. *Surf. Sci.* **2003**, 540, 407.
- (156) Jennings, P. J.; Jones, R. O.; Weinert, M. *Phys. Rev. B* **1988**, 37, 6113.

- (157) Chulkov, E. V.; Silkin, V. M.; Echenique, P. M. *Surf. Sci.* **1999**, 437, 330.
- (158) Taylor, J. R. *Scattering Theory: The Quantum Theory of Nonrelativistic Collisions*; Krieger: Malabar, FL, 1983.
- (159) Press, W. H.; Tenkolsky, S. A.; Vetterling, W. T.; Flannery, B. P. *Numerical Recipes in FORTRAN*; Cambridge University Press: Cambridge, U.K., 1992.
- (160) Borisov, A. G.; Gauyacq, J. P.; Shabanov, S. V. *Surf. Sci.* **2001**, 487, 243.
- (161) Lanczos, C. *J. Res. Natl. Bur. Stand.* **1950**, 45, 255.
- (162) Tal-Ezer, H.; Kosloff, R. *J. Chem. Phys.* **1984**, 81, 3967.
- (163) Arnoldi, W. E. *Q. Appl. Math.* **1951**, 9, 17.
- (164) Borisov, A. G.; Shabanov, S. V. *J. Comput. Phys.* **2005**, 209, 643.
- (165) Mandelshtam, V. A.; Taylor, H. S. *J. Chem. Phys.* **1995**, 103, 2903.
- (166) Huang, Y.; Zhu, W.; Kouri, D. J.; Hoffman, D. K. *Chem. Phys. Lett.* **1993**, 206, 96; 213, 209(E).
- (167) Huang, Y.; Kouri, D. J.; Hoffman, D. K. *J. Chem. Phys.* **1994**, 101, 10493.
- (168) Pollard, W. T.; Friesner, R. A. *J. Chem. Phys.* **1994**, 100, 5054.
- (169) Huisinga, W.; Pesce, L.; Kosloff, R.; Saalfrank, P. *J. Chem. Phys.* **1999**, 110, 5538.
- (170) Sjakste, J.; Borisov, A. G.; Gauyacq, J. P.; Kazansky, A. K. *J. Phys. B: At. Mol. Opt. Phys.* **2004**, 37, 1593.
- (171) Marston, C. C.; Balint-Kurti, G. G. *J. Chem. Phys.* **1989**, 91, 3571.
- (172) Gütde, J.; Berthold, W.; Höfer, U. *Chem. Rev.* **2006**, 106, 4261–4280.
- (173) Brivio, G. P.; Trioni, M. I. *Rev. Mod. Phys.* **1999**, 71, 231.
- (174) Föhlisch, A.; Feulner, P.; Hennies, F.; Fink, A.; Menzel, D.; Sánchez-Portal, D.; Echenique, P. M.; Wurth, W. *Nature* **2005**, 436, 373.
- (175) Sánchez-Portal, D.; Ordejón, P.; Artacho, E.; Soler, J. M. *Int. J. Quantum Chem.* **1997**, 65, 453.
- (176) Soler, J. M.; Artacho, E.; Gale, J. D.; García, A.; Junquera, J.; Ordejón, P.; Sánchez-Portal, D. *J. Phys.: Condens. Matter* **2002**, 14, 2745.
- (177) Junquera, J.; Paz, O.; Sánchez-Portal, D.; Artacho, E. *Phys. Rev. B* **2001**, 64, 235111.
- (178) Falicov, L. M.; Yndurain, F. *J. Phys. C: Solid State Phys.* **1975**, 8, 147.
- (179) Mele, E. J.; Joannopoulos, J. D. *Phys. Rev. B* **1978**, 17, 1816.
- (180) Lee, D. H.; Joannopoulos, J. D. *Phys. Rev. B* **1981**, 23, 4997.
- (181) López-Sancho, M. P.; López-Sancho, J. M.; Rubio, J. *J. Phys. F: Met. Phys.* **1984**, 14, 1205; **1985**, 15, 851.
- (182) Artacho, E.; Ynduráin, F. *Phys. Rev. B* **1991**, 44, 6169.
- (183) Sánchez-Portal, D.; Menzel, D.; Echenique, P. M. Submitted.
- (184) *TRANSFER MATRIX, GREEN FUNCTION AND RELATED TECHNIQUES*; García-Moliner, F., Pérez Alvarez, R., Eds.; Universidad Jaume I. Servicio de Comunicación y Publicaciones: Castellon de la Plana, 2004; ISBN 84-8021-472-4.
- (185) Hellsing, B.; Eiguren, A.; Chulkov, E. V. *J. Phys.: Condens. Matter* **2002**, 14, 5959.
- (186) LaShell, S.; Jensen, E.; Balasubramanian, T. *Phys. Rev. B* **2000**, 61, 2371.
- (187) Hofmann, Ph.; Cai, Y. Q.; Grüttter, Ch.; Bilgram, J. H. *Phys. Rev. Lett.* **1998**, 81, 1670.
- (188) Tang, S.-J.; Ismail; Sprunger, P. T.; Plummer, E. W. *Phys. Rev. B* **2002**, 65, 235428.
- (189) Gayone, J. E.; Hofmann, S. V.; Li, Z.; Hofmann, Ph. *Phys. Rev. Lett.* **2003**, 91, 127601.
- (190) Søndergaard, Ch.; Schultz, Ch.; Agergaard, S.; Hoffmann, S. V.; Li, Z.; Hofmann, Ph.; Li, H.; Grüttter, Ch.; Bilgram, J. H. *Phys. Rev. B* **2003**, 67, 165422.
- (191) Paggel, J. J.; Luh, D.-A.; Miller, T.; Chiang, T.-C. *Phys. Rev. Lett.* **2004**, 92, 186803.
- (192) Sklyadneva, I. Yu.; Rusina, G. G.; Chulkov, E. V. *Surf. Sci.* **1998**, 416, 17.
- (193) Sklyadneva, I. Yu.; Rusina, G. G.; Chulkov, E. V. *Phys. Rev. B* **2002**, 65, 235419.
- (194) Zein, N. E. *Fiz. Tverd. Tela* **1984**, 26, 3028 [*Sov. Phys. Solid State* **1984**, 26, 1825].
- (195) Baroni, S.; de Gironcoli, S.; Dal Corso, A. *Rev. Mod. Phys.* **2001**, 73, 515.
- (196) Heid, R.; Bohnen, K.-P. *Phys. Rep.* **2003**, 387, 151.
- (197) Chulkov, E. V.; Silkin, V. M.; Echenique, P. M. *Surf. Sci.* **1997**, 391, L1217.
- (198) Matzdorf, R.; Meister, G.; Goldmann, A. *Phys. Rev. B* **1996**, 54, 14807.
- (199) Balasubramanian, T.; Jensen, E.; Wu, X. L.; Hulbert, S. L. *Phys. Rev. B* **1998**, 57, R6866.
- (200) Valla, T.; Fedorov, A. V.; Johnson, P. D.; Hulbert, S. L. *Phys. Rev. Lett.* **1999**, 83, 2085.
- (201) Silkin, V. M.; Balasubramanian, T.; Chulkov, E. V.; Rubio, A.; Echenique, P. M. *Phys. Rev. B* **2001**, 64, 085334.
- (202) Balasubramanian, T.; Johansson, L. I.; Glans, P.-A.; Virojanadara, C.; Silkin, V. M.; Chulkov, E. V.; Echenique, P. M. *Phys. Rev. B* **2001**, 64, 205401.
- (203) Kim, T. K.; Sørensen, T. S.; Wolfring, E.; Li, H.; Chulkov, E. V.; Hofmann, Ph. *Phys. Rev. B* **2005**, 72, 075422.
- (204) Kralj, M.; Siber, A.; Pervan, P.; Milun, M.; Valla, T.; Johnson, P. D.; Woodruff, D. P. *Phys. Rev. B* **2001**, 64, 085411.
- (205) Liebsch, A. *Electronic Excitations at Metal Surfaces*; Plenum Press: New York, 1997.
- (206) Persson, B. N. J.; Zaremba, E. *Phys. Rev. B* **1985**, 31, 1863.
- (207) Runge, E.; Gross, E. K. U. *Phys. Rev. Lett.* **1984**, 52, 997.
- (208) Ritchie, R. H. *Phys. Rev.* **1957**, 106, 874.
- (209) Schaich, W. L.; Dobson, J. F. *Phys. Rev. B* **1994**, 49, 14700.
- (210) Silkin, V. M.; Chulkov, E. V.; Echenique, P. M. *Phys. Rev. Lett.* **2004**, 93, 176801.
- (211) Silkin, V. M.; Chulkov, E. V. *Vacuum* **2006**, 81, 186.
- (212) Eguiluz, A. G. *Phys. Rev. Lett.* **1983**, 51, 1907.
- (213) Silkin, V. M.; Pitarke, J. M.; Chulkov, E. V.; Echenique, P. M. *Phys. Rev. B* **2005**, 72, 115435.
- (214) Rocca, M. *Surf. Sci. Rep.* **1995**, 22, 1.
- (215) Lindhard, J. *Dan. Mater. Fys. Medd.* **1954**, 28, No. 8.
- (216) Ritchie, R. H. *Phys. Rev. B* **1959**, 114, 644.
- (217) Schöne, W.-D.; Keyling, R.; Bandić, M.; Ekardt, W. *Phys. Rev. B* **1999**, 60, 8616.
- (218) Campillo, I.; Pitarke, J. M.; Rubio, A.; Zarate, E.; Echenique, P. M. *Phys. Rev. Lett.* **1999**, 83, 2230.
- (219) Campillo, I.; Silkin, V. M.; Pitarke, J. M.; Chulkov, E. V.; Rubio, A.; Echenique, P. M. *Phys. Rev. B* **2000**, 61, 13484.
- (220) Zhukov, V. P.; Chulkov, E. V. *J. Phys.: Condens. Matter* **2002**, 14, 1937.
- (221) Ladstädter, F.; Hohenester, U.; Puschnig, P.; Ambrosch-Draxl, C. *Phys. Rev. B* **2004**, 70, 235125.
- (222) Silkin, V. M.; Chulkov, E. V.; Echenique, P. M. *Phys. Rev. B* **2003**, 68, 205106.
- (223) Sklyadneva, I. Yu.; Chulkov, E. V.; Schöne, W. D.; Silkin, V. M.; Keyling, R.; Echenique, P. M. *Phys. Rev. B* **2005**, 71, 174302.
- (224) Dolado, J. S.; Silkin, V. M.; Cazalilla, M. A.; Rubio, A.; Echenique, P. M. *Phys. Rev. B* **2001**, 64, 195128.
- (225) Papaconstantopoulos, D. A. *The Band Structure of Elemental Solids*; Plenum Press: New York, 1986.
- (226) Zhukov, V. P.; Aryasetiawan, F.; Chulkov, E. V.; de Gurtubay, I. G.; Echenique, P. M. *Phys. Rev. B* **2001**, 64, 195122.
- (227) Campillo, I.; Rubio, A.; Pitarke, J. M.; Goldmann, A.; Echenique, P. M. *Phys. Rev. Lett.* **2000**, 85, 3241.
- (228) Marini, A.; Del Sole, R.; Rubio, A.; Onida, G. *Phys. Rev. B* **2002**, 66, 161104(R).
- (229) Zhukov, V. P.; Chulkov, E. V.; Echenique, P. M. *Phys. Rev. B* **2003**, 68, 045102.
- (230) Keyling, R.; Schöne, W.-D.; Ekardt, W. *Phys. Rev. B* **2000**, 61, 1670.
- (231) Knoesel, E.; Hotzel, A.; Wolf, M. *Phys. Rev. B* **1998**, 57, 12812.
- (232) Petek, H.; Nagano, H.; Ogawa, S. *Phys. Rev. Lett.* **1999**, 83, 832.
- (233) Gerlach, A.; Berge, K.; Goldmann, A.; Campillo, I.; Rubio, A.; Pitarke, J. M.; Echenique, P. M. *Phys. Rev. B* **2001**, 64, 085423.
- (234) Zhukov, V. P.; Chulkov, E. V.; Echenique, P. M. *Phys. Rev. B* **2006**, 73, 125105.
- (235) Crowell, C. R.; Sze, S. M. In *Physics of thin films*; Haas, G., Thun, R. E., Eds.; Academic Press: New York, 1967; Vol. 4, p 390.
- (236) Franco, N.; Klepeis, J. E.; Bostedt, C.; Van Buuren, T.; Heske, C.; Pankratov, O.; Callcott, T. A.; Ederer, D. L.; Terminello, L. J. *Phys. Rev. B* **2003**, 68, 045116.
- (237) Zhukov, V. P.; Aryasetiawan, F.; Chulkov, E. V.; Echenique, P. M. *Phys. Rev. B* **2002**, 65, 115116.
- (238) van Dijken, S.; Jiang, X.; Parkin, S. S. P. *Phys. Rev. B* **2002**, 66, 094417.
- (239) Jansen, R. *J. Phys. D: Appl. Phys.* **2003**, 36, R289.
- (240) Bacular, M. R.; Schöne, W.-D.; Keyling, R.; Ekardt, W. *Phys. Rev. B* **2002**, 66, 153101.
- (241) Petek, H.; Ogawa, S. *Prog. Surf. Sci.* **1997**, 56, 239.
- (242) Ladstädter, F.; de Pablos, P. F.; Hohenester, U.; Puschnig, P.; Ambrosch-Draxl, C.; de Andres, P. L.; García-Vidal, F. J.; Flores, F. *Phys. Rev. B* **2003**, 68, 085107.
- (243) Cao, J.; Gao, Y.; Elsayed-Ali, H. E.; Mantell, D. A. *Phys. Rev. B* **1998**, 58, 10948.
- (244) Mönnich, A.; Lange, J.; Bauer, M.; Aeschlimann, M.; Nechaev, I. A.; Zhukov, V. P.; Echenique, P. M.; Chulkov, E. V. *Phys. Rev. B* **2006**, 74, 035102.
- (245) Zhukov, V. P.; Andreyev, O.; Hoffmann, D.; Bauer, M.; Aeschlimann, M.; Chulkov, E. V.; Echenique, P. M. *Phys. Rev. B* **2004**, 70, 233106.
- (246) Sklyadneva, I. Yu.; Leonardo, A.; Echenique, P. M.; Ereemeev, S. V.; Chulkov, E. V. *J. Phys.: Condens. Matter* **2006**, 18, 7923.
- (247) Bauer, R.; Schmid, A.; Pavone, P.; Strauch, D. *Phys. Rev. B* **1998**, 57, 11276.

- (248) Zhukov, V. P.; Chulkov, E. V.; Echenique, P. M. *J. Magn. Magn. Mater.* **2004**, 272–276, 466.
- (249) Aeschlimann, M.; Bauer, M.; Pawlik, S.; Weber, W.; Burgermeister, R.; Oberli, D.; Siegmann, H. C. *Phys. Rev. Lett.* **1997**, 79, 5158.
- (250) Wegner, D.; Bauer, A.; Kaindl, G. *Phys. Rev. Lett.* **2005**, 94, 126804.
- (251) Bauer, M.; Pawlik, S.; Aeschlimann, M. *Proc. SPIE* **1998**, 3272, 201.
- (252) Aeschlimann, M.; Bauer, M.; Pawlik, S.; Knorren, R.; Bouzerar, G.; Benemann, K. H. *Appl. Phys. A: Mater. Sci. Process.* **2000**, 71, 485.
- (253) Chulkov, E. V.; Silkin, V. M.; Echenique, P. M. *Surf. Sci.* **2000**, 454–456, 458.
- (254) Silkin, V. M.; Chulkov, E. V. *Fiz. Tverd. Tela* **2000**, 42, 1334 [*Phys. Solid State* **2000**, 42, 1373].
- (255) Karlsson, U. O.; Flodström, S. A.; Engelhardt, R.; Gädeke, W.; Koch, E. E. *Solid State Commun.* **1984**, 49, 711.
- (256) Levinson, H. J.; Greuter, F.; Plummer, E. W. *Phys. Rev. B* **1983**, 27, 727.
- (257) Kevan, S. D.; Stoffel, N. G.; Smith, N. V. *Phys. Rev. B* **1985**, 31, 1788.
- (258) Bartynski, R. A.; Gaylord, R. H.; Gustafsson, T.; Plummer, E. W. *Phys. Rev. B* **1986**, 33, 3644.
- (259) Chulkov, E. V.; Silkin, V. M. *Solid State Commun.* **1986**, 58, 273.
- (260) Chulkov, E. V.; Silkin, V. M.; Shirykalov, E. N. *Surf. Sci.* **1987**, 188, 287.
- (261) Bartynski, R. A.; Jensen, E.; Gustafsson, T.; Plummer, E. W. *Phys. Rev. B* **1985**, 32, 1921.
- (262) Leonardo, A.; Sklyadneva, I. Yu.; Echenique, P. M.; Chulkov, E. V. *Phys. Rev. B*, submitted.
- (263) Pivetta, M.; Silly, F.; Patthey, F.; Pelz, J. P.; Schneider, W.-D. *Phys. Rev. B* **2003**, 67, 193402.
- (264) Straube, P.; Pforte, F.; Michalke, T.; Berge, K.; Gerlach, A.; Goldmann, A. *Phys. Rev. B* **2000**, 61, 14072.
- (265) Keyling, R.; Schöne, W.-D.; Ekardt, W. *Chem. Phys. Lett.* **2002**, 354, 376.
- (266) Reinert, F.; Nicolay, G.; Schmidt, S.; Ehm, D.; Hüfner, S. *Phys. Rev. B* **2001**, 63, 115415.
- (267) Gayone, J. E.; Kirkegaard, C.; Wells, J. W.; Hoffmann, S. V.; Li, Z.; Hofmann, Ph. *Appl. Phys. A* **2005**, 80, 943.
- (268) Wegner, D.; Bauer, A.; Koroteev, Yu. M.; Bihlmayer, G.; Chulkov, E. V.; Echenique, P. M.; Kaindl, G. *Phys. Rev. B* **2006**, 73, 115403.
- (269) Kurth, Ph.; Bihlmayer, G.; Blügel, S. *J. Phys.: Condens. Matter* **2002**, 14, 6353.
- (270) Schäfer, A.; Shumay, I. L.; Wiets, M.; Weinelt, M.; Fauster, Th.; Chulkov, E. V.; Silkin, V. M.; Echenique, P. M. *Phys. Rev. B* **2000**, 61, 13159.
- (271) Borisov, A. G.; Chulkov, E. V.; Echenique, P. M. *Phys. Rev. B* **2006**, 73, 073402.
- (272) Link, S.; Sievers, J.; Dürr, H. A.; Eberhardt, W. *J. Electron Spectrosc. Related Phenom.* **2001**, 114–116, 351.
- (273) Link, S.; Dürr, H. A.; Bihlmayer, G.; Blügel, S.; Eberhardt, W.; Chulkov, E. V.; Silkin, V. M.; Echenique, P. M. *Phys. Rev. B* **2001**, 63, 115420.
- (274) Roth, M.; Pickel, M.; Wang, J.; Weinelt, M.; Fauster, Th. *Appl. Phys. B: Lasers Opt.* **2002**, 74, 661.
- (275) Lingle, R. L., Jr.; Ge, N.-H.; Jordan, R. E.; McNeill, J. D.; Harris, C. B. *Chem. Phys.* **1996**, 205, 191.
- (276) Echenique, P. M.; Osmá, J.; Machado, M.; Silkin, V. M.; Chulkov, E. V.; Pitarke, J. M. *Prog. Surf. Sci.* **2001**, 67, 271.
- (277) Chulkov, E. V.; Osmá, J.; Sarria, I.; Silkin, V. M.; Pitarke, J. M. *Surf. Sci.* **1999**, 433–435, 882.
- (278) Present work.
- (279) Schmidt, A. B.; Pickel, M.; Wiemhöfer, M.; Donath, M.; Weinelt, M. *Phys. Rev. Lett.* **2005**, 95, 107402.
- (280) Crampin, S. *Phys. Rev. Lett.* **2005**, 95, 046801.
- (281) Chulkov, E. V.; Machado, M.; Silkin, V. M. *Vacuum* **2001**, 61, 95.
- (282) Silkin, V. M.; Chulkov, E. V.; Echenique, P. M. *Phys. Rev. B* **1999**, 60, 7820.
- (283) Silkin, V. M.; Chulkov, E. V.; Echenique, P. M. *Phys. Rev. B* **2001**, 64, 172512.
- (284) Heinrichsmeier, M.; Fleszar, A.; Hanke, W.; Eguiluz, A. G. *Phys. Rev. B* **1998**, 57, 14974.
- (285) Bulović, V.; Quiniou, B.; Osgood, R. M., Jr. *J. Vac. Sci. Technol., A* **1994**, 12, 2201.
- (286) Sarria, I.; Osmá, J.; Chulkov, E. V.; Pitarke, J. M.; Echenique, P. M. *Phys. Rev. B* **1999**, 60, 11795.
- (287) de Andres, P. L.; Echenique, P. M.; Flores, F. *Phys. Rev. B* **1989**, 39, 10356.
- (288) The period of classical motion in the $1/4z$ potential can be straightforwardly obtained following: Landau, L. D.; Lifshitz, E. M. *Course of Theoretical Physics*; Butterworth-Heinemann: Oxford, 1999; V.1, Mechanics. Chapter III, §11, problem 2.
- (289) Harris, C. B.; Ge, N. H.; Lingle, R. L., Jr.; McNeill, J. D.; Wong, C. M. *Annu. Rev. Phys. Chem.* **1997**, 48, 711.
- (290) McNeill, J. D.; Lingle, R. L., Jr.; Ge, N.-H.; Wong, C. M.; Jordan, R. E.; Harris, C. B. *Phys. Rev. Lett.* **1997**, 79, 4645.
- (291) Wolf, M.; Knoesel, E.; Hertel, T. *Phys. Rev. B* **1996**, 54, R5295.
- (292) Reuss, C.; Wallauer, W.; Fauster, Th. *Surf. Rev. Lett.* **1996**, 3, 1547.
- (293) Limot, L.; Maroutian, T.; Johansson, P.; Berndt, R. *Phys. Rev. Lett.* **2003**, 91, 196801.
- (294) Liebsch, A. *Phys. Rev. Lett.* **1993**, 71, 145.
- (295) Shumay, I. L.; Höfer, U.; Reuss, Ch.; Thomann, U.; Wallauer, W.; Fauster, Th. *Phys. Rev. B* **1998**, 58, 13974.
- (296) Eiguren, A.; Hellsing, B.; Chulkov, E. V.; Echenique, P. M. *J. Electron Spectrosc. Related Phenom.* **2003**, 129, 111.
- (297) Boger, K.; Weinelt, M.; Fauster, Th. *Phys. Rev. Lett.* **2004**, 92, 126803.
- (298) Rhie, H.-S.; Link, S.; Dürr, H. A.; Eberhardt, W.; Smith, N. V. *Phys. Rev. B* **2003**, 68, 033410.
- (299) Duke, C. B.; Pietronero, L.; Porteus, J. O.; Wendelken, J. F. *Phys. Rev. B* **1975**, 12, 4059.
- (300) Kim, B.-O.; Lee, G.; Plummer, E. W.; Dowben, P. A.; Liebsch, A. *Phys. Rev. B* **1995**, 52, 6057.
- (301) Rocca, M.; Biggio, F.; Valbusa, U. *Phys. Rev. B* **1990**, 42, 2835.
- (302) Rocca, M.; Valbusa, U. *Surf. Sci.* **1993**, 287–288, 770.
- (303) Sprunger, P. T.; Watson, G. M.; Plummer, E. W. *Surf. Sci.* **1992**, 269–270, 551.
- (304) Laitenberger, P.; Palmer, R. E. *Phys. Rev. Lett.* **1996**, 76, 1952.
- (305) Chiarello, G.; Formoso, V.; Santaniello, A.; Colavita, E.; Papagno, L. *Phys. Rev. B* **2000**, 62, 12676.
- (306) Corradini, M.; Del Sole, R.; Onida, G.; Palumbo, M. *Phys. Rev. B* **1998**, 57, 14569.
- (307) Ando, T.; Fowler, A. B.; Stern, F. *Rev. Mod. Phys.* **1982**, 54, 437.
- (308) Silkin, V. M.; García-Lekue, A.; Pitarke, J. M.; Chulkov, E. V.; Zaremba, E.; Echenique, P. M. *Europhys. Lett.* **2004**, 66, 260.
- (309) Pitarke, J. M.; Silkin, V. M.; Chulkov, E. V.; Echenique, P. M. *J. Opt. A: Pure Appl. Opt.* **2005**, 7, S73.
- (310) Pitarke, J. M.; Nazarov, V. U.; Silkin, V. M.; Chulkov, E. V.; Zaremba, E.; Echenique, P. M. *Phys. Rev. B* **2004**, 70, 205403.
- (311) Carlsson, A.; Claesson, D.; Lindgren, S.-Å.; Walldén, L. *Phys. Rev. Lett.* **1996**, 77, 346.
- (312) Carlsson, A.; Hellsing, B.; Lindgren, S.-Å.; Walldén, L. *Phys. Rev. B* **1997**, 56, 1593.
- (313) Fischer, N.; Schuppler, S.; Fischer, R.; Fauster, Th.; Steinmann, W. *Phys. Rev. B* **1993**, 47, 4705.
- (314) Kliewer, J.; Berndt, R. *Phys. Rev. B* **2001**, 65, 035412.
- (315) Fischer, N.; Schuppler, S.; Fischer, R.; Fauster, Th.; Steinmann, W. *Phys. Rev. B* **1991**, 43, 14722.
- (316) Carlsson, J. M.; Hellsing, B. *Phys. Rev. B* **2000**, 61, 13973.
- (317) Fischer, N.; Schuppler, S.; Fauster, Th.; Steinmann, W. *Surf. Sci.* **1994**, 314, 89.
- (318) Chulkov, E. V.; Kliewer, J.; Berndt, R.; Silkin, V. M.; Hellsing, B.; Crampin, S.; Echenique, P. M. *Phys. Rev. B* **2003**, 68, 195422.
- (319) Chulkov, E. V.; Silkin, V. M. *Phys. Rev.* **1989**, 215, 385.
- (320) Fasel, R.; Aebi, P.; Agostino, R. G.; Schlappbach, L.; Osterwalder, J. *Phys. Rev. B* **1996**, 54, 5893.
- (321) Stampfl, C.; Kambe, K.; Fasel, R.; Aebi, P.; Scheffler, M. *Phys. Rev. B* **1998**, 57, 15251.
- (322) Himpel, F. J. *Phys. Rev. B* **1991**, 44, 5966.
- (323) Cercellier, H.; Didot, C.; Fagot-Revurat, Y.; Kierren, B.; Moreau, L.; Malterre, D.; Reinert, F. *Phys. Rev. B* **2006**, 73, 195413.
- (324) Chiang, T.-C. *Surf. Sci. Rep.* **2000**, 39, 181.
- (325) Palomares, F. J.; Serrano, M.; Ruiz, A.; Soria, F.; Horn, K.; Alonso, M. *Surf. Sci.* **2002**, 513, 283.
- (326) Cercellier, H.; Fagot-Revurat, Y.; Kierren, B.; Malterre, D.; Reinert, F. *Surf. Sci.* **2004**, 566–568, 520.
- (327) Cercellier, H.; Fagot-Revurat, Y.; Kierren, B.; Reinert, F.; Popović, D.; Malterre, D. *Phys. Rev. B* **2004**, 70, 193412.
- (328) Ogando, E.; Zabala, N.; Chulkov, E. V.; Puska, M. J. *Phys. Rev. B* **2004**, 69, 153410.
- (329) Ogando, E.; Zabala, N.; Chulkov, E. V.; Puska, M. J. *Phys. Rev. B* **2005**, 71, 205401.
- (330) Valla, T.; Pervan, P.; Milun, M.; Hayden, A. B.; Woodruff, D. P. *Phys. Rev. B* **1996**, 54, 11786.
- (331) Milun, M.; Pervan, P.; Woodruff, D. P. *Rep. Prog. Phys.* **2002**, 65, 99.
- (332) Wessendorf, M.; Wiemann, C.; Bauer, M.; Aeschlimann, M.; Schneider, M. A.; Brune, H.; Kern, K. *Appl. Phys. A: Mater. Sci. Process.* **2004**, 78, 183.
- (333) Schiller, F.; Cordon, J.; Vyalikh, D.; Rubio, A.; Ortega, J. E. *Phys. Rev. Lett.* **2005**, 94, 016103.
- (334) Popović, D.; Reinert, F.; Hüfner, S.; Grigoryan, V. G.; Springborg, M.; Cercellier, H.; Fagot-Revurat, Y.; Kierren, B.; Malterre, D. *Phys. Rev. B* **2005**, 72, 045419.
- (335) Bendounan, A.; Forster, F.; Zirot, J.; Schmitt, F.; Reinert, F. *Phys. Rev. B* **2005**, 72, 075407.

- (336) Schiller, F.; Keyling, R.; Chulkov, E. V.; Ortega, J. E. *Phys. Rev. Lett.* **2005**, 95, 126402.
- (337) Koitzsch, C.; Battaglia, C.; Clerc, F.; Despont, L.; Garnier, M. G.; Aebi, P. *Phys. Rev. Lett.* **2005**, 95, 126401.
- (338) Diehl, R. D.; McGrath, R. *Surf. Sci. Rep.* **1996**, 23, 43.
- (339) Tochiwara, H.; Mizuno, S. *Prog. Surf. Sci.* **1998**, 58, 1.
- (340) Luh, D.-A.; Miller, T.; Paggel, J. J.; Chiang, T.-C. *Phys. Rev. Lett.* **2002**, 88, 256802.
- (341) Hellsing, B.; Carlsson, J.; Walldén, L.; Lindgren, S.-Å. *Phys. Rev. B* **2000**, 61, 2343.
- (342) Borisova, S. D.; Rusina, G. G.; Eremeev, S. V.; Echenique, P. M.; Benedek, G.; Sklyadneva, I. Yu.; Chulkov, E. V. *Phys. Rev. B*, submitted.
- (343) Miller, A. D.; Bezel, I.; Gaffney, K. J.; Garrett-Roe, S.; Liu, S. H.; Szymanski, P.; Harris, C. B. *Science* **2002**, 297, 1163.
- (344) Zhu, X.-Y. *Surf. Sci. Rep.* **2004**, 56, 1.
- (345) McNeill, J. D.; Lingle, R. L., Jr.; Jordan, R. E.; Padowitz, D. F.; Harris, C. B. *J. Chem. Phys.* **1996**, 105, 3883.
- (346) Wong, C. M.; McNeill, J. D.; Gaffney, K. J.; Ge, N.-H.; Miller, A. D.; Liu, S. H.; Harris, C. B. *J. Phys. Chem. B* **1999**, 103, 282.
- (347) Hotzel, A.; Moos, G.; Ishioka, K.; Wolf, M.; Ertl, G. *Appl. Phys. B: Lasers Opt.* **1999**, 68, 615.
- (348) Hotzel, A.; Wolf, M.; Gauyacq, J. P. *J. Phys. Chem. B* **2000**, 104, 8438.
- (349) Wang, H.; Dutton, G.; Zhu, X.-Y. *J. Phys. Chem. B* **2000**, 104, 10332.
- (350) Garrett-Roe, S.; Shipman, S. T.; Szymanski, P.; Strader, M. L.; Yang, A.; Harris, C. B. *J. Phys. Chem. B* **2005**, 109, 20370.
- (351) Cole, M. W. *Phys. Rev. B* **1971**, 3, 4418.
- (352) Berthold, W.; Feulner, P.; Höfer, U. *Chem. Phys. Lett.* **2002**, 358, 502.
- (353) Berthold, W.; Rebentrost, F.; Feulner, P.; Höfer, U. *Appl. Phys. A: Mater. Sci. Process.* **2004**, 78, 131.
- (354) Perluzzo, G.; Bader, G.; Caron, L. G.; Sanche, L. *Phys. Rev. Lett.* **1985**, 55, 545.
- (355) Machado, M.; Berthold, W.; Höfer, U.; Chulkov, E. V.; Echenique, P. M. *Surf. Sci.* **2004**, 564, 87.
- (356) Marinica, D. C.; Ramseyer, C.; Borisov, A. G.; Teillet-Billy, D.; Gauyacq, J. P. *Surf. Sci.* **2003**, 528, 78.
- (357) Lindgren, S.-Å.; Walldén, L. *Phys. Rev. B* **1989**, 40, 11546.
- (358) Papadia, S.; Persson, M.; Salmi, L.-A. *Phys. Rev. B* **1990**, 41, 10237.
- (359) Park, J.-Y.; Ham, U. D.; Kahng, S.-J.; Kuk, Y.; Miyake, K.; Hata, K.; Shigekawa, H. *Phys. Rev. B* **2000**, 62, R16341.
- (360) Hövel, H.; Grimm, B.; Reihl, B. *Surf. Sci.* **2001**, 477, 43.
- (361) Forster, F.; Nicolay, G.; Reinert, F.; Ehm, D.; Schmidt, S.; Hüfner, S. *Surf. Sci.* **2003**, 532, 160.
- (362) Andreev, T.; Barke, I.; Hövel, H. *Phys. Rev. B* **2004**, 70, 205426.
- (363) Rohleder, M.; Berthold, W.; Gütde, J.; Höfer, U. *Phys. Rev. Lett.* **2005**, 94, 017401.
- (364) Gütde, J.; Höfer, U. *Prog. Surf. Sci.* **2005**, 80, 49.
- (365) Perluzzo, G.; Sanche, L.; Gaubert, C.; Baudoin, R. *Phys. Rev. B* **1984**, 30, 4292.
- (366) Caron, L. G.; Perluzzo, G.; Bader, G.; Sanche, L. *Phys. Rev. B* **1986**, 33, 3027.
- (367) Sack, N. J.; Akbulut, M.; Madey, T. E. *Surf. Sci.* **1995**, 334, L695.
- (368) Nordlander, P.; Modisette, J. P. *Nucl. Instrum. Methods B* **1997**, 125, 305.
- (369) Sanche, L. *J. Phys. B: At. Mol. Opt. Phys.* **1990**, 23, 1597.
- (370) Palmer, R. E.; Rous, P. J. *Rev. Mod. Phys.* **1992**, 64, 383.
- (371) Palmer, R. E. *Prog. Surf. Sci.* **1992**, 41, 51.
- (372) Michaud, M.; Sanche, L. *J. Electron Spectrosc. Related Phenom.* **1990**, 51, 237.
- (373) Marinica, D. C.; Teillet-Billy, D.; Gauyacq, J. P.; Michaud, M.; Sanche, L. *Phys. Rev. B* **2001**, 64, 085408.
- (374) Marinica, D. C.; Ramseyer, C.; Teillet-Billy, D.; Gauyacq, J. P. *Surf. Sci.* **2006**, 600, 803.
- (375) Cohen-Tannoudji, C.; Dupont-Roc, J.; Grynberg, G. *Processus d'interaction entre photons et atomes*; EDP Sciences/CNRS Editions: Les Ulis, Paris, France, 2001.
- (376) Joffe, A. F.; Regel, A. R. *Prog. Semiconduct.* **1960**, 4, 237.
- (377) Kazansky, A. K.; Borisov, A. G.; Gauyacq, J. P. *Surf. Sci.* **2003**, 544, 309.
- (378) Kevan, S. D. *Phys. Rev. Lett.* **1983**, 50, 526.
- (379) Kevan, S. D. *Phys. Rev. B* **1986**, 33, 4364.
- (380) Kevan, S. D. *Surf. Sci.* **1986**, 178, 229.
- (381) Schoenlein, R. W.; Fujimoto, J. G.; Eesley, G. L.; Capehart, T. W. *Phys. Rev. B* **1991**, 43, 4688.
- (382) Schuppler, S.; Fischer, N.; Fauster, Th.; Steinmann, W. *Phys. Rev. B* **1992**, 46, 13539.
- (383) Wang, X. Y.; Paiella, R.; Osgood, R. M., Jr. *Phys. Rev. B* **1995**, 51, 17035.
- (384) Wallauer, W.; Fischer, R.; Fauster, Th. *Surf. Sci.* **1996**, 364, 297.
- (385) Reuss, Ch.; Shumay, I. L.; Thomann, U.; Kutschera, M.; Weinelt, M.; Fauster, Th.; Höfer, U. *Phys. Rev. Lett.* **1999**, 82, 153.
- (386) Fauster, Th.; Reuss, Ch.; Shumay, I. L.; Weinelt, M. *Chem. Phys.* **2000**, 251, 111.
- (387) Weinelt, M. *Surf. Sci.* **2001**, 482–485, 519.
- (388) Weinelt, M. *Appl. Phys. A: Mater. Sci. Process.* **2000**, 71, 493.
- (389) Boger, K.; Weinelt, M.; Wang, J.; Fauster, T. *Appl. Phys. A: Mater. Sci. Process.* **2004**, 78, 161.
- (390) Fauster, Th.; Weinelt, M. *Surf. Sci.* **2005**, 593, 1.
- (391) Berthold, W.; Gütde, J.; Feulner, P.; Höfer, U. *Appl. Phys. B: Lasers Opt.* **2001**, 73, 865.
- (392) Wang, X. Y.; Shen, X. J.; Osgood, R. M., Jr.; Haight, R.; Himpfel, F. J. *Phys. Rev. B* **1996**, 53, 15738.
- (393) Roth, M.; Pickel, M.; Jinxiang, W.; Weinelt, M.; Fauster, Th. *Phys. Rev. Lett.* **2002**, 88, 096802.
- (394) Shen, X. J.; Kwak, H.; Radojevic, A. M.; Smadici, S.; Mocuta, D.; Osgood, R. M., Jr. *Chem. Phys. Lett.* **2002**, 351, 1.
- (395) Tobin, R. G. *Surf. Sci.* **2002**, 502–503, 374.
- (396) Ishida, H. *Phys. Rev. B* **1996**, 54, 10905.
- (397) Persson, B. N. J. *Phys. Rev. B* **1991**, 44, 3277.
- (398) Hein, M.; Dumas, P.; Otto, A.; Williams, G. P. *Surf. Sci.* **2000**, 465, 249.
- (399) Bly, D. N.; Rous, P. J. *Phys. Rev. B* **1996**, 53, 13909.
- (400) Ishida, H. *Phys. Rev. B* **1994**, 49, 14610.
- (401) Crommie, M. F.; Lutz, C. P.; Eigler, D. M. *Nature* **1993**, 363, 524.
- (402) Hasegawa, Y.; Avouris, Ph. *Phys. Rev. Lett.* **1993**, 71, 1071.
- (403) Bürgi, L.; Jeandupeux, O.; Brune, H.; Kern, K. *Phys. Rev. Lett.* **1999**, 82, 4516.
- (404) Schneider, M. A.; Vitali, L.; Knorr, N.; Kern, K. *Phys. Rev. B* **2002**, 65, 121406(R).
- (405) Vitali, L.; Wahl, P.; Schneider, M. A.; Kern, K.; Silkin, V. M.; Chulkov, E. V.; Echenique, P. M. *Surf. Sci.* **2003**, 523, L47.
- (406) Roth, M.; Weinelt, M.; Fauster, Th.; Wahl, P.; Schneider, M. A.; Diekhöner, L.; Kern, K. *Appl. Phys. A: Mater. Sci. Process.* **2004**, 78, 155.
- (407) Wahlström, E.; Ekval, I.; Olin, H.; Walldén, L. *Appl. Phys. A: Mater. Sci. Process.* **1998**, 66, S1107.
- (408) Repp, J.; Moresco, F.; Meyer, G.; Rieder, K.-H.; Hyldgaard, P.; Persson, M. *Phys. Rev. Lett.* **2000**, 85, 2981.
- (409) Fichtorn, K. A.; Merrick, M. L.; Scheffler, M. *Phys. Rev. B* **2003**, 68, 041404(R).
- (410) Bogicevic, A.; Ovesson, S.; Hyldgaard, P.; Lundqvist, B. I.; Brune, H.; Jennison, D. R. *Phys. Rev. Lett.* **2000**, 85, 1910.
- (411) Knorr, N.; Brune, H.; Eppel, M.; Hirstein, A.; Schneider, M. A.; Kern, K. *Phys. Rev. B* **2002**, 65, 115420.
- (412) Hyldgaard, P.; Persson, M. *J. Phys.: Condens. Matter* **2000**, 12, L13.
- (413) Crommie, M. F.; Lutz, C. P.; Eigler, D. M. *Science* **1993**, 262, 218.
- (414) Crampin, S.; Boon, M. H.; Inglesfield, J. E. *Phys. Rev. Lett.* **1994**, 73, 1015.
- (415) Harbury, H. K.; Porod, W. *Phys. Rev. B* **1996**, 53, 15455.
- (416) Crampin, S.; Bryant, O. R. *Phys. Rev. B* **1996**, 54, R17367.
- (417) Kliewer, J.; Berndt, R.; Crampin, S. *Phys. Rev. Lett.* **2000**, 85, 4936.
- (418) Fiete, G. A.; Heller, E. J. *Rev. Mod. Phys.* **2003**, 75, 933.
- (419) Crampin, S.; Jensen, H.; Kröger, J.; Limot, L.; Berndt, R. *Phys. Rev. B* **2005**, 72, 035443.
- (420) Gauyacq, J. P.; Borisov, A. G. *Surf. Sci.* **2006**, 600, 825.
- (421) Usman, E. Yu.; Urazgil'din, I. F.; Borisov, A. G.; Gauyacq, J. P. *Phys. Rev. B* **2001**, 64, 205405.
- (422) Simon, B. *Ann. Phys.* **1976**, 97, 279.
- (423) Zaremba, E.; Nagy, I.; Echenique, P. M. *Phys. Rev. Lett.* **2003**, 90, 046801.
- (424) Zaremba, E.; Nagy, I.; Echenique, P. M. *Phys. Rev. B* **2005**, 71, 125323.
- (425) Limot, L.; Pehlke, E.; Kröger, J.; Berndt, R. *Phys. Rev. Lett.* **2005**, 94, 036805.
- (426) Madhavan, V.; Chen, W.; Jamneala, T.; Crommie, M. F.; Wingreen, N. S. *Phys. Rev. B* **2001**, 64, 165412.
- (427) Avouris, Ph.; Lyo, I. W.; Molinas-Mata, P. *Chem. Phys. Lett.* **1995**, 240, 423.
- (428) Ortega, J. E.; Himpfel, F. J.; Haight, R.; Peale, D. R. *Phys. Rev. B* **1994**, 49, 13859.
- (429) Namba, H.; Nakanishi, N.; Yamaguchi, T.; Kuroda, H. *Phys. Rev. Lett.* **1993**, 71, 4027.
- (430) Shen, X. J.; Kwak, H.; Mocuta, D.; Radojevic, A. M.; Smadici, S.; Osgood, R. M., Jr. *Phys. Rev. B* **2001**, 63, 165403.
- (431) Bartels, L.; Hla, S. W.; Kühnle, A.; Meyer, G.; Rieder, K.-H.; Manson, J. R. *Phys. Rev. B* **2003**, 67, 205416.
- (432) Smadici, S.; Osgood, R. M. *Phys. Rev. B* **2005**, 71, 165424.
- (433) Bobrov, K.; Mayne, A. J.; Dujardin, G. *Nature* **2001**, 413, 616.
- (434) Gadzuk J. W.; Sunjic, M. In *Aspects of electron-molecule scattering and photoionisation*, AIP conference proceedings 204; Herzenberg, A., Ed.; American Institute of Physics: New York, 1990; p 118.
- (435) Assion, A.; Baumert, T.; Bergt, M.; Brixner, T.; Kiefer, B.; Seyfried, V.; Strehle, M.; Gerber, G. *Science* **1998**, 282, 919.

- (436) Petek, H.; Nagano, H.; Weida, M. J.; Ogawa, S. *J. Phys. Chem. A* **2000**, *104*, 10234.
- (437) Anderson, P. W. *Phys. Rev.* **1961**, *124*, 41.
- (438) Grimley, T. B. *Proc. Phys. Soc. London* **1967**, *90*, 751; 92, 776.
- (439) Newns, D. M. *Phys. Rev.* **1969**, *178*, 1123.
- (440) Spanjaard, D.; Desjonquères, M. C. *Electronic Theory of Chemisorption. In Interactions of atoms and molecules with solid surfaces*; Bortolani, V., March, N. H., Tosi, M. P., Eds.; Plenum Press: New York, 1990; p 255.
- (441) Lang, N. D.; Williams, A. R. *Phys. Rev. B* **1978**, *18*, 616.
- (442) Scheffler, M.; Stampfl, C. In *Electronic Structure, Handbook of Surface Science*; Horn, K., Scheffler, M., Eds.; Elsevier Science: Amsterdam, 2000; Vol. 2, p 285.
- (443) Nordlander, P.; Tully, J. C. *Phys. Rev. Lett.* **1988**, *61*, 990.
- (444) Teillet-Billy, D.; Gauyacq, J. P. *Surf. Sci.* **1990**, *239*, 343.
- (445) Deutscher, S. A.; Yang, X.; Burgdörfer, J. *Nucl. Instrum. Methods B* **1995**, *100*, 336.
- (446) Martín, F.; Politis, M. F. *Surf. Sci.* **1996**, *356*, 247.
- (447) Kürpick, P.; Thumm, U.; Wille, U. *Nucl. Instrum. Methods B* **1997**, *125*, 273.
- (448) Merino, J.; Lorente, N.; Pou, P.; Flores, F. *Phys. Rev. B* **1996**, *54*, 10959.
- (449) Ermoshin, V. A.; Kazansky, A. K. *Phys. Lett. A* **1996**, *218*, 99.
- (450) Borisov, A. G.; Teillet-Billy, D.; Gauyacq, J. P. *Phys. Rev. Lett.* **1992**, *68*, 2842.
- (451) Maazouz, M.; Borisov, A. G.; Esaulov, V. A.; Gauyacq, J. P.; Guillemot, L.; Lacombe, S.; Teillet-Billy, D. *Phys. Rev. B* **1997**, *55*, 13869.
- (452) Mannstadt, W.; Grawert, G. *Phys. Rev. B* **1995**, *52*, 5343.
- (453) Nordlander, P.; Tully, J. C. *Phys. Rev. B* **1990**, *42*, 5564.
- (454) Borisov, A. G.; Teillet-Billy, D.; Gauyacq, J. P.; Winter, H.; Dierkes, G. *Phys. Rev. B* **1996**, *54*, 17166.
- (455) Bauer, M.; Pawlik, S.; Aeschlimann, M. *Phys. Rev. B* **1997**, *55*, 10040.
- (456) Bauer, M.; Pawlik, S.; Aeschlimann, M. *Phys. Rev. B* **1999**, *60*, 5016.
- (457) Ogawa, S.; Nagano, H.; Petek, H. *Phys. Rev. Lett.* **1999**, *82*, 1931.
- (458) Petek, H.; Weida, M. J.; Nagano, H.; Ogawa, S. *Science* **2000**, *288*, 1402.
- (459) Petek, H.; Nagano, H.; Weida, M. J.; Ogawa, S. *J. Phys. Chem. B* **2001**, *105*, 6767.
- (460) Gurney, R. W. *Phys. Rev.* **1935**, *47*, 479.
- (461) Scheffler, M.; Droste, Ch.; Fleszar, A.; Máca, F.; Wachutka, G.; Barzel, G. *Physica B* **1991**, *172*, 143.
- (462) Gauyacq, J. P.; Borisov, A. G.; Raseev, G.; Kazansky, A. K. *Faraday Discuss.* **2000**, *117*, 15.
- (463) Menzel, D.; Gomer, R. *J. Chem. Phys.* **1964**, *41*, 3311.
- (464) Redhead, P. A. *Can. J. Phys.* **1964**, *42*, 886.
- (465) Hertel, T.; Knoesel, E.; Wolf, M.; Ertl, G. *Phys. Rev. Lett.* **1996**, *76*, 535.
- (466) Ueba, H.; Mii, T. *Appl. Phys. A* **2000**, *71*, 537.
- (467) Gahl, C.; Bovensiepen, U.; Frischkorn, C.; Wolf, M. *Phys. Rev. Lett.* **2002**, *89*, 107402.
- (468) Bauer, M.; Wessendorf, M.; Hoffmann, D.; Wiemann, C.; Mönnich, A.; Aeschlimann, M. *Appl. Phys. A: Mater. Sci. Process.* **2005**, *80*, 987.
- (469) Kazansky, A. K.; Borisov, A. G.; Gauyacq, J. P. *Surf. Sci.* **2005**, *577*, 47.
- (470) Knoesel, E.; Hertel, T.; Wolf, M.; Ertl, G. *Chem. Phys. Lett.* **1995**, *240*, 409.
- (471) Bartels, L.; Meyer, G.; Reider, K.-H.; Velic, D.; Knoesel, E.; Hotzel, A.; Wolf, M.; Ertl, G. *Phys. Rev. Lett.* **1998**, *80*, 2004.
- (472) Gauyacq, J. P.; Borisov, A. G.; Raseev, G. *Surf. Sci.* **2001**, *490*, 99.
- (473) Lorente, N.; Persson, M. *Faraday Discuss.* **2000**, *117*, 277.
- (474) King, G. C.; Tronc, M.; Read, F. H.; Bradford, R. C. *J. Phys. B: At. Mol. Phys.* **1977**, *10*, 2479.
- (475) Avaldi, L.; Dawber, G.; Camilloni, R.; King, G. C.; Roper, M.; Siggel, M. R. F.; Stefani, G.; Zitnik, M. *J. Phys. B: At. Mol. Opt. Phys.* **1994**, *27*, 3953.
- (476) Menzel, D. *Appl. Phys. A: Mater. Sci. Process.* **1990**, *51*, 163.
- (477) Rocker, G.; Feulner, P.; Scheuerer, R.; Zhu, L.; Menzel, D. *Phys. Scr.* **1990**, *41*, 1014.
- (478) Björneholm, O.; Nilsson, A.; Sandell, A.; Hernnäs B.; Mårtensson, N. *Phys. Rev. Lett.* **1992**, *68*, 1892.
- (479) Ohno, M. *Phys. Rev. B* **1994**, *50*, 2566.
- (480) Karis, O.; Nilsson, A.; Weinelt, M.; Wiell, T.; Puglia, C.; Wassdahl, N.; Mårtensson, N.; Samant, M.; Stöhr, J. *Phys. Rev. Lett.* **1996**, *76*, 1380.
- (481) Sandell, A.; Hjortstam, O.; Nilsson, A.; Brühwiler, P. A.; Eriksson, O.; Bennich, P.; Rudolf, P.; Wills, J. M.; Johansson, B.; Mårtensson, N. *Phys. Rev. Lett.* **1997**, *78*, 4994.
- (482) Keller, C.; Stichler, M.; Comelli, G.; Esch, F.; Lizzit, S.; Menzel, D.; Wurth, W. *Phys. Rev. B* **1998**, *57*, 11951.
- (483) Keller, C.; Stichler, M.; Comelli, G.; Esch, F.; Lizzit, S.; Wurth, W.; Menzel, D. *Phys. Rev. Lett.* **1998**, *80*, 1774.
- (484) Sandell, A.; Brühwiler, P. A.; Nilsson, A.; Bennich, P.; Rudolf, P.; Mårtensson, N. *Surf. Sci.* **1999**, *429*, 309.
- (485) Brühwiler, P. A.; Karis, O.; Mårtensson, N. *Rev. Mod. Phys.* **2002**, *74*, 703.
- (486) Gortel, Z. W.; Menzel, D. *Phys. Rev. B* **2001**, *64*, 115416.
- (487) Wurth, W.; Menzel, D. *Chem. Phys.* **2000**, *251*, 141.
- (488) Föhlisch, A.; Menzel, D.; Feulner, P.; Ecker, M.; Weimar, R.; Kostov, K. L.; Tyuliev, G.; Lizzit, S.; Larciprete, R.; Hennies, F.; Wurth, W. *Chem. Phys.* **2003**, *289*, 107.
- (489) Vijayalakshmi, S.; Föhlisch, A.; Hennies, F.; Pietzsch, A.; Nagasono, M.; Wurth, W.; Borisov, A. G.; Gauyacq, J. P. *Chem. Phys. Lett.* **2006**, *427*, 91.
- (490) Keller, C.; Stichler, M.; Comelli, G.; Esch, F.; Lizzit, S.; Menzel, D.; Wurth, W. *J. Electron Spectrosc. Related Phenom.* **1998**, *93*, 135.
- (491) Da Silva, J. L. F.; Stampfl, C.; Scheffler, M. *Phys. Rev. Lett.* **2003**, *90*, 66104.
- (492) Troullier, N.; Martins, J. L. *Phys. Rev. B* **1991**, *43*, 1993.
- (493) Padowitz, D. F.; Merry, W. R.; Jordan, R. E.; Harris, C. B. *Phys. Rev. Lett.* **1992**, *69*, 3583.
- (494) Hotzel, A.; Ishioka, K.; Knoesel, E.; Wolf, M.; Ertl, G. *Chem. Phys. Lett.* **1998**, *285*, 271.
- (495) Berthold, W.; Höfer, U.; Feulner, P.; Menzel, D. *Chem. Phys.* **2000**, *251*, 123.
- (496) Gauyacq, J. P. *Phys. Rev. B* **2005**, *71*, 115433.
- (497) Economou, E. N. *Green's functions in Quantum Physics*; Springer: Berlin, 1983.
- (498) Melnikov, A.; Radu, I.; Bovensiepen, U.; Krupin, O.; Starke, K.; Matthias, E.; Wolf, M. *Phys. Rev. Lett.* **2003**, *91*, 227403.
- (499) Bovensiepen, U.; Melnikov, A.; Radu, I.; Krupin, O.; Starke, K.; Wolf, M.; Matthias, E. *Phys. Rev. B* **2004**, *69*, 235417.
- (500) Lisowski, M.; Loukakos, P. A.; Melnikov, A.; Radu, I.; Ungureanu, L.; Wolf, M.; Bovensiepen, U. *Phys. Rev. Lett.* **2005**, *95*, 137402.
- (501) LaShell, S.; McDougall, B. A.; Jensen, E. *Phys. Rev. Lett.* **1996**, *77*, 3419.
- (502) Chulkov, E. V.; Koroteev, Yu. M.; Silkin, V. M. *Surf. Sci.* **1991**, *247*, 115.
- (503) Reinert, F. *J. Phys.: Condens. Matter* **2003**, *15*, S693.
- (504) Henk, J.; Ernst, A.; Bruno, P. *Phys. Rev. B* **2003**, *68*, 165416.
- (505) Koroteev, Yu. M.; Bihlmayer, G.; Gayone, J. E.; Chulkov, E. V.; Blügel, S.; Echenique, P. M.; Hofmann, Ph. *Phys. Rev. Lett.* **2004**, *93*, 046403.
- (506) Pascual, J. I.; Bihlmayer, G.; Koroteev, Yu. M.; Rust, H.-P.; Ceballos, G.; Hansmann, M.; Horn, K.; Chulkov, E. V.; Blügel, S.; Echenique, P. M.; Hofmann, Ph. *Phys. Rev. Lett.* **2004**, *93*, 196802.
- (507) McLaughlan, J. R.; Llewellyn-Samuel, E. M.; Crampin, S. *J. Phys.: Condens. Matter* **2004**, *16*, 6841.
- (508) Hoesch, M.; Muntwiler, M.; Petrov, V. N.; Hengsberger, M.; Patthey, L.; Shi, M.; Falub, M.; Greber, T.; Osterwalder, J. *Phys. Rev. B* **2004**, *69*, 241401(R).
- (509) Hofmann, Ph.; Gayone, J. E.; Bihlmayer, G.; Koroteev, Yu. M.; Chulkov, E. V. *Phys. Rev. B* **2005**, *71*, 195413.
- (510) Mönig, H.; Sun, J.; Koroteev, Yu. M.; Bihlmayer, G.; Wells, J.; Chulkov, E. V.; Pohl, K.; Hofmann, Ph. *Phys. Rev. B* **2005**, *72*, 085410.
- (511) Hofmann, Ph. *Prog. Surf. Sci.* **2006**, *81*, 191.
- (512) Hirahara, T.; Nagao, T.; Matsuda, I.; Bihlmayer, G.; Chulkov, E. V.; Koroteev, Yu. M.; Echenique, P. M.; Saito, M.; Hasegawa, S. *Phys. Rev. Lett.*, submitted.
- (513) Crommie, M. F. *J. Electron Spectrosc. Related Phenom.* **2000**, *109*, 1.
- (514) Braun, K.-F.; Rieder, K.-H. *Phys. Rev. Lett.* **2002**, *88*, 096801.
- (515) Limot, L.; Pehlke, E.; Kröger, J.; Berndt, R. *Phys. Rev. Lett.* **2005**, *94*, 036805.
- (516) Diekhöner, L.; Schneider, M. A.; Baranov, A. N.; Stepanyuk, V. S.; Bruno, P.; Kern, K. *Phys. Rev. Lett.* **2003**, *90*, 236801.
- (517) Stepanyuk, V. S.; Niebergall, L.; Hergert, W.; Bruno, P. *Phys. Rev. Lett.* **2005**, *94*, 187201.
- (518) Mugarza, A.; Mascaraque, A.; Repain, V.; Rousset, S.; Altmann, K. N.; Himpel, F. J.; Koroteev, Yu. M.; Chulkov, E. V.; García de Abajo, F. J.; Ortega, J. E. *Phys. Rev. B* **2002**, *66*, 245419.
- (519) Baumberger, F.; Greber, T.; Delley, B.; Osterwalder, J. *Phys. Rev. Lett.* **2002**, *88*, 237601.
- (520) Mugarza, A.; Ortega, J. E. *J. Phys.: Condens. Matter* **2003**, *15*, S3281.
- (521) Roth, M.; Pickel, M.; Weinelt, M.; Fauster, Th. *Appl. Phys. A: Mater. Sci. Process.* **2004**, *78*, 149.